Université catholique de Louvain

Faculté des Sciences Appliquées

LABORATOIRE DE TÉLÉCOMMUNICATIONS
ET
TÉLÉDÉTECTION

B-1348 Louvain-la-Neuve
Belgique

Method of Moments Simulation of Infinite and Finite Periodic Structures
and Application to High-Gain Metamaterial Antennas

Xavier Dardenne

Thèse présentée en vue de l'obtention du grade de
Docteur en Sciences Appliquées

Examination Committee:

Christophe CRAEYE (UCL/TELE) - *Supervisor*
Igor NEFEDOV (Saratov University, Russia)
Filippo CAPOLINO (University of Siena, Italy)
Isabelle HUYNEN (UCL/EMIC)
Piotr SOBIESKI (UCL/TELE)
Jean-François REMACLE (UCL/AUCE)
Luc VANDENDORPE (UCL/ELEC) - *President*

March 2007

Abstract

The overall goal of the present thesis is double, namely to develop and validate an efficient numerical simulation code to study finite and infinite periodic structures and to propose efficient techniques for the design of high gain antennas based on metamaterials.

In a first instance, general properties of electromagnetic fields and sources are recalled. Then, some details are given on the numerical implementation of the Method of Moments based on the surface equivalence principle. Thanks to this code, both large phased arrays and metamaterials made of metal (either PEC or lossy) and/or dielectrics can be easily studied. The integral equation formulations at the heart of this code are the EFIE and the PMCHWT, respectively for metallic and dielectric structures. The first one enforces the nullity of the tangential electric field along PEC surfaces while the second insures the continuity of both tangential E and H fields along the interfaces between dielectric media.

To describe the fields radiated by large antenna arrays, or to compute transmission and reflection properties of metamaterials, fast infinite-array simulations can be used. To our best knowledge, it is the first time that a MoM implementation allows the simulation of both metallic and dielectric infinitely periodic structures. These simulations resort to the fast computation of the doubly periodic Green's function. It is shown how the latter is tabulated to further reduce computation time, using three different formulations, adequately chosen to guarantee optimum convergence in any practical situation. These formulations also allow a very easy extraction of the singularities present in the Green's function and its gradient.

The analysis of radiating devices based on periodic metamaterials often needs the analysis of periodic structures excited by a single primary source. We show that the Array Scanning Method allows to efficiently simulate periodic structures, made of three-dimensional cells, excited by a single (non periodic) source. Moreover, finite periodic structures can also be studied, in first approximation, by resorting to a combination of the Array scanning Method and a windowing technique.

Another way of accounting for the finiteness of real structures, based on a finite-by-infinite array approach, is presented. This approach relies on the use of the singly periodic Green's function, combined with an iterative solver. It is also demonstrated that this finite-by-infinite array approach can be used in conjunction with the Array Scanning Method and windowing to estimate element patterns of any element in a finite array.

In-depth analysis of periodic metamaterials is also possible thanks to the numerical computation of their dispersion curves. These curves are of prime importance in the determination of the modes that can propagate in periodic structures, as well as in the description of the characteristics of these modes. This technique is illustrated on wire media and it is shown how a numerical eigenmode analysis demonstrated that when a waveguide is filled with a wire medium, waves can propagate below the cut-off frequency of the empty guide. This yields very promising perspectives in terms of miniaturization of waveguide-based antennas.

All these techniques are validated numerically on several examples and it will then be shown how they can be combined to design high gain antennas based on metamaterials. Two optimized examples of such antennas are proposed. The first one uses a low permittivity metamaterial and the second one is based on a slotted waveguide exciting a metamaterial superstrate made of frequency selective surfaces. In the latter case, an efficient design method is presented. This method resorts to the separate analysis of the waveguide and the superstrate by defining an interior and an exterior problem, and replacing the electric field in the slot by equivalent magnetic currents.

The tools and methods presented in this thesis continue to be extended to further improve performance and broaden the range of applications. For instance, the interior-exterior separation mentioned above is currently extended to more than one feeding slot. This opens the possibility to efficiently design arrays of slots, dual-band as well as dual-polarization high gain antennas.
Some work is also carried out towards the analysis of large finite arrays of strongly coupled elements (such as electrically connected tapered slot antennas), using a combination of Macro Basis Functions, the Array Scanning Method and a multipole approach.

Contents

Introduction

1

1.1 Objective of the thesis

These last decades, periodic structures have received more and more attention in electromagnetics and particularly in antenna design. In this domain, the most common and well known periodic structure is the phased array. A phased array is a group of antennas in which the relative phases of the respective signals feeding the antennas are varied in such a way that the effective radiation pattern of the array is reinforced in a desired direction and suppressed in undesired directions. This technology was originally developed by Luis Alvarez during World War II as a rapidly steerable radar system for "ground-controlled approach", a system to aid in the landing of aeroplanes in England. It was later adapted for radio astronomy, and generalized in interferometric radio antennas. Nowadays, phased arrays are used in innumerable applications for the versatility of their radiation pattern.

Besides this, recent years have seen a growing interest in a new kind of periodic structures called "metamaterials". These new artificial materials exhibit many new appealing properties, not found in nature, and open many new possibilities in the domain of antenna design. An overview of these metamaterials and their properties can be found in the next section.

The leading idea at the basis of the present thesis is to develop efficient numerical techniques to study periodic structures such as phased arrays and metamaterials, and to show how these techniques can be used in the design of compact, high gain antennas, based on metamaterials.

1.2 History of metamaterials

1.2.1 Definition

Over the past five years, metamaterials have become one of the hottest topics in several areas of science and technology, encompassing electromagnetics and photonics, materials science, and engineering. "Meta" means "beyond" in Greek. But why this simple merging of "meta" and "materials" has attracted so much attention from researchers, and why has it resulted in an exponentially growing number of publications in the field? Here are some definitions of metamaterials that can be found in the literature and that could provide a partial answer to this question:

- Electromagnetic metamaterials are artificially structured composite materials that can be engineered to have desired electromagnetic properties, while having other advantageous material properties [1].
- Structures composed of macroscopically scattering elements [2].
- Materials whose permeability and permittivity derive from their structure. [3]
- A new class of ordered nanocomposites that exhibit exceptional properties not readily observed in nature. These properties arise from qualitatively new response functions that are not observed in the constituent materials and result from the inclusion of artificially fabricated, extrinsic, low dimensional inhomogeneities [4].
- Macroscopic composites having a man-made, three dimensional, periodic cellular architecture designed to produce an optimized combination, not available in nature, of two or more responses to a specific excitation. Each cell contains metaparticles, macroscopic constituents designed with low dimensionality that allow each component of the excitation to be isolated and separately maximized.

> The metamaterial architecture is selected to strategically recombine local quasi-static responses, or to combine or isolate specific non-local responses [5].

Regarding such definitions, one can notice that two essential properties are mentioned. The materials should exhibit electromagnetic properties

- not observed in the constituent materials, and/or
- not observed in nature.

The notion of metamaterials, i.e., artificial materials with properties not available in nature, originated in the microwave community but has been quickly adopted in optics research, thanks to rapidly developing nanofabrication and subwavelength imaging applications. Metamaterials are expected to open a new gateway to unprecedented electromagnetic properties and functionalities that are unattainable from naturally occurring materials, i.e. unattainable if based just on what may happen at atomic or molecular level. The structural units of metamaterials can be tailored in shape and size; their composition and morphology can be artificially tuned, and inclusions can be designed and placed at desired locations to achieve new functionalities. In the broad sense defined above, the field of metamaterials includes a large range of engineered materials with predesigned properties. However, the notion of metamaterials was originally proposed in regard to the idea of a negative refractive index, or negative-index materials (NIMs), which are also referred to as left-handed materials (LHMs), double negative media (DNG) or backward-waves materials (BW). Indeed, the refractive index of a material gives the factor by which the phase velocity of waves is decreased in the material compared to vacuum. NIMs have a negative refractive index, so the phase velocity is directed against the flow of energy (or group velocity).

1.2.2 Veselago's materials and perfect lenses

In 1968, V.G. Veselago, a physicist from the Lebedjev Physical Institute in Moscow, theoretically investigated plane wave propagation in a mate-

rial whose permittivity and permeability were assumed to be simultaneously negative [6]. His theoretical study showed that for a monochromatic uniform plane wave in such a medium, the direction of the Poynting vector is antiparallel to the direction of phase velocity, contrary to the case of plane wave propagation in simple conventional media. Hence these media exhibit a negative group velocity and the wavevector $\vec{k}$ forms a left-handed set with the vectors $\vec{E}$ and $\vec{H}$.
As a consequence of this, Veselago also showed that in left-handed substances, the Doppler effect will be reversed, i.e. the red-shift occurs in approaching conditions and the blue-shift occurs when the source and receiver move away. The Cerenkov effect will also be reversed, i.e. the cone of radiation of a particle moving in a straight line will be directed backward relative to the motion of the particle.
Finally, another interesting property of LHMs is negative refraction. Indeed, according to Snell's law, a wave coming from a medium with a refractive index n_1, on the interface with a second medium with refractive index n_2 and an incidence angle i with respect to the normal at the interface will be refracted in the second medium with an angle r. And the following relation holds:

$$n_1 \cdot sin(i) = n_2 \cdot sin(r) \tag{1.1}$$

In the case where n_1 and n_2 would have opposite signs, it is clear that the refracted wave will be on the same side of the normal as the incident wave (Fig. 1.1). This is called "negative refraction".
But why would anyone try to build such materials? An interesting application of negative refraction is the so-called "flat lens". When a ray passes from a medium with a refracting index n_1 to a medium with refracting index $n_2 = -n_1$, the ray undergoes refraction at the interface between the two media, but there is no reflected ray. Considering a plate of thickness d with a refracting index $n_2 = -1$, placed in vacuum, it is possible to obtain a flat lens that reproduces at a given point the radiation from a point source, as shown in Fig. 1.2. This yields an almost perfect lens, with perfect focusing of the source. Indeed, unlike classical curved lenses made from regular transparent materials, planar metama-

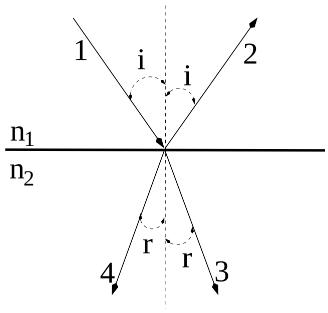

Figure 1.1: Passage of a ray through the boundary between two media. 1:Incident ray, 2:Reflected ray, 3:Refracted ray if the second medium is right-handed, 4:Refracted ray if the second medium is left-handed.

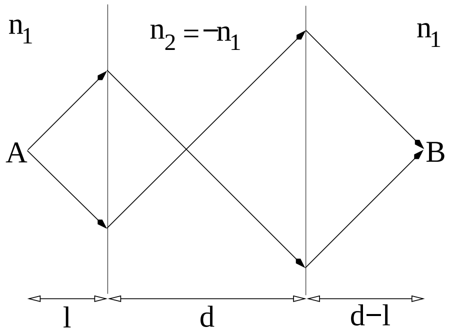

Figure 1.2: Passage of a ray through a plate of thickness d made of a left-handed material. A: Source of radiation, B: Focusing point.

terial lenses have no optical axis and reconstitute the near-field as well as the far-field of the source with sub-wavelength resolution. The sub-wavelength imaging property relies on the amplification of evanescent waves, which contain the high-resolution components of the image [9]. These lenses could be used in improved semiconductor lithography techniques and near-field imaging techniques. They could also be used for high capacity storage devices, such as DVDs. Finally, there would be a wide range of applications for materials that give rise to electromagnetic waves with "backward" properties. LHM are proposed for the design of compact novel filters, antennas and waveguides for use in wireless communications [7], [8].

1.2.3 Possible values of ϵ and μ

Fig. 1.3 shows a diagram with the values of ϵ and μ marked on the axes. The first quadrant contains the majority of isotropic dielectrics, for which both values of ϵ and μ are positive. These materials are right-handed and support forward-wave propagation. The second quadrant contains plasmas, for which the value of the permittivity is expressed as follows:

$$\epsilon \simeq 1 - \frac{\omega_p^2}{\omega^2} \text{ and } \omega < \omega_p \tag{1.2}$$

Where ω_p is the so-called "plasma frequency". It is obvious in Eq. 1.2 that at low frequencies, the permittivity is negative, which leads to reflection of waves from such media. Indeed, in this case, the refraction index is imaginary and waves are evanescent. The third quadrant is unoccupied in nature, there is indeed no substance in nature that exhibits both negative values of the magnetic permeability μ and the electric permittivity ϵ. However, Veselago showed that if it were possible to build such materials, they would exhibit a real but negative refraction index and that backward waves could propagate. Indeed, the complex refractive index of a given medium is defined as the ratio between the speed of an electromagnetic wave through that medium and that in vacuum and can thus be written as $n^2 = \epsilon\mu$, where μ is the complex relative magnetic permeability and ϵ, the complex relative dielectric permittivity. If both μ and ϵ are negative in a given wavelength range, this means that we may write $\mu = |\mu|e^{j\pi}$ and in an equivalent way $\epsilon = |\epsilon|e^{j\pi}$. It follows that

$$\begin{aligned} n &= \sqrt{|\epsilon||\mu|e^{2j\pi}} \\ &= \sqrt{|\epsilon||\mu|}e^{j\pi} \\ &= -\sqrt{|\epsilon||\mu|} \end{aligned} \tag{1.3}$$

Hence, the refractive index of a medium with simultaneously negative ϵ and μ must be negative. A more detailed consideration based on causality may be found in [10].

Finally, the fourth quadrant contains ferrimagnetic materials, such as ferrites and magnetic garnets. Again, in this case the refraction index is imaginary and waves cannot propagate.

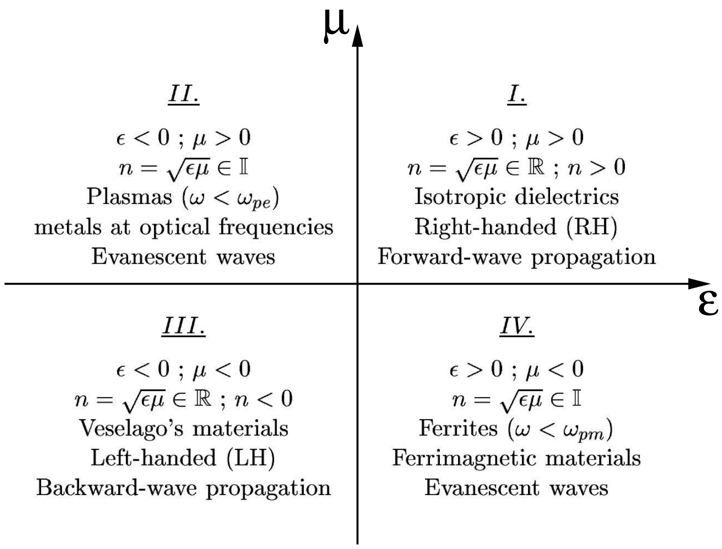

Figure 1.3: Diagram with theoretically possible values of ϵ and μ.

1.2.4 Realization of $\epsilon < 0$ and $\mu < 0$

Negative permittivity

In 1996 J. B. Pendry from the Imperial College London and his co-authors from the GEC-Marconi published a paper [11] about an artificial metallic construction, which exhibits negative permittivity. The understanding of this concept starts from the nature of the dielectric constant of metals [12]. The structure they proposed is made of a three-dimensional cubic lattice of metallic conducting wires with a periodicity smaller than the wavelength. This structure is depicted in Fig. 1.4 and can model the response of a diluted plasma, giving a negative ϵ below the plasma frequency (cf. Eq. 1.2). In other terms, the dilution offered by the reduction of the medium to wires allows to reduce the plasma frequency from optical to microwave frequencies.

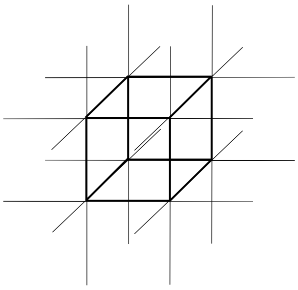

Figure 1.4: Periodic wire-frame structure for obtaining a negative ϵ. Thick lines are only shown for a better visualization of the structure.

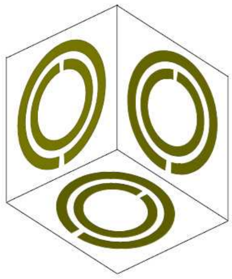

Figure 1.5: Unit cell of the split ring three-dimensional array used to obtain a negative μ

Negative permeability

In Veselago's days no negative-μ materials were known, nor thought likely to exist. But in 1999, Pendry and his co-authors published a solution to obtain a negative μ [13]. The idea is the same as for the negative ϵ, i.e. a periodic structure was proposed with a periodicity smaller than the wavelength of the exciting electromagnetic field. Then the average values of B and H were calculated and μ was determined as their ratio. The structure consists of a three dimensional array of split ring resonators (SRR). Each SRR is made of two concentric circles of metal, each of them being split. So the induced current can not close within one ring, but only in the capacitively coupled other one. The unit cell of this periodic structure is depicted in Fig. 1.5. This structure is resonant, and at frequencies slightly beyond the resonant frequency the mentioned average μ has a negative real part. The frequency behavior of the permeability can be expressed as follows [13]:

$$\mu(\omega) = 1 - \frac{F\omega^2}{\omega^2 - \omega_0^2 + j\nu\omega} \tag{1.4}$$

Where ω_0 is the resonant frequency of the SRRs, ν is a loss term and F depends on geometrical parameters of the lattice.

Figure 1.6: The double negative metamaterial used in the experimental verification at the University of California.

Combination of negative ϵ and μ

Until 1999, how to physically realize a material with simultaneously negative permittivity and permeability still remained a mystery. Then, Pendry, et. al., suggested that separate inclusions would provide each of the negative properties, permittivity and permeability. Smith, et. al. then suggested that interlacing the two lattices of carefully designed periodic arrays of conducting materials produced an amalgamation with simultaneously negative permittivity and permeability. Hence, in order to obtain a double negative material (DNG), and following these prescriptions, the idea was to build a periodic structure whose unit cell combines the unit cell of a metamaterial with a negative ϵ and the unit cell of another metamaterial with a negative μ. This has been done and the first experimental verification was made by Shelby, Smith and Schultz at the University of California in San Diego in 2001 [14]. The left-handed material was prepared by the standard shadow mask and etching circuit fabrication technique on 0.25mm thick fiber glass reinforced circuit board material. The structure consists of square split ring resonators and flat wire strips, both from copper. The rings and wires were on the opposite sides of the board. After processing, the boards were cut and assembled in an interlocking unit, which is shown in Fig. 1.6. The negative ϵ and μ occurred simultaneously at microwave frequencies between 10.2 GHz and 10.8 GHz and the verification of the negative index of refraction could be carried out for the first time.

1.3 Applications of metamaterials

Initially, the term metamaterial was used to describe artificial media possessing a left-handed behavior. However, this term is now accepted in a more general sense as engineered media whose electromagnetic responses are different from those of their constituent components. They are often generated by incorporating in a periodic manner various types of artificially fabricated, extrinsic, low dimensional inhomogeneities in some background substrate. Metamaterials that mimic known material responses or that qualitatively have new response functions that do not occur in nature have been realized. Some of these new artificial materials as well as their antenna related applications are described in this section.

1.3.1 Low ϵ metamaterials

As mentioned in section 1.2.4, some periodic structures made of conducting wires behave as a diluted plasma and hence, present a negative value of the permittivity below the plasma frequency (cf. Eq. 1.2). Looking at this equation, it is obvious that, in some frequency range, the permittivity can be close to zero. Hence, the refractive index of such structures is also close to zero and the energy radiated from an embedded source, when going out of the structure, will be refracted close to the normal with the interface with the outside medium. This property can be exploited to design high gain antennas. This is illustrated in Fig. 1.7, from [74], showing the electric field amplitude and phase in a structure made of parallel conducting wires and excited by an embedded monopole. The left picture shows clearly that the electric field outside the structure is indeed concentrated near the normal at the interface. On the right picture, one can see that the phase velocity inside the wire medium is very high (very small phase variation) and this is a proof that the refractive index is very low. The application of this phenomenon to high gain antennas will be discussed in section 5.1.

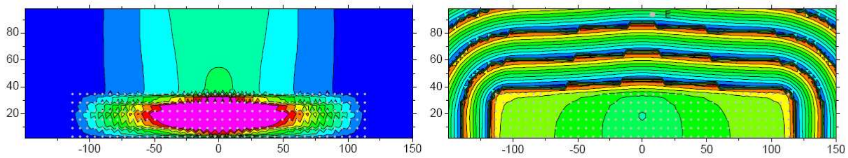

Figure 1.7: Amplitude (left) and lines of equal phase (right) in a structure made of parallel, infinite conducting wires excited by a small imbedded monopole. From [74].

1.3.2 High impedance surfaces and artificial magnetic conductors

Artificial magnetic conductors (AMCs) or high impedance surfaces, i.e. metamaterials that produce in-phase reflections are highly interesting for compact antenna solutions, in order to miniaturize and minimize the cost of communication components and systems. Such systems have already been transferred to the market and constitute an effective demonstration of the potential of metamaterials. A now well-known AMC design is the Sievenpiper class of mushroom high impedance surfaces [15]. An example of artificial perfect magnetic conductor (PMC) based on such a periodic mushroom-type structure will be discussed in section 3.4.2. Another application for high impedance surfaces is the improvement of radiation efficiency of patch antennas. Indeed, when designing patch antennas, compact circuit design is best achieved on high dielectric constant substrates. However, using these high permittivity dielectrics tends to increase surface waves phenomena and hence decreases the radiation efficiency. A solution to this problem consists of using PBG surfaces forbidding propagation of those surface waves (cf. Fig. 1.8).

1.3.3 Frequency selective reflection/transmission

Some metamaterials also exhibit frequency selective transmission characteristics and can be used to provide coatings with specific frequency filtering / reflection characteristics. This effort clearly originates from military applications (radomes, stealth planes, etc.), but has actually

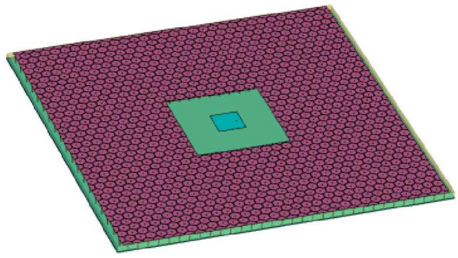

Figure 1.8: Patch antenna on a mushroom-type PBG ground plane to suppress surface waves and increase radiation efficiency.

important civil applications, especially in the field of electromagnetic compatibility (EMC) of civil devices like cell phones or providing colors or special optical effects on consumer goods. Frequency selective surfaces (FSS) or partially reflective surfaces (PRS) can also be used to design Fabry-Perot type resonators used to increase the gain of antennas. This application will be discussed in section 5.2.

1.3.4 Applications of DNG materials for small antennas

It has been shown [16] that surrounding an electrically small dipole antenna with a shell of double negative (DNG) material ($\epsilon < 0$ and $\mu < 0$) can increase the real power radiated by more than an order of magnitude over the corresponding free space case. Studies indeed shown that this electrically small antenna embedded in a DNG shell acts inductively rather than capacitively as it would in free space, hence, the DNG shell could act as a natural matching network for the dipole.

1.4 Numerical methods in electromagnetics

In electromagnetics, the starting point of all treatments are the four Maxwell's equations [17], which have to be solved for the corresponding geometries of the problems. Unfortunately, the majority of structures used today are complex enough to prevent their analytical resolution, and accurate computer-aided analysis and design tools have become essential. The requirements put on these methods are very severe since one wants them to be very efficient in terms of final results (typically when compared with measurements) and at the same time, not too CPU and memory intensive.

1.4.1 Overview of some classical methods

Finite Difference method

One of the very first techniques developed was the Finite Difference method (FD) [18]. The latter is often referred to as the least analytical one, since the mathematical processing it requires is minimal. However, this feature renders this method applicable to a wide range of complicated structures, as well as to frequency or time domain problems (FDTD) [19]. The overall principle is quite basic, since the idea is to solve a discretized version of the equation (Maxwell's, Laplace, wave equation, etc) instead of the equation itself. Hence, the first step in an FD approach is to define a mesh over the structure which allows for the expansion of various quantities (fields, potentials, etc), where derivatives are computed with the help of finite differences. The resulting matrices contain a lot of zeros, so they are in general inverted using special methods to speed up the process.

However, in its original version, the method was very inefficient for open structures, since it required to mesh the free-space region also, leading to unreasonable computation times. Nowadays, a lot of work has been dedicated to the investigation of proper absorbing layer conditions [20], [21], allowing the meshes to be limited to the immediate vicinity of the structures only. But nevertheless, many designs remain very challenging for FD methods (e.g. open media which are still better addressed by other methods), mainly because of the very large mesh they require, leading to large matrix equations and to excessive computational times. This major drawback seems to be the price to pay for the versatility of the method.

Finite Element Method

The Finite Element Method (FEM) [22] can be viewed as quite similar to FD methods but including variational features (the problem is in general replaced by a minimization problem of some functional) and, in general, a more flexible mesh. The drawback of this method appears again when applied to open structures since in this case, the region to analyze has to be truncated. This is not a trivial task since, in some situations, the fields may be slowly decaying and a bad truncation can result in strong errors. However, like for FD methods, this point is being extensively studied in the literature and one way to overcome it is to define proper absorbing boundary conditions [20], [21].

Mode Matching

As it can be seen, FD and FEM are two methods mainly based on numerical mathematics, in the sense that they approximate the operator of an equation by its discretized version.
The Mode Matching technique is based on more physical considerations, taking advantage of some peculiarities of the geometries to analyze. It is most typically applied to the problem of scattering into waveguide structures on both sides of a discontinuity. Actually, the name of the method is self-explanatory since it consists in matching the modes between two structures, and hence, should be applied to closed environments (where modes can indeed be defined). To do so, fields on both sides of the discontinuity are expanded in terms of modal functions with unknown coefficients, which are then matched by a proper application of the boundary conditions.

Transmission Line Matrix

The Transmission Line Matrix method (TLM) [23] is conceptually very similar to the FDTD method. Instead of discretizing the Maxwell's equations, an equivalent array of short transmission lines is used. This method is usually applied in the time domain, where the field problem is converted into a network problem in which the physical characteristics are matched onto electrical constraints (e.g. electric walls correspond to short- circuits and magnetic walls to open-circuits). Notice that after the time domain response has been obtained, the frequency domain one can be retrieved by a simple Fourier transformation.

Method of Moments

In the framework of this thesis, our main concern is to deal with open environments such as antennas or antenna arrays radiating into free-space. Thanks to the versatility of FD and FEM, such structures could be addressed by these two methods. The periodicity of the structures can be taken into account with the help of appropriate periodic boundary conditions applied to the fields on each side of the unit cell of the periodic structure. However, in order to avoid the heaviness of FD or FEM, researchers have built other techniques best suited for these media, based on more physical considerations. One of these techniques is the Method of Moments [28], used to solve integral equation formulations. Our approach is based on this method and the surface equivalence principle, where the fields are replaced by unknown equivalent electric and magnetic currents. Only surfaces need to be meshed (i.e. interfaces between different homogeneous media) instead of a whole volume, and this leads to less unknowns when compared to FD or FEM. This method will be described in details in Section 2.2.1. The periodicity of the structure can be taken into account with the help of periodic Green's functions, which are nothing else than a description of the fields radiated by a periodic array of point current sources (cf. Section 3.1).

1.5 Outline of this thesis

A description of our MoM simulation code will be given in Chapter 2. This description will be of tutorial nature. Before going deeply into the details of the numerical simulation code, general properties of electromagnetic fields will be recalled, such as the relations between fields and sources, the boundary conditions and the equivalence principle. Then the basics of the Method of Moments are explained, and it is shown how it can be used to solve the integral equations involved in scattering problems including metallic and dielectric objects. The integral formulations used to this purpose, respectively the EFIE and the PMCHWT approach are also explained. Finally, the accuracy of the code on finite structures is demonstrated on several validating examples.

Chapter 3 deals with infinitely periodic structures. Solving problems that involve large periodic structures such as metamaterials can be excessively time-consuming because of the large number of unknowns involved and the infinite-array approximation provides, in most situations, good estimates of the behavior of the fields in such structures. In infinite arrays, the periodicity is accounted for, thanks to the use of the periodic Green's function. Hence, this periodic Green's functions is first introduced, as well as efficient computation techniques for it and for its gradient. The infinite-array code is then validated on an example consisting of a self-complementary antenna array. Then, several applications of infinite-array simulations are shown, such as the computation of transmission and reflection properties of infinitely periodic structures. It is then shown how ohmic losses can be taken into account in the MoM simulation and the proposed approach is validated in the case of an infinite array of TEM horns. This validation is based on energy conservation. When dealing with metamaterials, one often needs to compute the response of a periodic structure to a non-periodic excitation. A way to achieve this is to resort to the so-called "Array Scanning Method" which is introduced in Section 3.6. An elegant convergence criterion, based on infinite array radiation pattern, is also proposed for the ASM. Then, the simulations involving dielectrics are validated on an infinite-array of dielectric spheres. To our best knowledge, our implementation is the only one for this kind of problems. Several ideas ensuring its efficiency will be discussed.

Finally, the last section of this chapter is dedicated to finite-by-infinite array simulations. In large arrays, the couplings between elements can be very strong, and the elements near the edges of the array can exhibit a strongly deviating behavior with respect to elements further inside that behave almost as if they were in an infinite-array. A first step in the prediction of the effects of truncation is to consider structures that are infinitely periodic in one direction and finite in the orthogonal direction. The basics of finite-by-infinite array simulations are first recalled and a fast iterative solution of the system of equations is presented. Then the application to the array truncation analysis is discussed and it is also shown how the Array Scanning Method can be used to estimate the element patterns of any element of a finite array. Finally, the application of the singly periodic Green's function to the analysis of infinite dielectric objects is presented.

Chapter 4 descibes how the dispersion curves of periodic structures can be computed numerically with our MoM code. This requires an efficient extension of our Green's function formulation to 3D periodic structures. The knowledge of these dispersion relations can be very helpful in the design of metamaterial based antennas. The computation technique is then demonstrated on the analysis of wire media. It will also be shown how, thanks to the computation of these curves, we were able to predict surprising properties for waveguides filled with wire media, such as the propagation of waves below the cut-off frequency of the fundamental mode.

Finally, Chapter 5 is dedicated to the application of all the previously mentioned techniques in the design of high gain antennas based on metamaterials. Two particular cases will be presented. The first one consists of a metallic EBG structure that exhibits a low refraction index and is used to collimate energy of a primary source. Then, the second example is about FSS superstrates creating some sort of Fabry-Perot resonator used to increase the gain of a slotted waveguide. For this second example, an efficient design method based on the separation of the structure in two different problems (one interior to the waveguide and an exterior one consisting of the superstrate) is proposed. In this method, the electric field in the slot is replaced by equivalent magnetic currents, and this allows fast separate optimizations of the radiation pattern and the input impedance, respectively in the exterior and interior problems.

Conclusions are then drawn in Chapter 6.

MoM based numerical simulation code

2

2.1 General relations between fields and sources

2.1.1 Fields radiated from sources

Maxwell's equations describe all classical electromagnetic phenomena and are expressed in the frequency domain as follows.

$$\nabla \times \vec{E} = -j\omega\mu\vec{H} \tag{2.1}$$

$$\nabla \times \vec{H} = \vec{J} + j\omega\epsilon\vec{E} \tag{2.2}$$

$$\nabla \cdot \vec{E} = \frac{1}{\epsilon}\rho \tag{2.3}$$

$$\nabla \cdot \vec{H} = 0 \tag{2.4}$$

In this work, media in which propagation is considered are homogeneous, i.e. the electric permittivity ϵ and the magnetic permeability μ are assumed to be constant, or at least piecewise constant when working with homogeneous dielectric objects. In order to evaluate fields from sources, it is convenient to work with electric and magnetic potentials rather than the $\vec{E}$ and $\vec{H}$ fields themselves. Two of Maxwell's equations allow us to introduce these potentials, then the other two, written in terms of these potentials take the form of a Helmoltz equation. The divergenceless $\vec{B}$ implies the existance of a vector potential $\vec{A}$ such as $\vec{B} = \nabla \times \vec{A}$. Hence, Eq. (2.1) can be written as:

$$\nabla \times (\vec{E} + j\omega\vec{A}) = 0 \tag{2.5}$$

Then, the curl-less quantity $\vec{E} + j\omega\vec{A}$ can be represented as the gradient of a scalar potential ϕ:

$$\vec{E} + j\omega\vec{A} = -\nabla\phi \tag{2.6}$$

Hence the fields are obtainable from these potentials by

$$\begin{aligned} \vec{E} &= -\nabla\phi - j\omega\vec{A} \\ \vec{B} &= \nabla \times \vec{A} \end{aligned} \tag{2.7}$$

The potentials $\vec{A}$ and ϕ are not uniquely defined. To ensure the uniqueness of these potentials, it is customary to impose the Lorenz condition:

$$\nabla \cdot \vec{A} = -j\omega\epsilon\mu\phi \tag{2.8}$$

Then we can use eqs. (2.7) and (2.8) in the remaining two Maxwell's equations.

$$\begin{aligned} \nabla \cdot \vec{E} &= \nabla(-\nabla\phi - j\omega\vec{A}) \\ &= -\nabla^2\phi - j\omega\nabla \cdot \vec{A} \\ &= -\nabla^2\phi + j^2\omega^2\epsilon\mu\phi \\ &= -\nabla^2\phi - k^2\phi \end{aligned}$$

Using the third Maxwell's equation (2.3), we obtain the Helmoltz equation for the scalar potential ϕ:

$$\nabla^2\phi + k^2\phi = -\frac{\rho}{\epsilon_0} \tag{2.9}$$

And similarly,

$$\begin{aligned} \nabla \times \vec{B} - j\omega\mu\vec{D} &= \nabla \times (\nabla \times \vec{A}) - j\omega\epsilon\mu(-\nabla\phi - j\omega\vec{A}) \\ &= \nabla \times (\nabla \times \vec{A}) + j\omega\epsilon\mu\nabla\phi - \omega^2\epsilon\mu\vec{A} \\ &= \nabla \times (\nabla \times \vec{A}) - \nabla \cdot \nabla \cdot \vec{A} - k^2\vec{A} \\ &= -\nabla^2\vec{A} - k^2\vec{A} \end{aligned} \tag{2.10}$$

Using the second Maxwell's equation (2.2), we obtain the Helmoltz equation for the vector potential $\vec{A}$:

$$\nabla^2\vec{A} + k^2\vec{A} = -\mu\vec{J} \tag{2.11}$$

Solving the Helmoltz equation yields the expressions for both scalar and vector potentials in terms of current and charge densities $\vec{J}$ and ρ

$$\phi(r) = \int_{V'} \frac{\rho(r')}{\epsilon} \frac{e^{-jkR}}{4\pi R} dV' \quad (2.12)$$

$$\vec{A}(r) = \int_{V'} \mu \vec{J}(r') \frac{e^{-jkR}}{4\pi R} dV' \quad (2.13)$$

With $R = |r - r'|$, the distance between observation and source points. These solutions may be written in the convolutional form:

$$\phi(r) = \int_{V'} \frac{\rho(r')}{\epsilon} G(r - r') dV' \quad (2.14)$$

$$\vec{A}(r) = \int_{V'} \mu \vec{J}(r') G(r - r') dV' \quad (2.15)$$

where $G(r)$ is the Green's function for the Helmoltz equation:

$$\nabla^2 G + k^2 G = -\delta(x)\delta(y)\delta(z) \quad \text{and} \quad G(r) = \frac{e^{-jkr}}{4\pi r} \quad (2.16)$$

With the help of the Lorenz condition the fields can be expressed completely in terms of the vector potential. Indeed, from (2.6) and (2.8) we get

$$\nabla \phi = \frac{-1}{j\omega\epsilon\mu} \nabla\nabla \cdot \vec{A}$$

Replacing this expression for the scalar potential in (2.6) finally yields the expression for the electric field.

$$\begin{aligned} \vec{E} &= -j\omega\vec{A} + \frac{1}{j\omega\epsilon\mu} \nabla\nabla \cdot \vec{A} \\ &= \frac{1}{j\omega\epsilon\mu}(-j^2\omega^2\epsilon\mu\vec{A} + \nabla\nabla \cdot \vec{A}) \\ &= \frac{1}{j\omega\epsilon\mu}(\frac{\omega^2}{c^2}\vec{A} + \nabla\nabla \cdot \vec{A}) \\ &= \frac{1}{j\omega\epsilon\mu}(k^2\vec{A} + \nabla\nabla \cdot \vec{A}) \end{aligned} \quad (2.17)$$

Where $k = \frac{\omega}{c}$ represents the free-space wavenumber. To summarize, with $\vec{A}(r)$ computed from Eq. (2.13), the $\vec{E}$ and $\vec{H}$ fields are obtained from

$$\vec{E} = \frac{1}{j\omega\epsilon\mu}(k^2\vec{A} + \nabla\nabla \cdot \vec{A}) \quad (2.18)$$

$$\vec{H} = \frac{1}{\mu} \nabla \times \vec{A} \quad (2.19)$$

2.1.2 Magnetic sources and duality

In addition to ordinary electric charge and current densities ρ and $\vec{J}$, we can also consider magnetic charges and current densities ρ_m and $\vec{M}$. Although the latter ones are fictitious and have no physical existance, they prove to be very helpful in some circumstances such as the study of aperture problems or scattering by dielectric objects. Introducing these new sources in Maxwell's equations leads to the so-called generalized form of Maxwell's equations:

$$\nabla \times \vec{E} = -\vec{M} - j\omega\mu\vec{H} \tag{2.20}$$

$$\nabla \times \vec{H} = \vec{J} + j\omega\epsilon\vec{E} \tag{2.21}$$

$$\nabla \cdot \vec{E} = \frac{1}{\epsilon}\rho \tag{2.22}$$

$$\nabla \cdot \vec{H} = \frac{1}{\mu}\rho_m \tag{2.23}$$

There is now complete symmetry, or duality, between the electric and the magnetic quantities. The solution of this new set of equations is obtained in terms of the usual scalar and vector potentials ϕ and A, as well as two new potentials ϕ_m and A_m.

$$\phi_m(\vec{r}) = \int_{V'} \frac{\rho_m(\vec{r'})}{\mu} G(\vec{r} - \vec{r'})dV' \tag{2.24}$$

$$\vec{A}_m(\vec{r}) = \int_{V'} \epsilon\vec{M}(\vec{r'})G(\vec{r} - \vec{r'})dV' \tag{2.25}$$

ϕ_m is called the magnetic scalar potential and $\vec{A}_m$ the electric vector potential. Hence the new expressions of $\vec{E}$ and $\vec{H}$ fields are now:

$$\vec{E} = -\nabla\phi - j\omega\vec{A} - \frac{1}{\epsilon}\nabla \times \vec{A}_m \tag{2.26}$$

$$\vec{H} = -\nabla\phi_m - j\omega\vec{A}_m + \frac{1}{\mu}\nabla \times \vec{A} \tag{2.27}$$

Using the Lorenz condition (2.8), the scalar potentials may be eliminated from these expressions as in Eq. (2.18) and (2.19). This yields the following expressions for $\vec{E}$ and $\vec{H}$, depending only on electric and magnetic vector potentials:

$$\vec{E} = \frac{1}{j\omega\epsilon\mu}(k^2\vec{A} + \nabla\nabla\cdot\vec{A}) - \frac{1}{\epsilon}\nabla\times\vec{A}_m \quad (2.28)$$

$$\vec{H} = \frac{1}{j\omega\epsilon\mu}(k^2\vec{A}_m + \nabla\nabla\cdot\vec{A}_m) + \frac{1}{\mu}\nabla\times\vec{A} \quad (2.29)$$

Using the expressions (2.15) and (2.25) for the vector potentials, the fields $\vec{E}$ and $\vec{H}$ can also be expressed directly in terms of the source currents $\vec{J}$ and $\vec{M}$:

$$\vec{E} = \int_{V'} \frac{k^2\overline{\overline{I}} + \nabla\nabla\cdot}{j\omega\epsilon}\left[\vec{J}\,G(\vec{r}-\vec{r'})\right] - \vec{M}\times\nabla' G(\vec{r}-\vec{r'})dV' \quad (2.30)$$

$$\vec{H} = \int_{V'} \frac{k^2\overline{\overline{I}} + \nabla\nabla\cdot}{j\omega\mu}\left[\vec{M}\,G(\vec{r}-\vec{r'})\right] + \vec{J}\times\nabla' G(\vec{r}-\vec{r'})dV' \quad (2.31)$$

Where $\overline{\overline{I}}$ is the identity matrix. These last expressions will be particularly useful in the development of the Method of Moment simulation code.

2.1.3 Boundary conditions

Maxwell's equations allow the computation of fields in homogeneous media. In such media, fields as well as their first and second derivatives are continuous. However, in order to determine the fields behavior at the interface between two media with different electromagnetic properties, these equations must be completed with boundary conditions along the interface. These boundary conditions express the field discontinuities in terms of surface currents and charge densities as follows:

$$\hat{n}\times(\vec{H}^{(1)} - \vec{H}^{(2)}) = \vec{J}_s \quad (2.32)$$

$$\hat{n}\times(\vec{E}^{(1)} - \vec{E}^{(2)}) = -\vec{M}_s \quad (2.33)$$

$$\hat{n}\cdot(\vec{E}^{(1)} - \vec{E}^{(2)}) = \frac{1}{\epsilon}\rho_s \quad (2.34)$$

$$\hat{n}\cdot(\vec{H}^{(1)} - \vec{H}^{(2)}) = \frac{1}{\mu}\rho_{ms} \quad (2.35)$$

Where $\hat{n}$ is the unit normal at the interface between media 1 and 2, pointing towards the medium 1.

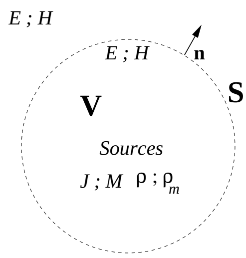

Figure 2.1: Volume V containing some sources and bounded by S.

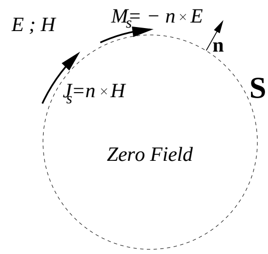

Figure 2.2: Surface currents produce the same field external to S as do the original sources.

2.1.4 Field equivalence principle

The Field equivalence principle [24] is at the heart of the MoM simulation and is recalled in this section. Many source distributions inside a given region can produce the same fields outside that region. Two sources producing the same field within a given region of space are said to be *equivalent within that region*. When we are interested in the field in a given region of space, we do not need to know the actual sources. Equivalent sources will serve as well. A simple application of this principle is depicted in Figs. 2.1 and 2.2. Fig.2.1 shows a volume V bounded by a closed surface S and containing electric and magnetic sources that produce electric and magnetic fields $\vec{E}$ and $\vec{H}$ inside and outside the volume V. A problem equivalent to the original problem external to S can be set up as follows. Let us assume that the original fields exist external to S but null fields internal to S. To support this field, boundary conditions on S imply that there must exist electric and magnetic surface currents $\vec{J}_s$ and $\vec{M}_s$ on S expressed as

$$\vec{J}_s = \hat{n} \times \vec{H} \quad \text{and} \quad \vec{M}_s = -\hat{n} \times \vec{E} \tag{2.36}$$

where $\hat{n}$ points outward V, $\vec{E}$ and $\vec{H}$ are respectively the original electric and magnetic fields along the boundary S. Fields outside V can be determined from these surface currents and, from the uniqueness theorem, we know that those fields are the originally postulated ones.

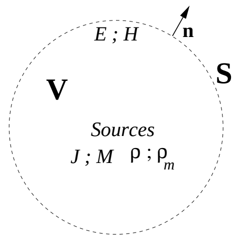

Figure 2.3: Volume V containing all the sources and bounded by S.

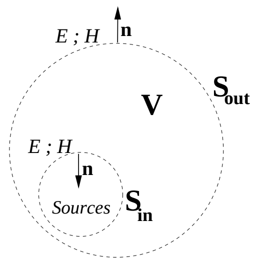

Figure 2.4: Sources outside the volume V.

2.1.5 Kottler's formulas and the surface field equivalence principle

The field equivalence principle can also be demonstrated mathematically starting from Kottler's formulas which in turn are obtained from the vector Green's second identity [25]. The Kottler's formulas [25] allow the electromagnetic field to be calculated at any point of a volume V, containing a homogeneous medium, from the volumic source densities $\vec{J}$, $\vec{M}$, ρ, and ρ_m, and from the values of the fields on the boundary S of V (Fig. 2.3).

$$\begin{aligned}\vec{E}(\vec{r}) = &\int_V (-j\omega\mu G\vec{J} - \vec{M} \times \nabla' G + \frac{\rho}{\epsilon}\nabla' G)\, dV \\ &- \int_S \left[-j\omega\mu G(\hat{n} \times \vec{H}) + (\hat{n} \times \vec{E}) \times \nabla' G + (\hat{n} \cdot \vec{E})\nabla' G\right] dS \end{aligned} \tag{2.37}$$

where $G(R)$ is the free-space Green's function with $R = |\vec{r} - \vec{r'}|$, $\vec{r}$ is the observation point and $\vec{r'}$, the integration point.

If one is interested in the fields outside the volume containing the sources, these formulas can still be used, assuming that surface S, volume V and the normals are defined as in figure 2.4. In this case, there are no sources within V and the volume integral vanishes. Moreover, if S_{out} recedes to infinity, the integral over S_{out} tends to zero. Hence Eq. (2.37) becomes:

$$\vec{E}(\vec{r}) = \int_{S_{in}} \left[-j\omega\mu G(\hat{n} \times \vec{H}) + (\hat{n} \times \vec{E}) \times \nabla' G + (\hat{n} \cdot \vec{E})\nabla' G\right] dS \tag{2.38}$$

It is more convenient to work only with tangential components of the fields, and it can be shown that (Appendix C):

$$\int_S (\hat{n} \cdot \vec{E}) \nabla' G \, dS = \frac{1}{j\omega\epsilon} \nabla\nabla \cdot \int_S (\hat{n} \times \vec{H}) G \, dS \tag{2.39}$$

Hence, equation (2.38) becomes

$$\vec{E}(\vec{r}) = \int_{S_{in}} \Big[- j\omega\mu G(\hat{n} \times \vec{H}) + (\hat{n} \times \vec{E}) \times \nabla' G + \frac{1}{j\omega\epsilon} \nabla\nabla \cdot \Big((\hat{n} \times \vec{H}) G \Big) \Big] dS \tag{2.40}$$

The electric and magnetic fields along S can be replaced by equivalent magnetic and electric currents respectively. These currents are defined as:

$$\vec{J}_{eq} = \hat{n} \times \vec{H} \tag{2.41}$$

$$\vec{M}_{eq} = -\hat{n} \times \vec{E} \tag{2.42}$$

and (2.40) finally reads:

$$\vec{E}(\vec{r}) = \int_{S_{in}} \left[\frac{k^2 \overline{\overline{I}} + \nabla\nabla\cdot}{j\omega\epsilon} \vec{J}_{eq} G - \vec{M}_{eq} \times \nabla' G \right] dS \tag{2.43}$$

It can be shown, thanks to the symmetry of generalized Maxwell's equations, that the H field reads:

$$\vec{H}(\vec{r}) = \int_{S_{in}} \left[\frac{k^2 \overline{\overline{I}} + \nabla\nabla\cdot}{j\omega\mu} \vec{M}_{eq} G + \vec{J}_{eq} \times \nabla' G \right] dS \tag{2.44}$$

Eqs. (2.43) and (2.44) are obviously equivalent to eqs. (2.30) and (2.31) where real source currents $\vec{J}$ and $\vec{M}$ would have been replaced by equivalent surface currents $\vec{J}_{eq}$ and $\vec{M}_{eq}$.

2.1.6 Note on the surface fields

We showed that eqs. (2.43) and (2.44) can be used to compute fields outside any volume V containing any source distribution under the condition that the surface S bounding V supports equivalent electric and magnetic currents defined in eqs. (2.41) and (2.42). However, if one is interested in the value of the fields *on* S, those integrals exhibit a discontinuity. To solve this problem, we use the following mathematical theorem (demonstrated in [25]), holding for any vector $\vec{A}$, S being a closed surface with exterior normal $\hat{n}$, G is the free space Green function and $\vec{r}_S$ is a point on S:

$$\begin{aligned}\lim_{\vec{r}\to\vec{r_S}} \int_S & \left[\left(\hat{n}(\vec{r'}) \times \vec{A}(\vec{r'})\right) \times \vec{\nabla}' G(\vec{r},\vec{r'}) + \left(\hat{n}(\vec{r'}) \cdot \vec{A}(\vec{r'})\right)\vec{\nabla}' G(\vec{r},\vec{r'})\right] dS \\ & = \pm\frac{1}{2}\vec{A}(\vec{r}_S) \\ & + \fint_S \left[\left(\hat{n}(\vec{r'}) \times \vec{A}(\vec{r'})\right) \times \vec{\nabla}' G(\vec{r}_S,\vec{r'}) + \left(\hat{n}(\vec{r'}) \cdot \vec{A}(\vec{r'})\right)\vec{\nabla}' G(\vec{r_S},\vec{r'})\right] dS\end{aligned} \tag{2.45}$$

with the negative sign if $\vec{r}_S$ is approached from the inside and the positive sign otherwise. And $\fint$ stands for principal value integration. The resulting integral over S is a principal value integral or Cauchy integral because it presents a singularity at the coordinate $\vec{r} = \vec{r}_S$. This principal value integral excludes the integrand over an infinitesimal surface element supporting the singularity. The numerical integration of such integrals will be discussed later. Applying this theorem to Eq. (2.38), and considering that $\vec{r}$ approaches $\vec{r}_S$ from outside, we finally get for the electric field on S:

$$\vec{E}(\vec{r}_S) = \fint_{S_{in}} \left[\frac{k^2\overline{\overline{I}} + \nabla\nabla\cdot}{j\omega\epsilon}\vec{J}_{eq}G - \vec{M}_{eq} \times \nabla' G\right] dS + \frac{\hat{n} \times \vec{M}_{eq}}{2} \tag{2.46}$$

and similarly for $\vec{H}$:

$$\vec{H}(\vec{r}_S) = \fint_{S_{in}} \left[\frac{k^2\overline{\overline{I}} + \nabla\nabla\cdot}{j\omega\mu}\vec{M}_{eq}G + \vec{J}_{eq} \times \nabla' G\right] dS - \frac{\hat{n} \times \vec{J}_{eq}}{2} \tag{2.47}$$

2.2 The Method of Moments

2.2.1 Principle

The Method of Moments (MoM) [28] is used to solve equations of the form:

$$\mathcal{L}f = g \tag{2.48}$$

where $\mathcal{L}$ is a linear integro-differential operator, g is a known excitation and f is the unknown function to be determined. The steps to solve equation (2.48) with the MoM are:

1. Choose a set of N expansion functions f_n and let f be expanded in a series of these functions:

$$f = \sum_n \alpha_n f_n \tag{2.49}$$

   where α_n are constants and the f_n are called *basis functions.*

2. Choose a set of N weighting functions w_m and define a suitable inner product $< .,. >$ for the problem. w_m are also called *testing functions.*

3. Take the inner product of Eq. (2.48) with each testing function.

$$\sum_n \alpha_n < \mathcal{L}f_n, w_m >=< g, w_m >$$

This yields a system of N equations with N unknowns α_n that can be written in matrix form:

$$[Z_{mn}][\alpha_n] = [g_m]$$

where

$$[Z_{mn}] = \begin{pmatrix} < \mathcal{L}f_1, w_1 > & < \mathcal{L}f_1, w_2 > & \dots \\ < \mathcal{L}f_2, w_1 > & < \mathcal{L}f_2, w_2 > & \dots \\ \vdots & \vdots & \ddots \end{pmatrix}, \ [\alpha_n] = \begin{pmatrix} \alpha_1 \\ \alpha_2 \\ \vdots \end{pmatrix}$$

$$[g_m] = \begin{pmatrix} < g, w_1 > \\ < g, w_2 > \\ \vdots \end{pmatrix}$$

If the matrix $[Z_{mn}]$ is not singular, the unknowns α_n are simply given by:

$$[\alpha_n] = [Z_{mn}]^{-1}[g_m]$$

and the unknown function f can be reconstructed using Eq. (2.49).
The convergence of the MoM is closely related to the choice of basis functions and, although to a lesser extend, to the choice of testing functions. There are essentially two families of basis functions:

Entire domain basis functions: using these functions to expand the unknowns is analogous to a Fourier expansion or to a modal expansion. These types of functions yield a good convergence of the method but are not versatile since the geometry need to be regular in order to have the modes defined. Note that in this case there is no need to mesh the geometry.

Sub-domain basis functions: they rely on a proper meshing of the geometry, which can be rectangular, triangular, etc. The choice of basis functions is here very wide, from Dirac, pulses , piecewise linear, higher orders, etc.

There are also two popular ways of choosing the testing functions:

Point matching: $w_m = \delta(\vec{r} - \vec{r}_m)$. In this case, Eq. (2.48) is exactly enforced at m points $\vec{r}_m$. It leads to a relatively simple evaluation of the inner product and to a rapid building of the impedance matrix, but generally leads to less accurate solutions that are very sensitive to the choice of the m points and the convergence of the MoM may not be optimal.

Galerkin testing: $w_m = f_m$. The testing functions are the same as the basis functions. With this choice Eq. (2.48) is enforced in an

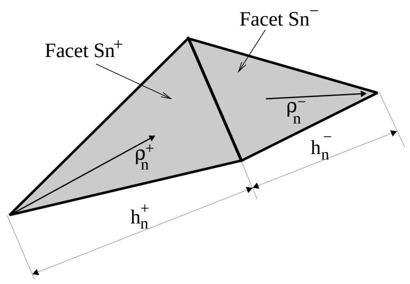

Figure 2.5: Geometry of the RWG basis function.

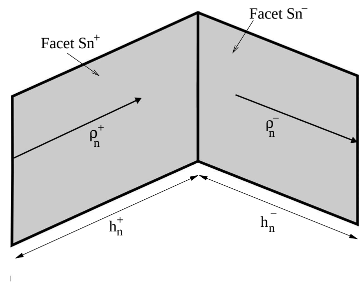

Figure 2.6: Geometry of the rooftop basis function.

average sense over the subdomains in which the N basis functions are defined.

2.2.2 Discretization: RWG and Rooftop basis functions

As shown in the previous section, in order to solve numerically the integral equations with the Method of Moments for any geometry, one first needs to discretize the surface in small non-overlapping sub-domains on which equivalent currents will be approximated. A very popular discretization is made of triangles, but in order to reduce the number of unknowns, we chose to include also the possibility to use rectangular subdomains (or parallelograms). Moreover, using rectangular shaped subdomains allows in some cases a better precision in current approximation because using rectangles sometimes allows to account for the symmetry in the simulated geometries. The meshes of the structures are generated by Gmsh [29], a three-dimensional mesh generator. A basis function will be associated to each interior edge of the discretization (i.e. not the boundary edges) and is to vanish everywhere except in the two facets attached to that edge. In the case of triangular facets, we used the well known Rao-Wilton-Glisson basis functions (RWG) [30], and for rectangular sub-domains, the Rooftop basis functions. These basis functions are defined as follows:

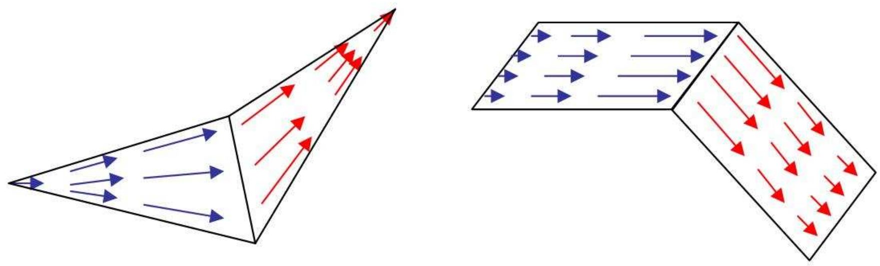

Figure 2.7: Illustration of vector fields defined in RWG and rooftop basis functions.

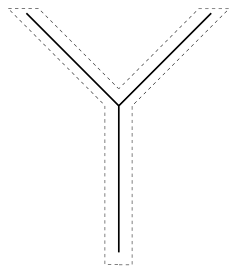

Figure 2.8: Metallic object surrounded by an imaginary closed surface

$$\vec{f}_n(\vec{r}) = \begin{cases} \vec{\rho_n^+}/h_n^+ & \text{if } \vec{r} \text{ is in } S_n^+ \\ \vec{\rho_n^-}/h_n^- & \text{if } \vec{r} \text{ is in } S_n^- \\ 0 & \text{elsewhere} \end{cases}$$

and are depicted in Figs. 2.5, 2.6 and 2.7. Note that hybrid basis functions are needed for edges belonging to both triangular and rectangular facets.

2.2.3 Scattering by metallic objects: solving the EFIE

In order to compute the scattering by a metallic object, the surface equivalence principle can be used. The body is then removed and replaced by fictitious electric and magnetic currents flowing on a surface S enclosing the object (Fig. 2.8). The knowledge of these currents is sufficient to compute all the scattered fields. The problem can be simplified if the surface S is taken infinitely close to the metallic surface. Indeed, if ohmic losses are neglected, in that case the boundary conditions along S are those applicable at the surface of a PEC object:

$$\hat{n} \times \vec{E} = 0 = \vec{M}_{eq} \tag{2.52}$$

$$\hat{n} \times \vec{H} = \vec{J} = \vec{J}_{eq} \tag{2.53}$$

The tangential electric field along S is null as well as the equivalent magnetic currents and one only need to solve for equivalent electric currents which in this particular case will correspond to physical currents flowing on the metallic surface. Hence, Eq. (2.46) simplifies to:

$$\vec{E}(\vec{r}) = \frac{1}{j\omega\epsilon} \int_S \left[k^2 \vec{J} G + \nabla\nabla \cdot (\vec{J} G) \right] dS \tag{2.54}$$

Where the equivalent magnetic currents are omitted. In the more general case where there would be an incident electric field $\vec{E}_i(\vec{r})$ on the structure, this equation can be rewritten:

$$\begin{aligned} \vec{E}(\vec{r}) &= \vec{E}_i(\vec{r}) + \frac{1}{j\omega\epsilon} \int_S \left[k^2 \vec{J} G + \nabla\nabla \cdot (\vec{J} G) \right] dS & (2.55) \\ &= \vec{E}_i(\vec{r}) + \vec{E}_s(\vec{r}) & (2.56) \end{aligned}$$

Where $\vec{E}_s(\vec{r})$ is the scattered electric field.
By enforcing condition (2.52), we obtain the electric field integral equation (EFIE):

$$\hat{n} \times \vec{E}_s(\vec{r}) = -\hat{n} \times \vec{E}_i(\vec{r}) \tag{2.57}$$

which can be rewritten:

$$\frac{1}{j\omega\epsilon} \hat{n} \times \int_S \left[k^2 \vec{J} G + \nabla\nabla \cdot (\vec{J} G) \right] dS = -\hat{n} \times \vec{E}_i(\vec{r}) \tag{2.58}$$

To solve this equation, the unknown surface currents $\vec{J}$ are dicretized using N weighted basis functions and can be written:

$$\vec{J}(\vec{r}) = \sum_{i=1}^{N} a_i \vec{J}_i(\vec{r})$$

In order to get N equations, the testing procedure consists of enforcing the boundary conditions *in an average sense* by taking the dot product of both sides of Eq. (2.58) with N testing functions $\vec{w}_j(\vec{r})$:

$$\int_S \vec{w}_j(\vec{r}) \cdot \vec{E}_s(\vec{r}) = -\int_S \vec{w}_j(\vec{r}) \cdot \vec{E}_i(\vec{r})$$

In the Galerkin testing procedure, the testing and basis functions are the same : $\vec{w}_j(\vec{r}) = \vec{J}_j(\vec{r})$, and we get N linear equations with the unknowns a_i:

$$\frac{1}{j\omega\epsilon}\sum_{i=1}^{N} a_i \int_S \vec{J}_j(\vec{r})\cdot(k^2\overline{\overline{I}}+\nabla\nabla\cdot)\int_{S'}\vec{J}_i(\vec{r'})G(R)dS'dS = -\int_S \vec{J}_j(\vec{r})\cdot\vec{E}_i(\vec{r}) \tag{2.59}$$

with $j = 1...N$.

Note that the cross-product with the unit normal $\hat{n}$ is no longer necessary as the normal component of fields is automatically omitted thanks to the dot-product with testing functions. One should also notice that, in the case of thin PEC structures, the computed current implicitly is the sum of currents on both sides of the metallic sheets.

Computation of the impedance matrix elements

Using Eq. (2.59), one can see that the MoM impedance matrix elements can be computed as follows:

$$Z_{mn} = \frac{1}{j\omega\epsilon}\int_S \vec{J}_m \cdot (k^2\overline{\overline{I}} + \nabla\nabla\cdot)\int_{S'} \vec{J}_n G(R)\, dS' dS$$

Where $\vec{J}_n$ are the basis functions and $\vec{J}_m$, the testing functions.

By distributing the $\nabla\nabla\cdot$ operator on the basis and testing functions, this expression can be rewritten:

$$Z_{mn} = \frac{1}{j\omega\epsilon}\left[\int_S\int_{S'}\left(k^2\vec{J}_m\cdot\vec{J}_n - (\nabla\cdot\vec{J}_m)(\nabla\cdot\vec{J}_n)\right)G(R)dS'dS\right] \tag{2.61}$$

where $\nabla\cdot\vec{J}_m = \nabla\cdot\vec{J}_n = 2/h$ for triangular basis funtions and $\nabla\cdot\vec{J}_m = \nabla\cdot\vec{J}_n = 1/h$ for rectangular ones. h is the height of the basis functions, as shown in Figs 2.5 and 2.6.

Details on how to obtain this expression can be found in Appendix B.

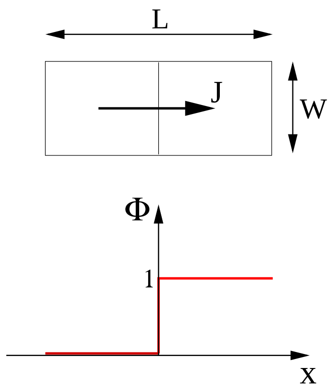

Figure 2.9: Schematic view of a basis function supporting a delta-gap excitation.

Computing the excitation vector

Delta-gap excitation: Right member of equation (2.59) is nul everywhere except for the basis function supporting the delta-gap. So the excitation vector has only one element that is non zero, the element corresponding to the basis function supporting the delta-gap. The electric field along the basis function supporting the delta-gap (cf. Fig. 2.9) writes:

$$\vec{E}_i(x) = -\nabla\phi(x) = -\delta(x)$$

hence

$$\begin{aligned} g_m = -\int_{S_m} \vec{E}_i \cdot \vec{J}_m dS &= -\int_0^W \int_{-L/2}^{L/2} -J_m(x)\delta(x)dx\, dy \\ &= W J_m(0) \\ &= W \end{aligned}$$

Where S_m is the surface of the m^{th} basis function.

Plane wave excitation: In this case, all the elements of the excitation vector must be computed. Assuming an incident plane wave coming from the direction (θ, ϕ), the incident electric field writes

$$\vec{E}_i = \vec{E}_0\, e^{j\vec{k}\cdot\vec{r}}$$

Where $\vec{k}$ is the wave vector for the incident wave:

$$\vec{k} = \frac{2\pi}{\lambda}\big(\sin\theta\cos\phi, \sin\theta\sin\phi, \cos\theta\big)$$

Hence, assuming that the amplitude of the electric field is $|\vec{E}_0| = 1\ V/m$, the elements of the excitation vector are:

$$g_m = -\int_{S_m} e^{j\vec{k}\cdot\vec{r}}\,\vec{e}_p\cdot\vec{J}_m\,dS$$

Where $\vec{e}_p$ is the polarization of the electric field.

2.2.4 Scattering by dielectric objects: PMCHWT formulation

The body is removed and replaced by fictitious equivalent currents on the interface [24]. These equivalent currents are expressed respectively as $\vec{J} = \vec{n}\times\vec{H}$ and $\vec{M} = -\vec{n}\times\vec{E}$, where $\vec{n}$ is the unit normal pointing outward the object and $\vec{E}$ and $\vec{H}$ are the electric and magnetic fields. The knowledge of these currents is sufficient to compute the fields scattered by the object. They can be determined by ensuring the continuity of scattered fields at the object surface. Assuming incident fields $\vec{E}_{inc}$ and $\vec{H}_{inc}$, the fields outside the dielectric body computed from equivalent currents are written:

$$\vec{E}_{out}(\vec{r}) = \vec{E}_{inc}(\vec{r}) + \int_S \left[\frac{k_{out}^2 + \nabla\nabla\cdot}{j\omega\epsilon_{out}}(\vec{J}G_{out}) - \vec{M}\times\nabla' G_{out}\right] dS \quad (2.62)$$

$$\vec{H}_{out}(\vec{r}) = \vec{H}_{inc}(\vec{r}) + \int_S \left[\frac{k_{out}^2 + \nabla\nabla\cdot}{j\omega\mu_{out}}(\vec{M}G_{out}) + \vec{J}\times\nabla' G_{out}\right] dS \quad (2.63)$$

Where $\vec{J}$ and $\vec{M}$ are the unknown equivalent electric and magnetic currents, S is the interface between the dielectric body and the outside medium, and G_{out} is the free-space Green's function for the outside medium. Inside the dielectric object, fields are expressed as:

$$\vec{E}_{in}(\vec{r}) = -\int_S \left[\frac{k_{in}^2 + \nabla\nabla\cdot}{j\omega\epsilon_{in}}(\vec{J}G_{in}) - \vec{M}\times\nabla' G_{in}\right] dS \quad (2.64)$$

$$\vec{H}_{in}(\vec{r}) = -\int_S \left[\frac{k_{in}^2 + \nabla\nabla\cdot}{j\omega\mu_{in}}(\vec{M}G_{in}) + \vec{J}\times\nabla' G_{in}\right] dS \tag{2.65}$$

The negative sign in Eq. (2.64) and (2.65) is due to the fact that equivalent currents, as seen from inside the dielectrics, have an opposite sign to those seen from outside. G_{in} is the Green's function for the medium inside the dielectrics. One should recall that when fields are evaluated on the surface of the dielectric body, the integrals involved in Eqs. (2.62) to (2.65) are singular and must be evaluated as in Eqs. (2.46) and (2.47). These two set of equations are then completed with the boundary conditions enforcing the continuity of tangential fields along the surface of the dielectric object.

$$\vec{n}\times\vec{E}_{in} = \vec{n}\times\vec{E}_{out} \tag{2.66}$$

$$\vec{n}\times\vec{H}_{in} = \vec{n}\times\vec{H}_{out} \tag{2.67}$$

Introducing Eqs. (2.62) to (2.65) in these expressions yields the integral equations for the electric and magnetic fields::

$$\begin{aligned}\vec{n}\times\Bigg(\vec{E}_{inc} + \frac{k_{in}^2\overline{\overline{I}} + \nabla\nabla\cdot}{j\omega\epsilon_{in}}\int_S G_{in}\vec{J}dS + \frac{k_{out}^2\overline{\overline{I}} + \nabla\nabla\cdot}{j\omega\epsilon_{out}}\int_S G_{out}\vec{J}dS \\ -\int_S \vec{M}\times\nabla'(G_{in}+G_{out})dS\Bigg) = 0\end{aligned} \tag{2.68}$$

$$\begin{aligned}\vec{n}\times\Bigg(\vec{H}_{inc} + \frac{k_{in}^2\overline{\overline{I}} + \nabla\nabla\cdot}{j\omega\mu_{in}}\int_S G_{in}\vec{M}dS + \frac{k_{out}^2\overline{\overline{I}} + \nabla\nabla\cdot}{j\omega\mu_{out}}\int_S G_{out}\vec{M}dS \\ +\int_S \vec{J}\times\nabla'(G_{in}+G_{out})dS\Bigg) = 0\end{aligned} \tag{2.69}$$

Computation of the impedance matrix elements

Let us define

$$\vec{E}_{in}^J = -\frac{k_{in}^2\overline{\overline{I}} + \nabla\nabla\cdot}{j\omega\epsilon_{in}}\int_S G_{in}\vec{J}dS \tag{2.70}$$

$$\vec{E}_{out}^J = \frac{k_{out}^2\overline{\overline{I}} + \nabla\nabla\cdot}{j\omega\epsilon_{out}}\int_S G_{out}\vec{J}dS \tag{2.71}$$

the electric field inside and outside the dielectric object radiated by electric currents and

$$\vec{E}_{in}^{M} = \oint_S \vec{M} \times \nabla' G_{in} dS \tag{2.72}$$

$$\vec{E}_{out}^{M} = -\oint_S \vec{M} \times \nabla' G_{out} dS \tag{2.73}$$

the electric field inside and outside the dielectric object radiated by magnetic currents. And similar definitions for the magnetic field:

$$\vec{H}_{in}^{J} = -\oint_S \vec{J} \times \nabla' G_{in} dS \tag{2.74}$$

$$\vec{H}_{out}^{J} = \oint_S \vec{J} \times \nabla' G_{out} dS \tag{2.75}$$

$$\vec{H}_{in}^{M} = -\frac{k_{in}^2 \overline{\overline{I}} + \nabla\nabla\cdot}{j\omega\mu_{in}} \int_S G_{in} \vec{M} dS \tag{2.76}$$

$$\vec{H}_{out}^{M} = \frac{k_{out}^2 \overline{\overline{I}} + \nabla\nabla\cdot}{j\omega\mu_{out}} \int_S G_{out} \vec{M} dS \tag{2.77}$$

Eqs. (2.68) and (2.69) can be rewritten:

$$\vec{n} \times \left(\vec{E}_{out}^{J} + \vec{E}_{out}^{M} - \vec{E}_{in}^{J} - \vec{E}_{in}^{M} \right) = -\vec{n} \times \vec{E}_{inc} \tag{2.78}$$

$$\vec{n} \times \left(\vec{H}_{out}^{J} + \vec{H}_{out}^{M} - \vec{H}_{in}^{J} - \vec{H}_{in}^{M} \right) = -\vec{n} \times \vec{H}_{inc} \tag{2.79}$$

These equation are tested by taking the dot product with testing functions $\vec{J}_m$ and omitting the cross product with the normal $\vec{n}$, which is no longer necessary.

$$\int_S \left(\vec{E}_{out}^{J} + \vec{E}_{out}^{M} - \vec{E}_{in}^{J} - \vec{E}_{in}^{M} \right) \cdot \vec{J}_m dS = -\int_S \vec{E}_{inc} \cdot \vec{J}_m dS \tag{2.80}$$

$$\int_S \left(\vec{H}_{out}^{J} + \vec{H}_{out}^{M} - \vec{H}_{in}^{J} - \vec{H}_{in}^{M} \right) \cdot \vec{J}_m dS = -\int_S \vec{H}_{inc} \cdot \vec{J}_m dS \tag{2.81}$$

If the object's surface is discretized using N basis functions for electric currents and N for magnetic currents:

$$\vec{J} = \sum_{n=1}^{N} \alpha^J \vec{J}_n \tag{2.82}$$

$$\vec{M} = \sum_{n=1}^{N} \alpha^M \vec{J}_n \tag{2.83}$$

$$\tag{2.84}$$

This procedure yields a set of $2N$ equations that can be put in matrix form. The impedance matrix has now 4 distinct blocks:

$$[Z_{mn}] = \begin{pmatrix} \mathbf{Z^{EJ}} & \mathbf{Z^{EM}} \\ \mathbf{Z^{HJ}} & \mathbf{Z^{HM}} \end{pmatrix}$$

The elements in the EJ and HM blocks are similar to those of the impedance matrix for a metallic object and can be computed as described in Section 2.2.3.

$$\begin{aligned}
Z_{mn}^{EJ} &= \int_S (\vec{E}_{out}^J - \vec{E}_{in}^J) \cdot \vec{J}_m dS \\
&= \int_S \left[\frac{k_{in}^2 \overline{\overline{I}} + \nabla\nabla\cdot}{j\omega\epsilon_{in}} \int_{S'} G_{in} \vec{J}_n dS' \right. \\
&+ \left. \frac{k_{out}^2 \overline{\overline{I}} + \nabla\nabla\cdot}{j\omega\epsilon_{out}} \int_{S'} G_{out} \vec{J}_n dS' \right] \cdot \vec{J}_m dS \qquad (2.86)
\end{aligned}$$

$$\begin{aligned}
Z_{mn}^{HM} &= \int_S (\vec{H}_{out}^M - \vec{H}_{in}^M) \cdot \vec{J}_m dS \\
&= \int_S \left[\frac{k_{in}^2 \overline{\overline{I}} + \nabla\nabla\cdot}{j\omega\mu_{in}} \int_{S'} G_{in} \vec{J}_n dS' \right. \\
&+ \left. \frac{k_{out}^2 \overline{\overline{I}} + \nabla\nabla\cdot}{j\omega\mu_{out}} \int_{S'} G_{out} \vec{J}_n dS' \right] \cdot \vec{J}_m dS \qquad (2.87)
\end{aligned}$$

$$\begin{aligned}
Z_{mn}^{EM} &= \int_S (\vec{E}_{out}^M - \vec{E}_{in}^M) \cdot \vec{J}_m dS \\
&= -\int_S \int_{S'} \vec{J}_n \times \nabla'(G_{in} + G_{out}) dS' \cdot \vec{J}_m dS \qquad (2.88)
\end{aligned}$$

$$\begin{aligned}
Z_{mn}^{HJ} &= \int_S (\vec{H}_{out}^J - \vec{H}_{in}^J) \cdot \vec{J}_m dS \\
&= \int_S \int_{S'} \vec{J}_n \times \nabla'(G_{in} + G_{out}) dS' \cdot \vec{J}_m dS \qquad (2.89)
\end{aligned}$$

Striking is the fact that the integrals involved in EJ and HM blocks of the impedance matrix are almost identical as well as those in EM and HJ blocks.

The vector of unknown currents is organized as follows:

$$[\alpha_n] = \begin{pmatrix} \alpha^{\mathbf{J}} \\ \alpha^{\mathbf{M}} \end{pmatrix}$$

where $\alpha^{\mathbf{J}}$ is a vector with unknown electric currents and $\alpha^{\mathbf{M}}$ with unknown magnetic currents. The excitation vector contains the impressed E and H fields on every basis functions.

$$[g_m] = \begin{pmatrix} \mathbf{g}^{\mathbf{E}} \\ \mathbf{g}^{\mathbf{H}} \end{pmatrix}$$

2.2.5 Evaluation of the integrals, treatment of singularities

As seen in the previous section, the computation of the MoM impedance matrix elements requires the evaluation of several surface integrals. These can be carried out with the help of numerical methods called *quadratures*. They consist of approximating the integral over a domain S by a summation of integrand samples. Each sample point has a weighting coefficient associated with it.

$$\int_S f(x,y)dx\ dy \approx S \sum_i w_i f(x_i, y_i) \tag{2.90}$$

Where S is the area of the domain, N is the total number of integrand sample points and w_i is the weighting coefficient associated to the sample point (x_i, y_i). In our case, these quadratures are performed over triangular and rectangular domains, respectively for RWG and Rooftop basis functions. For triangular domains, Dunavant [32] quadratures are used and Gauss-Legendre quadratures for rectangular domains.
However, the presence of the Green's function $G(R)$, in the integrand way cause numerical problems when the point samples on the basis and testing functions are close from each other (R is then close to zero). Indeed, as shown by Eq. (2.91) the real part of the Green's function exhibit a $1/R$ singularity at the origin.

$$\begin{aligned} G(R) &= \frac{e^{-jkR}}{4\pi R} \\ &= \frac{1}{4\pi}\left(\frac{1}{R} - jk - \frac{k^2}{2}R + j\frac{k^3}{6}R^2 + O[R^4]\right) \end{aligned} \tag{2.91}$$

Moreover, when dealing with dielectric objects, the gradient of the Green's function appear in the integrals of the PMCHWT formulation (Section

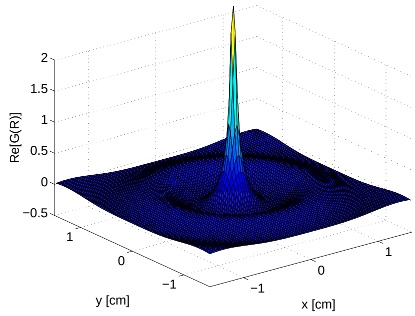

Figure 2.10: Amplitude of the free-space Green's function ($\lambda = 1$ cm).

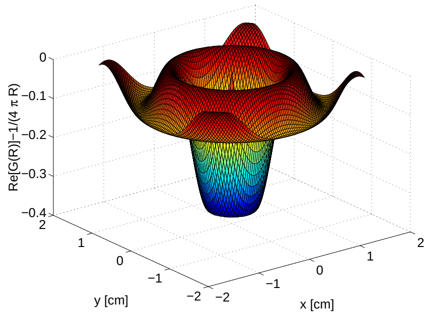

Figure 2.11: Amplitude of the free-space Green's function with $1/R$ singularity extracted ($\lambda = 1$ cm).

2.2.4). And this gradient contains a double singularity at the origin. One behaves also as $1/R$ and the other one as $1/R^3$, as shown by Eq. (2.92).

$$\begin{aligned}\nabla G(R) &= \frac{(1-jkR)e^{-jkR}}{4\pi R^3}\vec{R} \\ &= \frac{1}{4\pi}\left(\frac{1}{R^3}+\frac{k^2}{2}\frac{1}{R}-j\frac{k^3}{3}-\frac{k^4}{8}R+O[R^2]\right)\vec{R} \qquad (2.92)\end{aligned}$$

The integrals involved in the MoM become very difficult to evaluate accurately on a domain in which R is small because of the steepness of the Green's function and it's gradient around $R = 0$. An elegant approach to overcome this problem is to perform the extraction of the singularities. These singularities are substracted from the Green's function and its gradient before the numerical integration. They are then integrated analytically over the basis function, and numerically over the testing function.

The $1/R$ singularity

As shown by Eq. (2.61), the elements of the MoM impedance matrix are written as follows:

$$Z_{mn} = \int_S \int_{S'} f(\vec{r}, \vec{r'}) G(\vec{r}, \vec{r'}) dS' dS \tag{2.93}$$

where $f(\vec{r}, \vec{r'}) = \frac{1}{j\omega\epsilon} \left(k^2 \vec{J}_m \cdot \vec{J}_n - (\nabla \cdot \vec{J}_m)(\nabla \cdot \vec{J}_n) \right)$.
The principle of singularity extraction is to decompose this integral in two parts : a first one I_{NS} in which the singularities have been extracted and a second one I_S containing the singularities.

$$\begin{aligned} Z_{mn} &= I_{NS} + I_S \\ &= \int_S \int_{S'} f(\vec{r}, \vec{r'}) \left[G(\vec{r}, \vec{r'}) - \frac{1}{4\pi R} \right] dS' dS + \int_S \int_{S'} f(\vec{r}, \vec{r'}) \frac{1}{4\pi R} dS' dS \end{aligned} \tag{2.94}$$

Where $R = |\vec{r} - \vec{r'}|$. The first term (I_{NS}) can now be easily evaluated numerically with a very good accuracy. Depending on the actual (small) value of R it might be preferable to use a Taylor approximation of the Green's function (cf. Eq. 2.91) in this term in order to avoid substracting huge numbers. The inner integral of the second term I_S will be evaluated analytically over the basis function $\vec{J}_n(\vec{r'})$ and the result is then integrated numerically over the testing function $\vec{J}_m(\vec{r})$. Looking at the expression for I_S, one can see that two different analytical integrals must be computed:

1. $$\int_{S'} \frac{1}{4\pi R} dS' \tag{2.95}$$

2. $$\int_{S'} \frac{\vec{J}_n}{4\pi R} dS' \tag{2.96}$$

The analytical expression for the first integral (2.95) over polygons can be found in [33] under the form of line integrals. The second expression (2.96) however needs a little rewriting depending on the type of basis

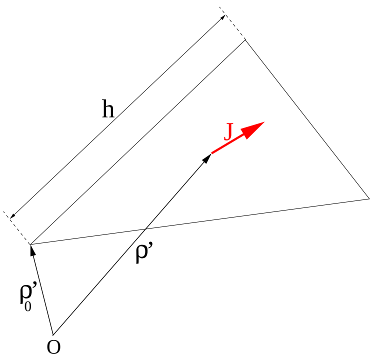

Figure 2.12: Current in triangular basis functions.

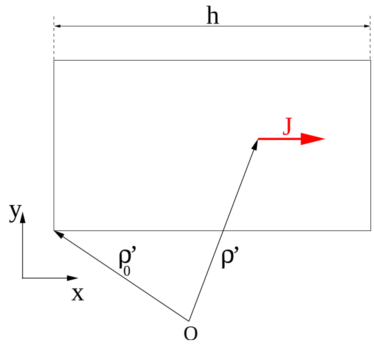

Figure 2.13: Current in rectangular basis functions.

function. In the case of a triangular basis function, the basis function is expressed as follows (cf. Section 2.2.2):

$$\vec{J}_n(\vec{r'}) = \frac{\vec{\rho'} - \vec{\rho'}_0}{h}$$

Where $\vec{\rho'}$ is the projection in the plane of the basis function of the vector $\vec{r'}$ where the current is computed, $\vec{\rho'}_0$ is the projection of the vector pointing to the origin of the basis function (triangle summit) and h is the height of the triangle (cf. Fig. 2.12). Hence, expression (2.96) can be rewritten:

$$\begin{aligned}
\int_{S'} \frac{\vec{J}_n}{4\pi R} dS' &= \frac{1}{4\pi h} \int_{S'} \frac{\vec{\rho'} - \vec{\rho'}_0}{R} dS' \\
&= \frac{1}{4\pi h} \int_{S'} \frac{\vec{\rho'} - \vec{\rho}}{R} dS' + \frac{1}{4\pi h} \int_{S'} \frac{\vec{\rho} - \vec{\rho'}_0}{R} dS' \\
&= \frac{1}{4\pi h} \int_{S'} \frac{\vec{\rho'} - \vec{\rho}}{R} dS' + \frac{\vec{\rho} - \vec{\rho'}_0}{4\pi h} \int_{S'} \frac{1}{R} dS' \qquad (2.97)
\end{aligned}$$

The expression for $\int_{S'} \frac{\vec{\rho'} - \vec{\rho}}{R} dS'$ can also be found in [33].
A similar derivation can be done in case of rectangular basis function. Assuming for the sake of simplicity that the rectangle has its edges parallel to x and y axis, the current is expressed (Fig. 2.13):

$$\vec{J}_n(\vec{r'}) = \frac{\vec{\rho'} - \vec{\rho'}_0}{h} \cdot \hat{x}$$

And expression (2.96) can be rewritten:

$$\begin{aligned}\int_{S'} \frac{\vec{J}_n}{4\pi R} dS' &= \frac{1}{4\pi h} \int_{S'} \frac{\vec{\rho'}_x - \vec{\rho'}_{0x}}{R} dS' \\ &= \frac{1}{4\pi h} \int_{S'} \frac{\vec{\rho'}_x - \vec{\rho}_x}{R} dS' + \frac{1}{4\pi h} \int_{S'} \frac{\vec{\rho}_x - \vec{\rho'}_{0x}}{R} dS' \\ &= \frac{1}{4\pi h} \int_{S'} \frac{\vec{\rho'}_x - \vec{\rho}_x}{R} dS' + \frac{\vec{\rho}_x - \vec{\rho'}_{0x}}{4\pi h} \int_{S'} \frac{1}{R} dS' \end{aligned} \quad (2.98)$$

where the subscript x means that only the x component of the vector is concerned.

The $1/R^3$ singularity

As previously mentioned, when dealing with dielectric objects the gradient of the Green's function appear in the integrals of the PMCHWT formulation (Section 2.2.4). And looking at the expression (2.92) of this gradient, one can note that in addition to the $1/R$ type singularity, a $1/R^3$ singularity now also needs to be treated. In the case of triangular basis functions, this can be done by using similar techniques as for the $1/R$ singularity and the analytical expression for the two following integrals (2.99) and (2.100) can be found in [34].

$$\int_{S'} \frac{1}{R^3} dS' \quad (2.99)$$

$$\int_{S'} \frac{\vec{\rho'} - \vec{\rho}}{R^3} dS' \quad (2.100)$$

However, the case of rectangular basis functions cannot be found in the literature and is treated as follows:
The integral that needs to be computed analytically reads:

$$\vec{I} = \int_{S'} \nabla' G(\vec{r}, \vec{r'}) \times \vec{J}(\vec{r'})\, dS' \quad (2.101)$$

Where the current in a rectangular basis function can be written (cf. Fig. 2.14):

$$\vec{J} = \frac{\hat{u}}{D} \big(\hat{u} \cdot (\vec{r'} - \vec{r'}_m)\big) \quad (2.102)$$

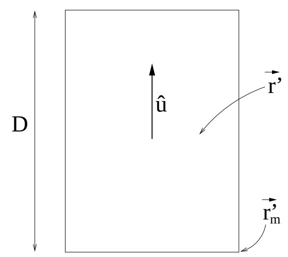

Figure 2.14: Definitions of the origin $\vec{r'}_m$ of the basis function, the unit vector $\vec{u}$ and the point $\vec{r'}$ where current is evaluated.

Eq. (2.101) can then be rewritten:

$$\begin{aligned}\vec{I} &= \int_{S'} \frac{-(1+jkR)e^{-jkR}}{R^3} \left(\vec{R}\times\hat{u}\right)\left(\hat{u}\cdot(\vec{r'}-\vec{r}_m)\right)\, dS' \\ &= \underbrace{\hat{u}\times\int_{S'} \frac{\vec{R}}{R^3}\left((1+jkR)e^{-jkR}-(1+\frac{k^2R^2}{2})\right)\left(\hat{u}\cdot(\vec{r'}-\vec{r'}_m)\right)\, dS'}_{I_{NS}\ :\ \text{Non Singular}} \\ &\quad \underbrace{+\,\hat{u}\times\int_{S'} \frac{\vec{R}}{R^3}(1+\frac{k^2R^2}{2})\left(\hat{u}\cdot(\vec{r'}-\vec{r'}_m)\right)\, dS'}_{I_S\ :\ \text{Singular}} \end{aligned} \tag{2.103}$$

The first integral I_{NS} in Eq. (2.103) is non singular and can be computed numerically. However, the second one, I_S, must be computed analytically.
The vector $\vec{r'}-\vec{r'}_m$ can be decomposed as follows:

$$\vec{r'}-\vec{r'}_m = (\vec{r'}-\vec{r}) + (\vec{r}-\vec{r'}_m)$$

Where $\vec{r}$ is the observation point.
Then, noticing that

$$\frac{\vec{R}}{R^3} = -\nabla'\frac{1}{R} \quad \text{and} \quad \frac{\vec{R}}{R} = \nabla' R$$

The singular integral I_S can be rewritten:

$$I_S = \hat{u} \times \Bigg[\underbrace{\int_{S'} \frac{\vec{R}}{R^3}\, dS'}_{\vec{I}_1} + \frac{k^2}{2} \underbrace{\int_{S'} \frac{\vec{R}}{R}\, dS'}_{\vec{I}_2} \Bigg] \big(\hat{u} \cdot (\vec{r} - \vec{r'}_m)\big)$$
$$+ \hat{u} \times \Bigg[- \underbrace{\int_{S'} \Big(\nabla' \frac{1}{R}\Big) \big(\hat{u} \cdot (\vec{r'} - \vec{r})\big)\, dS'}_{\vec{I}_a} + \frac{k^2}{2} \underbrace{\int_{S'} \big(\nabla' R\big) \big(\hat{u} \cdot (\vec{r'} - \vec{r})\big)\, dS'}_{\vec{I}_b} \qquad (2.104)$$

Let us define

$$\vec{z}_n = \big[(\vec{r} - \vec{r'}_m) \cdot \hat{n}_S\big]\hat{n}_S \qquad (2.105)$$

Where $\hat{n}_S$ is the unit normal to the plane of the half basis function. Hence, $\vec{z}_n$ is a vector normal to the plane of the half basis function and joining this plane to the observation point. Then, the vector $\vec{R}$ can be decomposed as follows:

$$\vec{R} = \vec{r'} - \vec{r} = \vec{\rho'} - \vec{\rho} - \vec{z}_n$$

And the integral $\vec{I}_1$ in (2.104) can be computed as:

$$\vec{I}_1 = \int_{S'} \frac{\vec{R}}{R^3}\, dS' = \int_{S'} \frac{\vec{\rho'} - \vec{\rho}}{R^3}\, dS' - \vec{z}_n \int_{S'} \frac{1}{R^3}\, dS' \qquad (2.106)$$

Where, as already mentioned above, the two integrals in the right member can be found in [34]. Similarly, $\vec{I}_2$ is computed as:

$$\vec{I}_2 = \int_{S'} \frac{\vec{R}}{R}\, dS' = \int_{S'} \frac{\vec{\rho'} - \vec{\rho}}{R}\, dS' - \vec{z}_n \int_{S'} \frac{1}{R}\, dS' \qquad (2.107)$$

And the two integrals in the right member can be found in [33]. Let us now concentrate on the two remaining integrals, $\vec{I}_a$ and $\vec{I}_b$. It can be shown (cf. internal note by C. Craeye) that:

$$\nabla' \frac{1}{R} = \nabla'_S \frac{1}{R} - \vec{z}_n \frac{1}{R^3}$$

and

$$\nabla' R = \nabla'_S R - \vec{z}_n \frac{1}{R}$$

Hence, $\vec{I}_a$ can be rewritten as follows:

$$\begin{aligned}\vec{I}_a &= \int_{S'} \big(\nabla'_S \frac{1}{R}\big)\big(\hat{u}\cdot(\vec{r'}-\vec{r})\big)\, dS' + \vec{z}_n \int_{S'} \frac{1}{R^3}\big(\hat{u}\cdot(\vec{r'}-\vec{r})\big)\, dS' \\ &= \int_{S'} \nabla'_S\left(\frac{\hat{u}\cdot(\vec{r'}-\vec{r})}{R}\right) dS' - \underbrace{\int_{S'} \frac{1}{R}\nabla'\big(\hat{u}\cdot(\vec{r'}-\vec{r})\big)\, dS'}_{\text{Will be zero after cross-product with } \hat{u}} \\ &+ \vec{z}_n\hat{u}\cdot\int_{S'} \frac{\vec{r'}-\vec{r}}{R^3}\, dS' \\ &= \sum_i \hat{n}_i\hat{u}\cdot \underbrace{\int_{\partial S'_i} \frac{\vec{R}}{R}\, dl}_{\vec{I}_3} + \vec{z}_n\hat{u}\cdot\vec{I}_1 \end{aligned} \tag{2.108}$$

Where the index i in the summation relates to the edges $\partial S'_i$ of the rectangular surface S' and $\hat{n}_i$ is the unit normal to this i^{th} edge, in the plane of the surface and pointing outward. In a similar way, it can be shown that:

$$\vec{I}_b = \sum_i \hat{n}_i\hat{u}\cdot \underbrace{\int_{\partial S'_i} R\vec{R}\, dl}_{\vec{I}_4} - \vec{z}_n\hat{u}\cdot\vec{I}_2 \tag{2.109}$$

It can then be shown (cf. internal note by C. Craeye) that these line integrals can be computed in the following way:

$$\vec{I}_3 = \hat{l}_i(R_i^+ - R_i^-) \tag{2.110}$$

$$\vec{I}_4 = \hat{l}_i\left(\frac{{R_i^+}^3 - {R_i^-}^3}{3}\right) \tag{2.111}$$

Where the $\hat{l}_i$, R_i^+ and R_i^- are defined in Fig. 2.15, from [33]. To summarize, the singular integral I_S can be computed as follows:

$$\begin{aligned} I_S &= \hat{u}\times\big(\vec{I}_1 + \frac{k^2}{2}\vec{I}_2\big)\big(\hat{u}\cdot(\vec{r}-\vec{r'}_m)\big) \\ &+ \hat{u}\times\big[-\vec{I'}_1 - \vec{z}_n(\hat{u}\cdot\vec{I}_1) + \frac{k^2}{6}\vec{I'}_2 - \frac{k^2}{2}\vec{z}_n(\hat{u}\cdot\vec{I}_2)\big] \end{aligned} \tag{2.112}$$

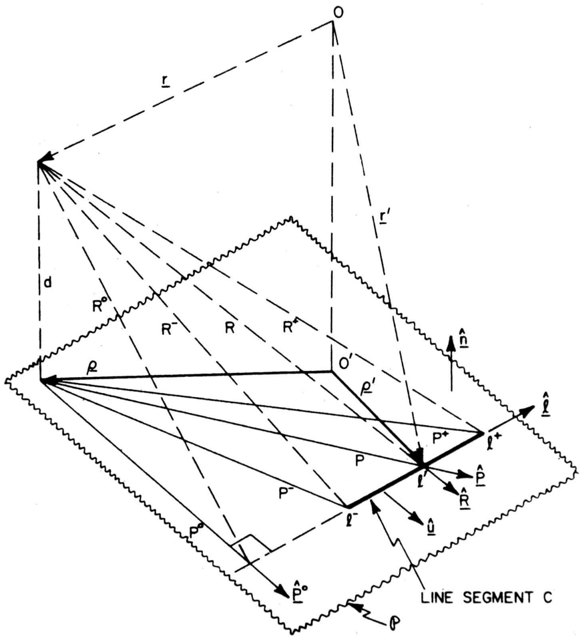

Figure 2.15: Geometrical quantities associated with an edge of the basis function lying in the plane $\mathcal{P}$. From [33]

Where $\vec{z}_n$ is defined in Eq. (2.105), $\vec{I}_1$ in Eq. (2.106), $\vec{I}_2$ in Eq. (2.107) and the two new quantities $\vec{I'}_1$ and $\vec{I'}_2$ are expressed as follows:

$$\vec{I'}_1 = \sum_i \hat{n}_i(\hat{u} \cdot \hat{l}_i)(R_i^+ - R_i^-) \tag{2.113}$$

$$\vec{I'}_2 = \sum_i \hat{n}_i(\hat{u} \cdot \hat{l}_i)(R_i^{+^3} - R_i^{-^3}) \tag{2.114}$$

2.3 Examples and validations

In this section, the accuracy of the simulation code is demonstrated on several examples.

2.3.1 Fractal antennas: The Sierpinski gasket

The Sierpinski gasket is named after the Polish mathematician Sierpinski who described some of the main properties of this fractal shape in 1916. The original gasket is constructed by subtracting a central inverted triangle from a main triangle shape. After the subtraction, three equal triangles remain on the structure, each one being half of the size of the original one. One can iterate the same subtraction procedure on the remaining triangles and if the iteration is carried out, an infinite number of times, the ideal fractal Sierpinski gasket is obtained. In such an ideal structure, each one of its three main parts is exactly equal to the whole object, but scaled by a factor of two and so are each of the three gaskets that compose any of those parts. Due to this particular similarity properties, shared with many other fractal shapes, it is said that the Sierpinski gasket is a self-similar structure. The mesh of a five-iteration gasket is presented in Fig. 2.16. If one admits that the current flowing from the feed should concentrate over a region that is comparable in size to the wavelength, and because of self-similarity, the frequency behavior should be similar at frequencies spaced by a factor equal to the ratio of the sizes of triangles in successive iterations (a factor of two in this case). Hence fractal antennas exhibit a multi-band behavior, as shown in Fig. 2.18. Simulation results obtained with our MoM code are in

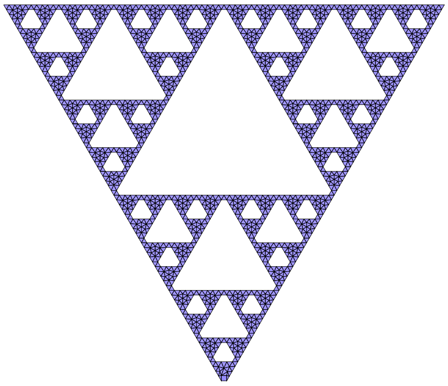

Figure 2.16: Mesh of the five-iteration Sierpinski monopole.

excellent agreement with experimental results found in [35] and shown in Fig. 2.17. Our results actually compare better with the experimental results than those obtained with the FDTD method, also presented in Fig. 2.17 from [35].

2.3.2 Input impedance of a slotted waveguide fed with a coaxial pin

Slotted waveguides have been studied here because, as it will be shown in Section 5.2, they can be used in the design of compact, high gain antennas using metamaterial superstrates. However, the full-wave simulation of large periodic structures excited by a slotted waveguide can be excessively time consuming because of the large number of unknowns involved. In order to speed up the design process, analytical models for the slotted waveguide can be very helpful. It is indeed possible to develop equivalent circuits based on the transmission line theory that account for the waveguide dimensions, size and position of the slots and of the feed probe. These equivalent circuits help in understanding the influence of the key parameters of the waveguide on the input impedance and allow a faster optimization of the latter than a method relying only on full-wave simulation.

The equivalent TL model for a waveguide with one transversal slot cut

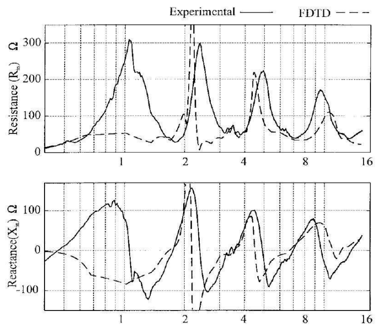

Figure 2.17: Input impedance of the five-iteration Sierpinski monopole (from [35]).

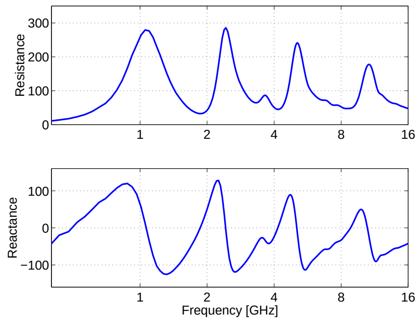

Figure 2.18: Input impedance of the five-iteration Sierpinski monopole obtained mith our MoM code.

in its top wall (Fig. 2.19) is represented in Fig. 2.22. In this model, each portion of the waveguide is modelled as a piece of transmission line and the transversal slots are represented by series resistance and reactance (longitudinal slots would be represented by shunt elements), whose expressions can be found in [37] and [38]. The feed probe is modeled by an ideal transformer and a series reactance [36]. If the end of the guide is open or closed, the equivalent transmission line is respectively open-circuited or short-circuited. However, both of these situations may involve strong reflections at the end of the guide and cause strong resonances that would dramatically reduce the achievable impedance bandwidth. Our goal was to test the optimization procedure for the input impedance, hence we chose to put a matched load at the end of the guide to avoid reflections. In full-wave simulations, the matched load was implemented as a hyperbolic resistive profile in the walls of the guide. The characteristic impedance of the equivalent transmission line is computed as follows.

Assuming that only the TE_{10} mode is propagating, fields in the waveg-

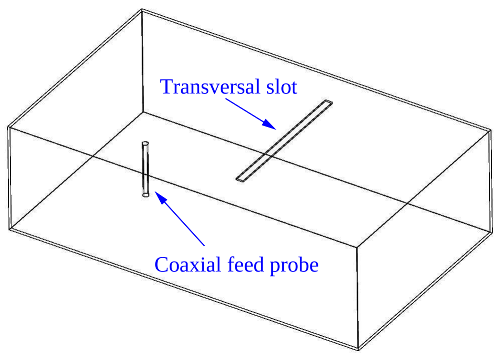

Figure 2.19: Waveguide with a transversal slot cut in its top wall.

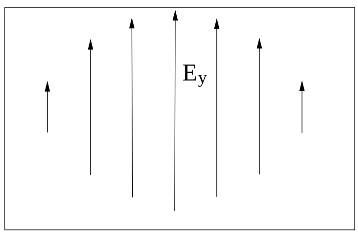

Figure 2.20: E Field in the waveguide cross-section.

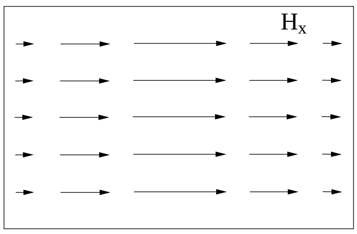

Figure 2.21: H Field in the waveguide cross-section.

uide cross-section are expressed as follows:

$$E_y(x) = E_0 sin(\frac{\pi x}{a}) \tag{2.115}$$

$$H_x(x) = -\frac{E_0}{Z_{TE}} sin(\frac{\pi x}{a}) \tag{2.116}$$

Where $Z_{TE} = \frac{\eta}{\sqrt{1-(\frac{\lambda}{2a})^2}}$ is the TE_{10} wave impedance and $\eta = \sqrt{\mu/\epsilon}$. The power flowing in the waveguide can be computed by integrating the Poynting vector over the whole cross-section.

$$\begin{aligned} P &= \int_{x=0}^{a} \int_{y=0}^{b} (\vec{E} \times \vec{H}^*) \cdot \hat{a}_z \, dx \, dy \\ &= b \int_{x=0}^{a} E_y(x) \, H_x^*(x) dx \\ &= \frac{|E_0|^2}{Z_{TE}} \frac{ab}{2} \end{aligned} \tag{2.117}$$

The voltage difference between bottom and top walls of the waveguide can be obtained by integrating the electric field along a vertical straight line joining these walls.

$$V = \int_{y=0}^{b} E(x = \frac{a}{2}) \, dy = E_0 \, b \tag{2.118}$$

The current flowing on top and bottom walls and crossing the waveguide cross-section is obtained by integrating the surface current density $\vec{K}$ along the bottom wall of the guide. This current density is given by $\vec{K} = \hat{n} \times \vec{H}$, where $\hat{n}$ is the unit normal to the waveguide bottom wall. Hence, this current is simply obtained as follows:

$$I = \hat{u}_z \cdot \int_{x=0}^{a} \hat{n} \times \vec{H}_x \, dx = \int_{x=0}^{a} H_x(x) \, dx = \frac{2aE_0}{\pi Z_{TE}} \tag{2.119}$$

Where $\hat{u}_z$ is the unit vector perpendicular to the waveguide cross-section. Three different equivalent models can be used. They differ by the parameters chosen to be equal in the transmission line model and the physical waveguide. They yield slightly different expressions for the characteristic impedance of the equivalent transmission line.

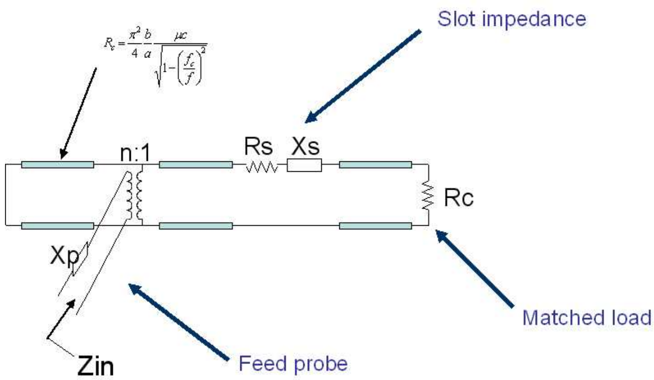

Figure 2.22: Equivalent TL model for the slotted waveguide (here for one slot).

Voltage and Current: $Z^{VI} = \frac{V}{I} = \frac{\pi}{2}\frac{b}{a}\frac{\eta}{\sqrt{1-\left(\frac{\lambda}{2a}\right)^2}}$

Power and Voltage: $Z^{PV} = \frac{V^2}{2P} = \frac{b}{a}\frac{\eta}{\sqrt{1-\left(\frac{\lambda}{2a}\right)^2}}$

Power and Current: $Z^{PI} = \frac{2P}{I^2} = \frac{\pi^2}{4}\frac{b}{a}\frac{\eta}{\sqrt{1-\left(\frac{\lambda}{2a}\right)^2}}$

Although the generally adopted empirical formula for the characteristic impedance is the geometric mean of the formulas given by the $V-I$ and $P-V$ models [39], after comparing these models with full-wave simulations on several examples, we noted that, in this case, the $P-I$ model, based on the equivalence of power and current flow was the most accurate and that is the one we used for the following simulations.
Simulation results are presented in Fig. 2.23 where the input impedance of a waveguide with 10 equidistant slots cut in its top wall is shown. The blue curves are obtained with the equivalent TL model and the red bullets are obtained from full-wave simulations. Striking is the very good agreement between these curves except above 2.8GHz. Actually, the waveguide cross-section was 12cm by 6cm, hence the cut-off frequency for the dominant TE_{10} mode is 1.25GHz. The next higher order mode is the TE_{20} with a cut-off at 2.5GHz, but this mode cannot be excited with a feed probe in the middle of the bottom wall. However, the TE_{11}

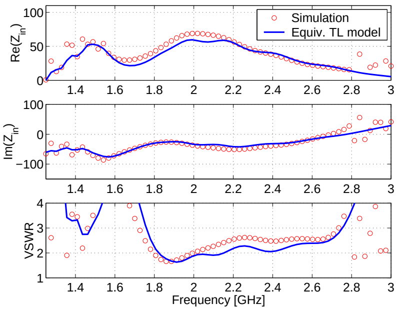

Figure 2.23: Input impedance and VSWR of the waveguide with ten equidistant slots. Simulation vs. Analytical model.

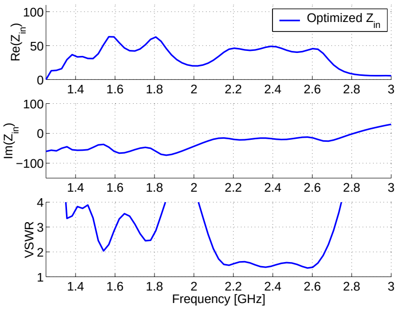

Figure 2.24: Input impedance and VSWR of the waveguide with optimized positions of the 10 slots.

mode can be excited and has a cut-off at 2.8GHz. Hence the analytical model is no longer valid from 2.8GHz because it was developed assuming only the propagation of the dominant mode and that is the reason for the difference between analytical and numerical results at high frequencies. Non-linear regression techniques were tested to optimize the input impedance around 2.4GHz by changing slot positions. The input impedance after optimization is shown in Fig. 2.24 where the VSWR is around 1.5 in a fractional bandwidth of more than 15 percent.

2.3.3 Near field computation: Fields in a waveguide supporting a TE_{10} mode.

It is possible to visualize fields in the structure that has been simulated. Indeed, once the equivalent currents have been computed, they can be integrated using (2.28), (2.29) and (2.15), (2.25) to compute electric and magnetic fields anywhere around the simulated structure. This is demonstrated here on a very simple example. We considered a slotted waveguide whose dimensions are as follows: width=1.5 cm, height=0.75 cm and length=2 cm. The transversal slot is cut in the middle of the top wall and the guide is excited with a small vertical probe located 0.5 cm from the back wall and supporting a delta-gap. From the size of the

waveguide, we can determine that the dominant mode (TE_{10}) cut-off frequency is $f_c^{10} = 10GHz$ and the next mode is the TE_{20} mode with a cut-off at $f_c^{20} = 20GHz$. Hence the waveguide was excited at a frequency of $f = 18GHz$ to allow only the dominant mode to propagate. Then, the currents obtained by simulation were integrated to compute E and H fields that are represented respectively in Figs. 2.25 and 2.26, where we recognize the typical field distributions for the TE_{10} mode.
It is interesting to notice how these fields can be obtained very easily with the MoM code. Indeed, as mentioned in Section 2.2.3, the testing procedure used to solve the EFIE with the method of moments reads:

$$\int_S \vec{E}_s(\vec{r}) \cdot \vec{J}_m \, dS = -\int_S \vec{E}_i(\vec{r}) \cdot \vec{J}_m \, dS$$

Where $\vec{E}_s(\vec{r})$ is the scattered electric field, $\vec{E}_i(\vec{r})$, the incident electric field, and $\vec{J}_m$ is the testing function. The scattered field is expressed as follows:

$$\begin{aligned} \vec{E}_s(\vec{r}) &= \frac{1}{j\omega\epsilon} \int_{S'} \left[k^2 \vec{J} G + \nabla\nabla \cdot (\vec{J} G) \right] \, dS' \\ &\approx \frac{1}{j\omega\epsilon} \sum_n \alpha_n \int_{S'} \left[k^2 \vec{J}_n G + \nabla\nabla \cdot (\vec{J}_n G) \right] \, dS' \end{aligned} \tag{2.120}$$

Where $\vec{J}_n$ are the basis functions used to discretize the current and α_n are the associated unknowns. Hence, the scattered electric field projected on a testing function can be written:

$$\begin{aligned} \int_S \vec{E}_s(\vec{r}) \cdot \vec{J}_m dS &= \sum_n \alpha_n \int_S \vec{J}_m \cdot \int_{S'} \left[k^2 \vec{J}_n G + \nabla\nabla \cdot (\vec{J}_n G) \right] \, dS' dS \\ &= \sum_n \alpha_n Z_{mn} \end{aligned} \tag{2.121}$$

Hence, the vector $[E_m]$ containing the values of the electric field projected on every the testing functions can be obtained as follows:

$$[E_m] = [Z_{mn}][\alpha_n] \tag{2.122}$$

Where $[Z_{mn}]$ is the impedance matrix and $[\alpha_n]$ the vector of unknowns. So, in order to compute the electric field in a plane such as in Fig. 2.25,

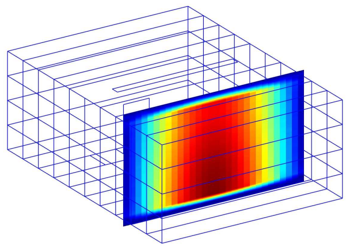

Figure 2.25: E field in the slotted waveguide.

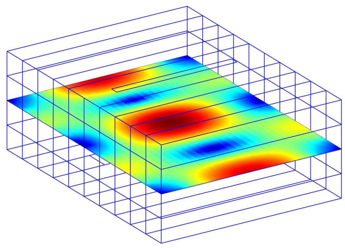

Figure 2.26: H field in the slotted waveguide.

one just needs to discretize this observation plane in small rectangular domains, over which the fields are assumed to be constant, and testing functions are defined on these small domains. Then, an impedance matrix is filled using the basis functions of the original structure (i.e. the waveguide in this case) and the newly defined testing functions. This impedance matrix is then multiplied by the vector of unknows computed previously when simulating the original structure and the result is a vector containing values of the average projected electric field at the place of the testing functions multiplied by the surface of these functions. A similar procedure can be used to compute the magnetic field.

2.4 Conclusion

In this chapter, general relations between fields and sources were recalled and the basic features of the MoM code were presented:

- Based on the surface field equivalence principle.
- Method of Moments used to solve integral equations formulations.
- EFIE formulation for metallic structures.
- PMCHWT formulation for dielectric structures.

- Separate treatment of the $1/R$ and $1/R^3$ singularities involved respectively in the Green's function and its gradient.

Finally, some validating examples were presented.

Infinitely periodic structures

3

Solving problems that involve large periodic structures such as metamaterials or large antenna arrays can be excessively time-consuming because of the number of unknowns included in such structures. A convenient approach for solving such problems is the infinite-array approximation. It provides good estimates of the behavior of the fields radiated by very large arrays and it is a good starting point for more accurate techniques involving the estimation of the truncation effets.
In infinite arrays, the periodicity is accounted for by replacing the single dipole Green's function by the Green's function related to an infinite array of electric dipoles with constant amplitudes and linear phase progressions.

3.1 Computation of the periodic Green's function

Let us consider an infinite array of point current sources, located at $\vec{r}_m = (ma, nb, 0)$, phase shifts between successive sources of ψ_x in the x direction and ψ_y in the y direction and an observation point $\vec{r} = (x, y, z)$. The Green's function for this array is the solution of the following Helmoltz equation:

$$(\nabla^2 + k^2)G = -\sum_{m=-\infty}^{\infty}\sum_{n=-\infty}^{\infty} \delta(x - ma)\delta(y - nb)\delta(z)e^{-jm\psi_x}e^{-jn\psi_y} \quad (3.1)$$

Three different formulations will be used, depending on the location of the observation point.

3.1.1 First formulation : direct summation

Solving directly Eq. 3.1 yields the spatial formulation of the Green's function:

$$G(x,y,z) = \sum_{m=-\infty}^{\infty} e^{-jm\psi_x} \sum_{n=-\infty}^{\infty} e^{-jn\psi_y} \frac{e^{-jkr_{mn}}}{4\pi r_{mn}} \tag{3.2}$$

where

$$r_{mn} = \sqrt{(x-ma)^2 + (y-nb)^2 + z^2}$$

and

$$\psi_x = k_x a \qquad \psi_y = k_y b$$

This spatial summation converges very slowly for most observation positions. However, as shown in [31] a spectral formulation can be used where the Green's function is expressed as a sum of plane waves. This is the second formulation.

3.1.2 Second formulation : Sum of plane waves

It can be shown [31] that when written as a Fourier series, the periodic excitation in Eq. (3.1) can be expressed as:

$$\sum_{m=-\infty}^{\infty} \sum_{n=-\infty}^{\infty} \delta(x-ma)\delta(y-nb)\delta(z)e^{-jm\psi_x}e^{-jn\psi_y} =$$
$$\frac{1}{ab} \sum_{m=-\infty}^{\infty} \sum_{n=-\infty}^{\infty} e^{j\beta_m x}e^{j\beta_n y}\delta(z)$$

with

$$\beta_m = \frac{2\pi m}{a} - k_x \qquad \beta_n = \frac{2\pi n}{b} - k_y$$

And the spectral domain Green's function, expressed as a sum of plane waves, reads:

$$G(x,y,z) = \frac{1}{2jab} \sum_{m=-\infty}^{\infty} \sum_{n=-\infty}^{\infty} \frac{e^{-j\gamma_{mn}|z|}e^{j(\beta_m x + \beta_n y)}}{\gamma_{mn}} \tag{3.3}$$

where

$$\gamma_{mn} = \begin{cases} \sqrt{k^2 - \beta_m^2 - \beta_n^2} & if \;\; k^2 > \beta_m^2 + \beta_n^2 \\ -j\sqrt{\beta_m^2 + \beta_n^2 - k^2} & if \;\; k^2 < \beta_m^2 + \beta_n^2 \end{cases}$$

This spectral formulation converges rapidly as long as $z \neq 0$ (the "off-plane" case). This rapid convergence occurs because as m ans n increase, the plane-wave response changes from propagating waves to exponentially decaying evanescent waves. When $z = 0$ (the "on-plane" case), the convergence is slower because it doesn't benefit from this exponential decay. To overcome this problem, a third formulation will be used where the Green's function is expressed as a sum of cylindrical waves.

3.1.3 Third formulation : Sum of cylindrical waves

Let us first consider a linear infinite array of point sources located at $(ma, 0, 0)$ with a phase shift ψ_x between successive sources. The spatial Green's function for this array is expressed as follows:

$$G(x, y, z) = \sum_{m=-\infty}^{\infty} e^{-jm\psi_x} \frac{e^{-jkr_{mn}}}{4\pi r_{mn}} \tag{3.4}$$

where

$$r_{mn} = \sqrt{(x - ma)^2 + y^2 + z^2}$$

As already mentioned, this sum is slowly convergent. But via the Poisson sum formula, it can be transformed into [40]:

$$G(\vec{r}) = G(R, x) = \frac{1}{4ja} \sum_{n=-\infty}^{\infty} e^{jk_n x} H_0^{(2)}(\gamma_n R) \tag{3.5}$$

with

$$\begin{aligned} R &= \sqrt{(y^2 + z^2)} \\ \gamma_n &= \begin{cases} \sqrt{k^2 - k_n^2} & if \;\; k^2 > k_n^2 \\ -j\sqrt{k_n^2 - k^2} & if \;\; k_n^2 > k^2 \end{cases} \end{aligned} \tag{3.6}$$

where

$$k_n = \frac{\psi_x}{a} + n\frac{2\pi}{a}$$

and $H_0^{(2)}$ is the Hankel function of the second kind and order zero. For indices n leading to real values of γ_n, the cylindrical waves are propagating and for imaginary values of γ_n, the Hankel function becomes a rapidly decaying modified Bessel function of the first kind, which represent evanescent cylindrical waves:

$$\begin{aligned} H_0^{(2)}(x) &= J_0(x) - jY_0(x) \\ H_0^{(2)}(-jx) &= \frac{2}{\pi} jK_0(x) \end{aligned}$$

For observation points located far from the X axis, very few evanescent waves need to be taken into account and the summation converges rapidly. For observation points close to the X axis, the convergence is slower and the direct summation (3.4) will be used.
The doubly periodic array of point sources can be seen as the superposition of an infinite number of infinite linear arrays along X. The associated Green's function can then also be seen as the superposition of Green's functions associated to infinite lines along X, with a phase shift ψ_y between successive lines. The expression for the doubly periodic Green's function then becomes :

$$G(x, y, z) = \frac{1}{4ja} \sum_{p=-\infty}^{\infty} e^{-jp\psi_y} \sum_{n=-\infty}^{\infty} e^{-jk_n x} H_0^{(2)}(\gamma_n R_p) \tag{3.7}$$

where

$$\begin{aligned} R_p &= \sqrt{(y - pb)^2 + z^2} \\ k_n &= \frac{\psi_x}{a} + n\frac{2\pi}{a} \\ \gamma_n &= \begin{cases} \sqrt{k^2 - k_n^2} & if \;\; k^2 > k_n^2 \\ -j\sqrt{k_n^2 - k^2} & if \;\; k^2 < k_n^2 \end{cases} \end{aligned}$$

3.1.4 Tabulation of the periodic Green's function

In the previous sections, we showed that, depending on where the periodic Green's function needs to be evaluated, the adequate formulation is chosen to ensure the fastest possible convergence. Moreover, convergence

may still be accelerated using techniques such as Shank's [41] or Levin's [42] extrapolation formula . Although efficient techniques are used, in a MoM scheme, the computation time of the periodic Green's function may still be considered as prohibitive, especially for small distances above the array plane. To overcome this problem, the Green's function is tabulated in a 2D or 3D table (depending on the structure to be simulated). The singularity is extracted before tabulation, hence the function obtained is smooth and can be stored accurately in a table of limited size. When the Green's function needs to be evaluated (when filling the impedance matrix), a second order interpolation technique is used on the values stored in the table. Then, the singular component is either added back after interpolation or integrated separately as explained in Section 2.2.5.
We would like to stress that, thanks to our efficient computation scheme for the periodic Green's function, the singularity can be extracted very easily. Actually, only the first singularity (the one at the origin) has to be extracted. This allows to perform exactly the same treatment of this singularity in the case of isolated objects or in periodic arrays. In periodic structures, when the observation point lies too close to the next singularity, the testing functions are shifted of one unit cell, and the result of the integration is multiplied by the adequate phase factor.

3.2 Gradient of the doubly periodic Green's function

As shown is Section 2.2.4, when simulating dielectric objects, the gradient of the periodic Green's function appears in the integral equations of the PMCHWT formulation: Eqs (2.88) and (2.89). The three formulations used for the computation of this gradient are derived in this section.

3.2.1 First formulation : direct summation

By derivation of Eq.(3.2) :

$$\vec{\nabla} G(x,y,z) = -\sum_{m=-\infty}^{\infty} e^{-jm\psi_x} \sum_{n=-\infty}^{\infty} e^{-jn\psi_y} \frac{(1+jkr_{mn})e^{-jkr_{mn}}}{4\pi r_{mn}^3} \vec{r}_{mn} \tag{3.8}$$

3.2.2 Second formulation : Sum of plane waves

By derivation of Eq.(3.3) :

$$\frac{\partial G}{\partial x} = \frac{1}{2ab} \sum_{m=-\infty}^{\infty} \sum_{n=-\infty}^{\infty} \beta_m \frac{e^{-j\gamma_{mn}|z|} e^{j(\beta_m x + \beta_n y)}}{\gamma_{mn}} \tag{3.9}$$

$$\frac{\partial G}{\partial y} = \frac{1}{2ab} \sum_{m=-\infty}^{\infty} \sum_{n=-\infty}^{\infty} \beta_n \frac{e^{-j\gamma_{mn}|z|} e^{j(\beta_m x + \beta_n y)}}{\gamma_{mn}} \tag{3.10}$$

$$\frac{\partial G}{\partial z} = \frac{-1}{2ab} \sum_{m=-\infty}^{\infty} \sum_{n=-\infty}^{\infty} e^{-j\gamma_{mn}|z|} e^{j(\beta_m x + \beta_n y)} \tag{3.11}$$

Note that Eq. (3.11) is only valid for positive values of z. If this component of the gradient needs to be computed for $z < 0$, the sign has to be changed.

3.2.3 Third formulation : Sum of cylindrical waves

By derivation of Eq.(3.7) :

$$\frac{\partial G}{\partial x} = \frac{1}{4ja} \sum_{p=-\infty}^{\infty} e^{-jp\psi_y} \sum_{n=-\infty}^{\infty} -jk_n e^{-jk_n x} H_0^{(2)}(\gamma_n R_p) \tag{3.12}$$

$$\frac{\partial G}{\partial y} = \frac{1}{4ja} \sum_{p=-\infty}^{\infty} e^{-jp\psi_y} \sum_{n=-\infty}^{\infty} \frac{y - pb}{R_p} \gamma_n e^{-jk_n x} H_0^{(2)'}(\gamma_n R_p) \tag{3.13}$$

$$\frac{\partial G}{\partial z} = \frac{1}{4ja} \sum_{p=-\infty}^{\infty} e^{-jp\psi_y} \sum_{n=-\infty}^{\infty} \frac{z}{R_p} \gamma_n e^{-jk_n x} H_0^{(2)'}(\gamma_n R_p) \tag{3.14}$$

Where the derivative of Hankel function of the second kind and order zero is:

$$\begin{aligned} H_0^{(2)'}(x) &= -J_1(x) + jY_1(x) \\ H_0^{(2)'}(-jx) &= -\frac{2}{\pi} K_1(x) \end{aligned}$$

3.3 Validation in the case of a self-complementary array

As shown by Mushiake [26], self-complementary antennas exhibit a constant impedance equal to $\eta/2$, where η is the free-space impedance. Of

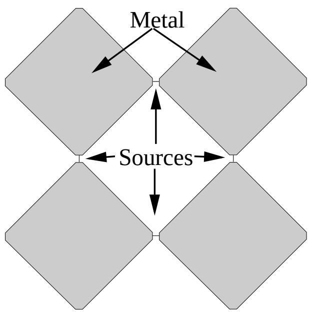

Figure 3.1: Planar bicone array.

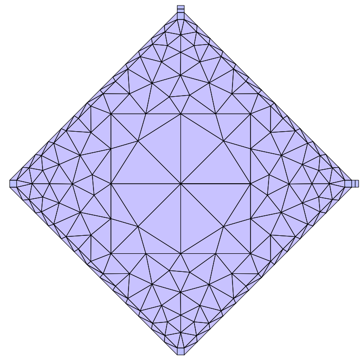
Figure 3.2: Mesh of the unit cell for the planar bicone array.

course, to be exactly self- complementary, the antennas should be infinite. In fact, there exists a relationship between the volume occupied by an antenna and its lowest achievable Q [27]. As for large arrays, the largest dimension of the whole structure may, in principle, be sufficient to achieve a large bandwidth. An elegant solution, proposed by McGrath and Baum [43], consists in ensuring that the array itself, rather than the array elements, has a self-complementary structure. This is, for instance, the case for arrays made of square plates connected at the corners, where they are also fed ("planar bicone" array). This array is depicted in Fig. 3.1 and the mesh of its unit-cell in Fig. 3.2. In order to get a good accuracy in the representation of currents, it is always a good idea to use a finer mesh where the current is stronger. In this case, the mesh is finer along the edges of the metallic plate and a typical current distribution at 1GHz is shown in Fig. 3.3. One can note that the current is indeed stronger along the edges of the plate.

Such arrays are compact and naturally exhibit a very wide bandwidth. However, these structures radiate on both sides of the plane, which makes them practically useless for most applications. The simplest structure to avoid radiation on the backside probably consists in placing a ground plane. It has been shown in the literature that the presence of a ground plane may have a dramatic effect on the bandwidth of isolated elements.

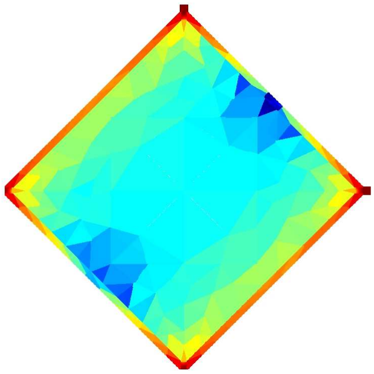

Figure 3.3: Current distribution in the unit cell of the planar bicone array at 1GHz.

Based on this, it may be expected that a ground plane may destroy the wideband behavior of self-complementary arrays. Infinite array simulations carried out with the MoM code showed that the input impedance of the array element is indeed constant and extremely close to $\eta/2$, as shown by the blue curve in Fig. 3.4. Simulations including a ground plane below the array also showed that the bandwidth is dramatically reduced because of destructive interferences of the fields radiated by the array itself and its image in the ground plane when their distance is a multiple of the wavelength. The red curve in Fig. 3.4 shows indeed that the radiation resistance drops to zero when the distance separating the array plane from the ground plane is a multiple of half a wavelength.

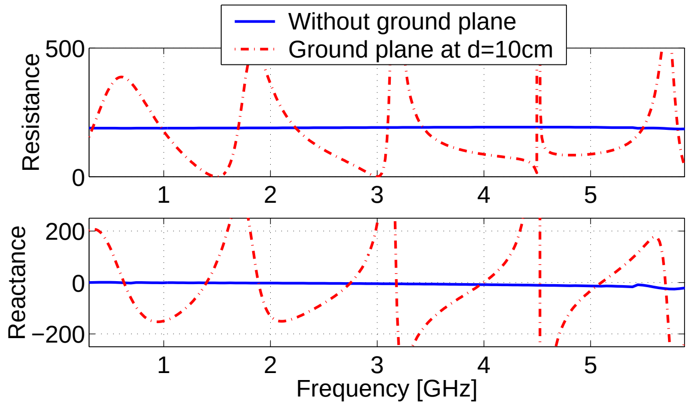

Figure 3.4: Impedance of self-complementary array without ground plane and with ground plane at d=10 cm below the array.

3.4 Transmission/Reflection properties of infinitely periodic structures

3.4.1 Metallic EBG structures

Electromagnetic Band Gap (EBG) structures are periodic structures, which exhibit passbands and stopbands to electromagnetic waves in some directions. The applications of such structures are numerous and, among them, one can find the enhancement of antenna gain, sidelobe level reduction and reduction of mutual coupling between antennas by suppressing surface-wave effects. One of the simplest EBG structures is made of parallel conducting wires arranged in a 2D square lattice. This structure is studied in [75] and in [74] where it is used to increase the gain of a monopole antenna. In this section, we will focus on the transmission properties of this structure illuminated by a plane wave. For the sake of simplicity, the parallel conducting wires are replaced by thin metallic strips, as described in Fig. 3.5. Infinite array simulations can be carried out with our MoM code to efficiently analyze the transmission properties of such a structure. Results for the transmission and reflection coefficients through 6 an 12 layers are presented respectively in Figs. 3.6 and 3.7. In this case, the unit cell is made of very small pieces of metallic

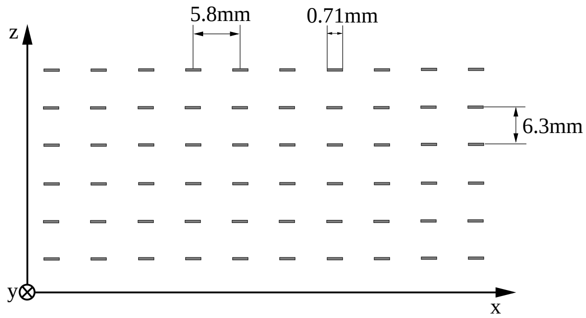

Figure 3.5: Description of the EBG structure. The incident plane wave propagates along the z axis.

strips (one for each layer), each of which contains only a few unknowns (typically 2 or 3) and hence the computation of the transmission characteristics can be performed very rapidly. The results of these simulations are presented in Figs. 3.6 and 3.7 where the transmission and reflection coefficients respectively through 6 and 12 layers are presented, as well as the sum of their amplitudes. One can see the typical low frequency cut-off of metallic periodic structures (here around 13 GHz). This cut-off frequency is due to the fact that when the wavelength is much greater than the period of a metallic grid, the latter behaves as a plain metallic sheet. Then, a first bandgap is visible around 27 GHz and a second one around 48 GHz. As expected, the depth of these bandgaps increases with the number of layers. Also, one can notice that the number of transmission peaks in the first passband is also directly related to the number of layers. Indeed, in an EBG structure composed of N layers, there are (N-1) Fabry-Perrot cavities and then (N-1) resonance frequencies associated [44]. Therefore, at normal incidence, the number of propagation peaks N_{peaks} is associated to the number of layers N_{layers} by the following relationship:

$$N_{peaks} = N_{layers} - 1$$

The consistency of the computation technique is assessed by verifying that the sum of the transmission and reflection coefficients is constant at 0 dB within a few tenths of a dB.

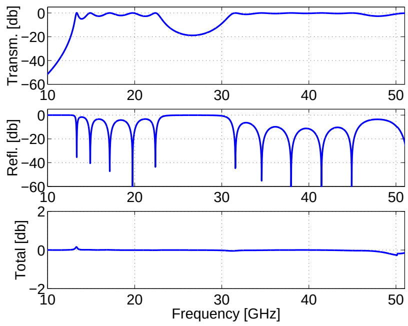

Figure 3.6: Transmission of a plane wave trough the structure shown in Fig. 3.5 with 6 layers at normal incidence.

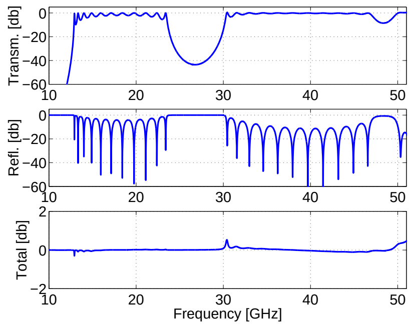

Figure 3.7: Transmission of a plane wave trough the structure shown in Fig. 3.5 with 12 layers at normal incidence.

We also verified the equivalence between metallic strips and wires with a circular cross-section, when the width of the strips is equal to four times the wire radius: $w = 4r$. This is illustrated in Fig. 3.8 where the transmission characteristics were computed in both cases. The band-gap is exacltly at the same position and there is only a slight increase of the cut-off frequency when simulating wires.

3.4.2 Perfect magnetic conductors

A straightforward method to enhance the directivity of antennas and prevent back radiation is to use a metallic reflector (as in Section 3.3. If the reflector behaves as a perfect electric conductor (PEC), a horizontal antenna must be placed at a distance $d = \frac{2n+1}{2} \cdot \frac{\lambda}{2}$, with $n = 0, 1, 2, \cdots$, from the reflector to interfere constructively with its image in the reflector. This is due to the 180° reflection phase of a PEC reflector. Indeed, boundary conditions along a PEC object (Eq. (2.52)) force the total tangential electric field to vanish along the interface, hence the reflected field must be in phase opposition with respect to the incident field at the interface. The duality theorem for Maxwell's equations says that if a PEC is substituted by a PMC (Perfect Magnetic Conductor), the boundary conditions change in a corresponding manner. Hence, using

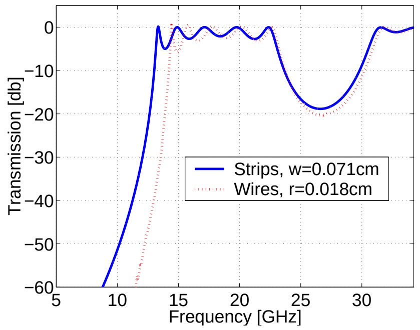

Figure 3.8: Comparison of the transmission characteristics through 6 layers made of wires with circular cross-section and thin strips. All other parameters are the same as in Fig. 3.5.

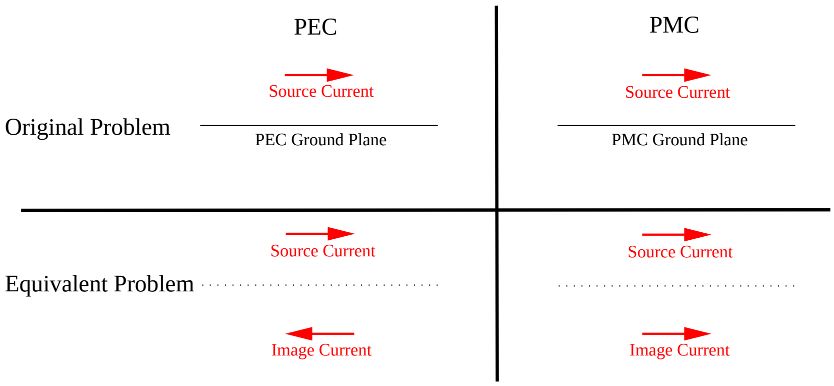

Figure 3.9: Illustration of the image theory applied to PEC and PMC ground planes.

image theory, the image currents of a PEC are in opposite phase to the original ones, while those of a PMC are in-phase. this is illustrated in Fig. 3.9. Also, a normally incident wave reflected by a PEC experiences a phase shift of 180°; in contrast, a PMC causes no phase shift. Thus, for constructive interference the PMC has to be placed at a distance $d = n \cdot \frac{\lambda}{2}$ from the antenna. In order to save space in antenna design, the reflector should be put as close as possible to the antenna. However, with a PEC reflector, very short distances are not possible because the antenna would be almost short-circuited by its image. This problem doesn't occur when using PMC reflectors and the antenna can then be placed very close to the reflector. Actually, no PMC material has been discoverd yet, but periodic structures that shows the same characteristics in a limited frequency band can be used as artificial PMCs [45]. An example of such a structure is the mushroom-like EBG [15] structure depicted in Fig. 3.10 that consists of an array of square metallic patches connected to a PEC ground plane with vias. The unit cell of this periodic structure, used for infinite-array simulations is shown in Fig. 3.11. The result of these simulations for the phase of the reflection coefficient are presented in Fig. 3.12 and are in very good agreement with those presented in [45] and obtained with FDTD simulations. It is obvious that around $27GHz$, the reflection phase is close to 0° and that in a small frequency band, this periodic EBG structure behaves like a PMC.

3.4.3 Field canalization: Sub-wavelength imaging

Recently, important efforts have been produced towards the development of lenses that are not limited by diffraction and able to reproduce images with sub-wavelength resolution. A first approach was proposed by Pendry [46] and uses a slab of left-handed medium (LHM) with $\epsilon = \mu = -1$. Another approach suggested by Wiltshire and Pendry [47] uses arrays of magnetic wires called Swiss Rolls. Both of these designs only work at resonance and hence, are narrow band and very sensitive to losses. Recently, P. Belov et al. proposed [48],[49] to use wire media (WM), i.e. an array of parallel conducting wires (Fig. 3.13) that will

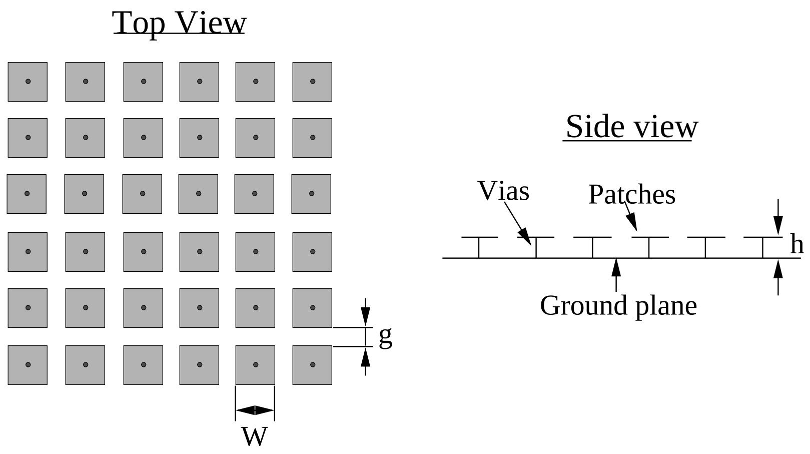

Figure 3.10: Geometry of the mushroom-like PMC.

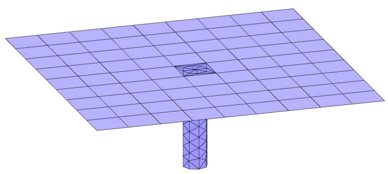

Figure 3.11: Unit cell for the PMC surface depicted in Fig. 3.10.

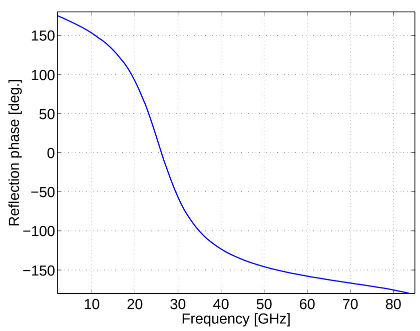

Figure 3.12: Phase of the reflection coefficient for the PMC surface depicted in Fig. 3.10 with $W = 0.3$ cm, $g = 0.05$ cm, $h = 0.1$ cm and $r = 0.0125$ cm.

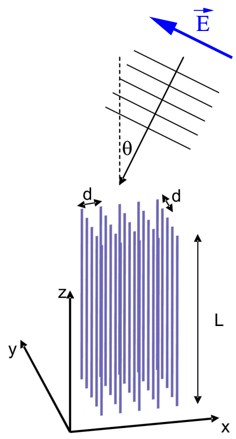

Figure 3.13: Wire medium.

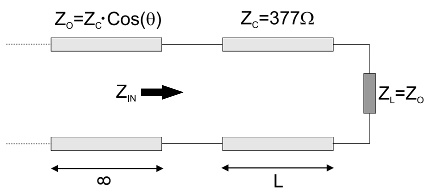

Figure 3.14: Transmission line model for the propagating waves in the wire medium.

operate as a multi-conductor transmission line and canalize the source electric field to produce images with sub-wavelength resolution far away from that source. As it was demonstrated in [48], this wire medium provides total transmission for any incidence angle, if Fabry-Perot conditions are satisfied. In this section, we study how parameters of WM influence on the transmisson for different incidence angles and, hence, on the resolution of the WM slab.

Analytical model

The structure under study is depicted in Figure 3.13 and consists of a periodic array of thin metallic strips with a square lattice. The length of the strips and the spacing between them are respectively represented by L and d. In a first instance, the transmission properties of a plane wave are studied. The incidence angle with respect to the wire axis is θ and the E-field polarization is parallel to the plane of the strips (TM waves). Assuming that the wire medium behaves like a transmission line, a very simple analytical model, presented in Figure 3.14 can be used. Only TEM modes can propagate between the wires at low frequencies, and at the interface of the structure, the longitudinal component of the electric field of TM waves will vanish. Only the component tangential to the interface propagates. Establishing an equivalent transmission line model limited to the tangential component of E and H fields, we get a characteristic impedance of $Z_o = \eta \cdot \cos(\theta)$ in free space. Where $\eta = 377\Omega$ is the free-space impedance. The medium outside the structure is just free-space with a wave impedance which is $Z_c = \eta$. With this simple model, it is trivial to show that the input impedance of the equivalent transmission line can be written as:

$$Z_{in} = Z_c \frac{Z_o + jZ_c \tan(kL)}{Z_c + jZ_o \tan(kL)} \quad \text{with } k = \frac{2\pi}{\lambda} \tag{3.15}$$

And the input reflection coefficient follows :

$$\Gamma = \frac{Z_{in} - Z_o}{Z_{in} + Z_o} \tag{3.16}$$

The magnitude of this reflection coefficient is depicted in Figure 3.15 for several incidence angles. One can notice that, according to this simple model, the fields are fully transmitted each time the length of the wires is a multiple of the half-wavelength. Also, reflections are stronger for greater incidence angles. As the incidence angle increases, interactions between electric field and wires are stronger and induce greater reflections. At normal incidence, the fields do not interact at all with the wires and the structure is fully transparent.

Numerical analysis

In order to check the consistency of the simple model described above, this structure has been investigated numerically with our MoM simulation code. The structure is supposed to be infinitely periodic. With this assumption, and by resorting to doubly infinite Green's function, the unknowns of the problem reduce to a single unit cell and very fast simulations can be carried out. Figure 3.16 presents the reflection coefficient of a plane wave for several incidence angles. By comparing these curves with analytical results in Figure 3.15, one can notice that the analytical model perfectly predicts the dependance of the maximum magnitude of

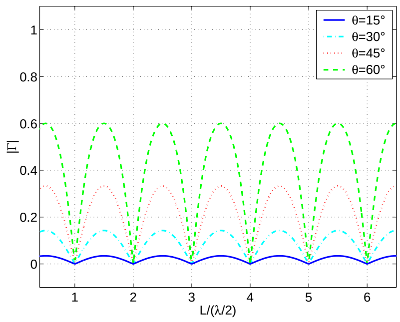

Figure 3.15: Magnitude of the reflection coefficient computed with Eq. 3.16

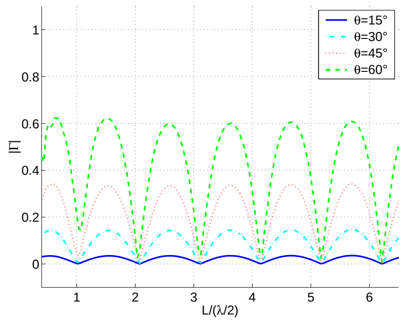

Figure 3.16: Simulated reflection coefficient for several incidence angles, $d = 0.0625$cm.

the reflection coefficient with respect to incidence angle. However, it is also obvious that reflection nulls are shifted towards lower wavelengths. And as shown in Figure 3.17, the lower the wire density, the greater the shift. This may be explained by considering evanescent waves appearing on each side of the wire medium which penetrate further in the material when the λ/d ratio, i.e. the wire density, is lower. Because of these edge effects, the effective length of the wires is decreasing with decreasing density. This is illustrated in Figure 3.18, where the difference $real\ length - effective\ length$ is shown for several values of wire density and incidence angle. In each case, the effective length of wires is obtained by matching the analytical model and the simulation results using non-linear regression techniques on the wire length. This picture clearly shows that only in very dense arrays the effective length is close to the real physical length.

Analytical model for wire length reduction

According to the transmission line model, at resonance (i.e. when there is no reflection), the currents at the ends of the wire medium should be non zero (local maximum), which is physically not possible for finite wires. Our interpretation is that those currents are annihilated by the currents associated with the evanescent waves appearing at the transition

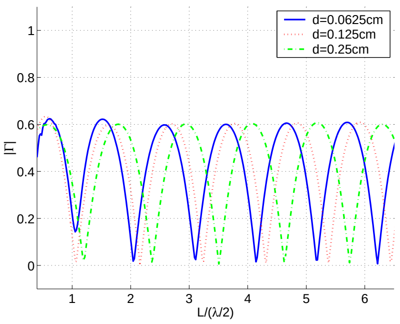

Figure 3.17: Reflection coefficient for several densities of wires, $\theta = 60$.

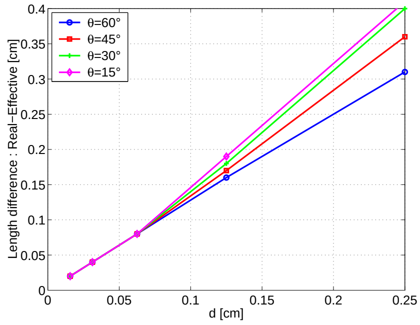

Figure 3.18: Length reduction of wires vs. wire density and incidence angle.

between free space and wire medium. Extra length may be necessary for this annihilation to occur. It is expected that this extra length is of the order of the decay distance of the evanescent wave. The latter can be computed as follows:
The wavenumber k_z of these evanescent waves along z must fulfill [50]:

$$k_z^2 = k_0^2 - k_x^2 - k_y^2 - k_p^2 \tag{3.17}$$

where k_0 is the free-space wavenumber and k_p is the plasma wavenumber of the wire medium, which can be approximated by [50]:

$$k_p^2 = \frac{2\pi}{d^2(\ln\left(\frac{d}{2a}\right) + 0.535)} \tag{3.18}$$

where a is the width of the strips and d is the distance between strips. As the plane wave propagation is in the XZ plane, $k_x = k_0 sin(\theta)$ and $k_y = 0$. Finally, we get the attenuation coefficient α :

$$k_z = \sqrt{k_0^2 \cos^2\theta - k_p^2} = j\alpha \tag{3.19}$$

Assuming that these evanescent waves have a significant effect along a distance $1/\alpha$ at each ends, the difference between real and effective length of wires should be of the order of $2/\alpha$ and is plotted in Fig. 3.19. Striking is the quite good agreement between these curves and those obtained

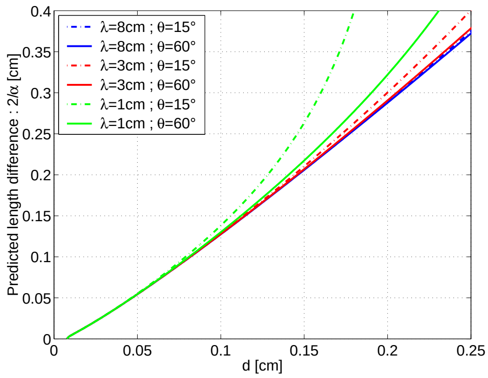

Figure 3.19: Predicted length difference computed as $2/\alpha$.

numerically in Fig. 3.18, especially for $\theta = 15°$. However, according to the analytical model, the effect of incidence angle on length reduction is negligible as long as the wavelength is much greater than the lattice period. This effect seems to be stronger in Fig. 3.18, but one should note that values of length reduction obtained for $d = 0.25$cm are not very accurate, due to the very small frequency domain over which simulation results could be compared to the analytical model. Indeed, to obtain full transmission, the wire length has to be a multiple of half a wavelength; moreover, to effectively canalize the fields, the distance between wires must be small compared to the wavelength. This is expressed by the following condition:

$$d \ll \lambda < 2L$$

And this condition can only be fulfilled over a small frequency range if the density of wires is too small.

Practical example of canalization

The last step of this study is to assess the canalization performance on a practical example. In this case, the structure was made of 23×23 strips of length $L = 15$ cm and spaced by $d = 0.2$ cm. The wires are illuminated by a loop of magnetic current at a frequency $f = 1$ GHz placed 0.1 cm below them. Figure 3.20 shows the structure as well as

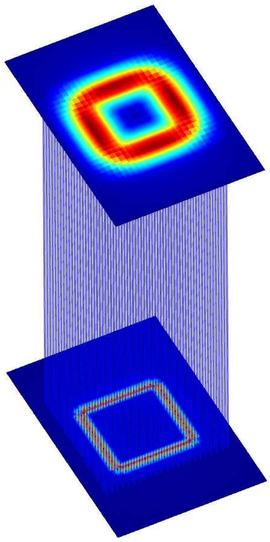

Figure 3.20: Canalization of electric field by wires

the source and image electric fields. Knowing that the size of these images is 0.26λ by 0.18λ, it is clear that the image of the electric field has been propagated from one side of the structure to the other one with a resolution much finer than the wavelength. As stated in [48], the image resolution is only limited by the density of the wires and is about twice the lattice period. Hence, in our example, the resolution would be about 0.4 cm$= \lambda/75$. It is worth noticing that these simulations can be carried out very efficiently by resorting to infinite array simulations, combined with the Array Scanning Method as described in [51].

3.5 Losses

When the conductors considered in simulations exhibit a finite conductivity, ohmic losses occur and can lead to some deviations of the input impedance when compared to antennas made of PEC materials. In this section, we show how it is possible to account for Ohmic losses in metallic structures, and the chosen approach is validated by verifying energy conservation in the case of an infinite array of TEM horns.

3.5.1 Impedance matrix elements

In order to take these losses into account, we developed a simple model based on the surface impedance of the conductors. From Snell's law of refraction, if an electromagnetic wave propagates from a low (or zero) conductivity medium to a high conductivity medium, the transmitted wave will be refracted very close the the normal at the interface, almost independently of the angle of incidence. Because of the finite conductivity of the medium, the refracted wave will be exponentially decaying, as energy is dissipated in ohmic losses. Suppose that the conducting region is so large that the evanescent wave attenuates completely. Then, the refracted electric field can be described as a damped plane wave propagating into the depth of the conductor. Because fields are continuous along the interface between both regions, the intrinsic impedance of the wave remains the same at the interface and the surface impedance can be computed as follows:

$$Z_s = \frac{E}{H} = \sqrt{\frac{j\omega\mu}{\sigma + j\omega\epsilon}} \tag{3.20}$$

Where μ and ϵ and σ are respectively the magnetic permeability, the electric permittivity and the conductivity of the metal. Assuming a good conductor ($\sigma \gg \omega\epsilon$), expression (3.20) simplifies to:

$$\begin{aligned} Z_s &= \frac{1+j}{2}\omega\mu\delta & (3.21) \\ &= (1+j)\sqrt{\frac{\omega\mu}{2\sigma}} & (3.22) \end{aligned}$$

Where $\delta = \sqrt{\frac{2}{\sigma\omega\mu}}$ is the skin depth. The presence of losses brings a new boundary condition along the metallic surface. Instead of Eq. (2.52), enforcing zero tangential electric field, one now has to use:

$$\hat{n} \times \vec{E}(\vec{r}) = Z_m\big(\hat{n} \times \vec{H}(\vec{r})\big) \tag{3.23}$$

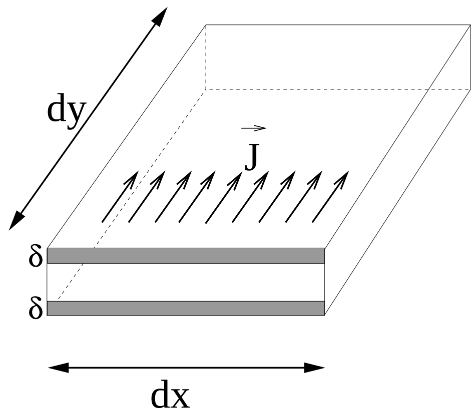

Figure 3.21: Schematic view of a thin metal plate supporting currents on both faces.

And using the fact that $\hat{n} \times \vec{H}(\vec{r})$ is the "near-surface" current $\vec{J}(\vec{r})$ (in A/m) flowing on the metal, Eq. (2.57)is now replaced by:

$$\hat{n} \times \vec{E}_s(\vec{r}) - Z_m \vec{J}(\vec{r}) = -\hat{n} \times \vec{E}_i(\vec{r}) \tag{3.24}$$

And the Galerkin MoM matrix elements now reads:

$$Z_{mn} = \frac{1}{j\omega\epsilon} \int_S \vec{J}_m \cdot \left[(k^2 \overline{\overline{I}} + \nabla\nabla\cdot) \int_{S'} \vec{J}_n G(R)\, dS' - Z_m \int_{S'} \vec{J}_n\, dS' dS \right] \tag{3.25}$$

3.5.2 Dissipated power

Let the infinitesimal piece of thin metallic plate depicted in Fig. 3.21, support a total current density J distributed on both faces of the plate. The current is supposed to be non negligible over a depth equal to the skin depth δ on both faces. The power dissipated by ohmic losses in this piece of metal can be expressed as:

$$\begin{aligned} dP &= dR \frac{|I|^2}{2} && (3.26) \\ &= dR \frac{|J|^2 dx^2}{2} && (3.27) \\ & && (3.28) \end{aligned}$$

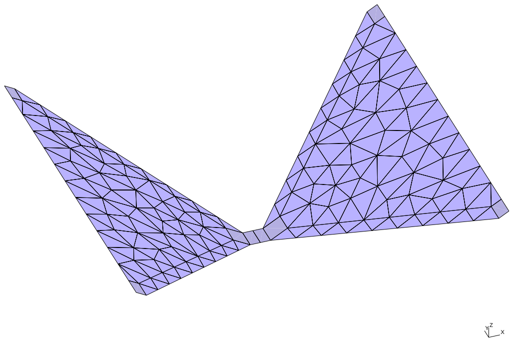

Figure 3.22: Unit cell for a TEM Horn array with 120° opening angle.

where I is the total current flowing on the piece of metal and J is the surface current density. The resistance dR is computed as:

$$\begin{aligned} dR &= \frac{\rho dy}{dA} \\ &= \frac{dy}{\sigma(\delta dx)} \end{aligned} \tag{3.29}$$

Where $\rho = 1/\sigma$ is the resistivity of metal and $dA = 2\delta\ dx$ is the total surface through which current flow is considered as non-negligible. Hence, the dissipated power can be computed as:

$$dP = \frac{|J|^2}{4\ \sigma\ \delta} dS \tag{3.30}$$

where $dS = dx\ dy$ is the surface of the metal piece. So the total dissipated power can be computed by integrating (3.30) on the whole metallic surface S.

$$P = \int_S \frac{|J|^2}{4\ \sigma\ \delta} dS \tag{3.31}$$

A way of verifying the consistency of the computation method consists in computing power budgets. The Poynting theorem stipulates that the real power absorbed by the active input impedance of the antenna corresponds to the power transferred into the far fields, plus the power dissipated as a result of ohmic losses. It can be written as follows:

$$Re\{Z_a\}\frac{|I_{in}^2|}{2} = \frac{a\ b\ cos\theta|E_a|^2}{2\eta} + \int_S \frac{|J|^2}{4\sigma\delta} dS \tag{3.32}$$

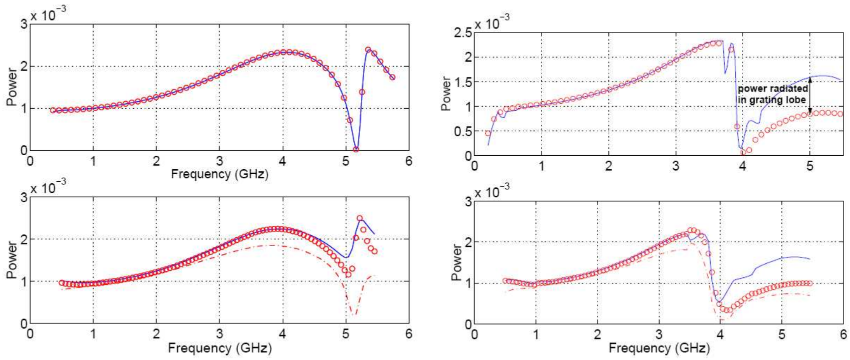

Figure 3.23: Verification of the Poynting theorem for the array of TEM horns whose unit cell is shown in Fig. 3.22 (spacing 5 cm, 120° opening angle) placed 2 cm above a ground plane. Left: broadside scan, Right: 30° scan in the E-plane. Top: without losses. Bottom: with a conductivity of $5\Omega^{-1}\text{cm}^{-1}$. Dashed line: power radiated in the direction of interest. Solid line: power delivered to the antenna (based on impedance). Circles: radiated power plus dissipated power.

where Z_a is the active input impedance, I_{in} is the port current, J is the surface current density, a and b are the element spacings of the array, E_a is the far radiated field, and θ is the angle of radiation from broadside. The magnitude of the far radiated field in the direction of the main lobe (we assume here a configuration without grating lobes) can be written as:

$$|E_a|^2 = \left(\frac{\eta}{2\ a\ b\ cos\theta}\right)^2 \left[\left| \int_S \vec{J} \cdot \hat{a}_h e^{j\vec{k}\cdot\vec{r}} dS \right|^2 + \left| \int_S \vec{J} \cdot \hat{a}_v e^{j\vec{k}\cdot\vec{r}} dS \right|^2 \right] \quad (3.33)$$

where $\hat{a}_h$ and $\hat{a}_v$ are unit vectors describing orthogonal polarizations in the direction of the main lobe, $\vec{k}$ is the vector wave number in that direction, and $\vec{r}$ are the coordinates of a point on the surface S of the antenna.

This identity has been verified for arrays of TEM horns with a 120° opening angle and with 5 cm spacings, placed 2 cm above a ground plane. The unit cell for this array is shown in Fig. 3.22. When losses are included in the analysis, the Method-of-Moments solution has been computed considering a surface impedance corresponding to a (very low) conductivity equal to $5\Omega^{-1}\text{cm}^{-1}$. Fig. 3.23 shows the different components of the power versus frequency. The left-side plots correspond to broadside observation. The power delivered to the antenna (cf. the input impedance) is represented by the solid line, while the power obtained from the radiated fields and losses in the conductors is represented by the circles. When there are no losses, the correspondence is surprisingly good. Knowing that the far radiated fields are variational with respect to the current distribution [56], this provides a good confidence on the value of the active input impedance. When losses are considered (bottom), the dashed line corresponds to the power radiated in the far fields. This is complemented by the losses in the conductors to correspond, within a good accuracy, to the power delivered to the antennas. To the author's best knowledge, this is the first time such a comparison is made for antennas in infinite arrays. On the right side of Fig. 3.23, results are shown for the same array scanned at an angle of 30° from normal in the E-plane. Striking is the deviation between the delivered power and the radiated (plus lost) power above 4 GHz. It should be noted that the far fields, as computed by Eq. (3.33), only concern the main beam. Near 4 GHz, a grating lobe enters visible space, and the available power has to be shared with it. When the grating lobe is very close to horizon, it conveys the major part of the radiated power; when it comes closer to broadside (at higher frequencies, here), the power radiated in that direction becomes comparable to the power radiated in the direction of the main beam.

3.6 Array Scanning Method (ASM)

3.6.1 Infinite array analysis

As explained above, the approach presented here and relying on infinite-array simulations reduces the unknowns involved in the simulation of periodic structures to one unit cell. The simulation code can efficiently analyze infinitely periodic structures by resorting to the doubly periodic Green's function. This method greatly reduces the computing time, but doing this, the excitation of the structure will also be periodized. However, when studying periodic structures such as FSS superstrates to increase the gain of a single radiating antenna or when one is interested in the central element pattern of a phased array, we want only one unit cell to be excited. The solution to this issue consists in using the *Array Scanning Method* [57], [58], [59]. This technique allows us to compute the response of a periodic structure to an excitation every N unit cell in both directions as a sum of N^2 responses where each unit cell is excited. This is illustrated in one dimension by equation (3.34) in which I_n is the current in the n^{th} cell when one cell over N is excited and $I^{\infty}(\psi_p)$ is the current flowing in a cell in the infinite array conditions with each cell excited and an inter-element phase shift ψ_p.

$$I_n = \frac{1}{N}\sum_{p=0}^{N-1} I^{\infty}(\psi_p)e^{-jn\psi_p} \quad \text{where} \quad \psi_p = p\frac{2\pi}{N} \tag{3.34}$$

As shown by Eq. (3.34), the array scanning method is just a discrete Fourier transform (DFT). The interesting property that is used here is the fact that the DFT of a sequence of ones has only one non zero element. This is illustrated in table 3.1 for $N = 4$ where each line describes the phases applied to successive unit cells in infinite array simulations with each cell excited. It is obvious that adding the excitations in the four lines is equivalent to simulating the same structure but with one cell over four excited. If N is taken large enough, depending on the strength

p \ n	0	1	2	3	4
0	0	0	0	0	0
1	0	$\frac{\pi}{2}$	π	$\frac{3\pi}{2}$	2π
2	0	π	2π	3π	4π
3	0	$\frac{3\pi}{2}$	3π	$\frac{9\pi}{2}$	6π
$\frac{\sum_{p=0}^{3} e^{j\psi_p}}{4}$	1	0	0	0	1

Table 3.1: Illustration of the excitation phases for ASM with N=4.

of the coupling between cells, the response of the cells surrounding the

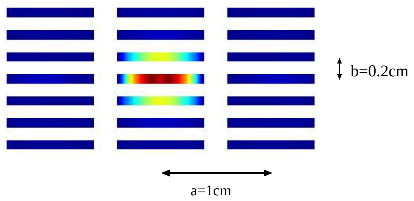

Figure 3.24: Structure of the dipole array. $\lambda = 1.56$, Ground plane $\lambda/4$ below the array.

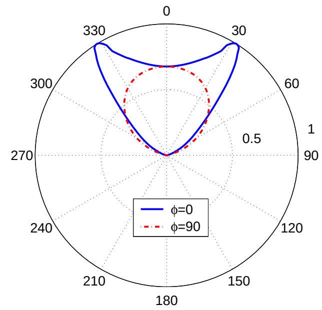

Figure 3.25: Element pattern for the infinite array computed with Eq. 3.35.

excitation will be close to the response obtained when only one cell is excited. Hence, the radiation pattern of this N-by-N array will be close to the infinite-array element pattern. In order to determine how large N should be to avoid interactions between successive excited cells, we can compare the pattern computed using the ASM with the radiation pattern of the infinite array where only one cell is excited. This pattern can indeed be obtained using Eq. (3.35) used in [55] in the receiving case, knowing that, by reciprocity the same relation holds on transmit:

$$\overline{F}_p(\hat{u}) = \int_S \vec{J}^{\infty}(\overline{r}) \cdot \hat{e}_p \, e^{jk\hat{u}\cdot\overline{r}} dS \tag{3.35}$$

$\overline{F}_p(\hat{u})$ is the radiation pattern in direction $\hat{u}$, $\vec{J}^{\infty}$ is the current in the unit cell of the infinite array when every cell is excited, $\hat{e}_p$ is the desired E field polarization and S is the unit cell surface. Fig. 3.25 shows the radiation pattern computed with Eq. 3.35 for the simple case of a dipole array depicted in Fig. 3.24. When N is large enough, depending on the strength of the coupling between cells, the pattern obtained with the ASM will be very close to the pattern of the infinite array with only one cell excited. Fig. 3.26 illustrates, for the dipole array shown above, the convergence of the radiation patterns with increasing values of N. The excellent agreement between the pattern obtained by Eq. 3.35 in Fig. 3.25 and the pattern obtained with the ASM considering N=31 obviously means that the current distribution computed with the ASM is very close to the current distribution in the case of only one cell excited.

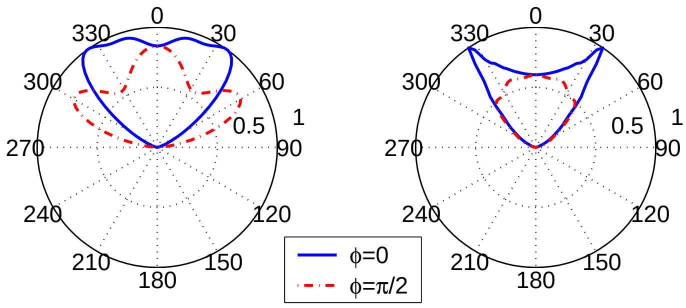

Figure 3.26: Convergence of ASM towards the infinite array solution. Left : N=5, Right : N=31

In practical situations, one should stop increasing N for example when the normalized RMS deviation between the infinite array pattern and the pattern computed with ASM is below a given value ϵ :

$$\int \frac{|\vec{E}^{\infty}(\theta) - \vec{E}^{ASM}(\theta)|^2}{|\vec{E}^{\infty}(\theta)|^2} d\theta < \epsilon \tag{3.36}$$

3.6.2 Finite array analysis

When finite array element patterns are needed, a simple windowing technique can be applied to the ASM results. After performing the ASM with a large enough N, as described in the previous section, infinite array currents when only one cell is excited are known in the excited cell and the $N^2 - 1$ surrounding cells. To obtain the central element pattern of a M-by-M finite array, with $M < N$, one only needs to integrate currents in the M^2 cells around the excited element, simply omitting the fraction of the ASM-computed current distribution that is beyond the physical size of the array. This obviously assumes that reflections at the edges of this new array can be neglected. Moreover, by moving the truncation window around the excited cell, it is possible to obtain the element patterns for any array element. Fig. 3.27 illustrates the truncation needed to obtain the central element pattern as well as a corner element pattern for a 3-by-3 finite array. This windowing technique was applied to ASM results

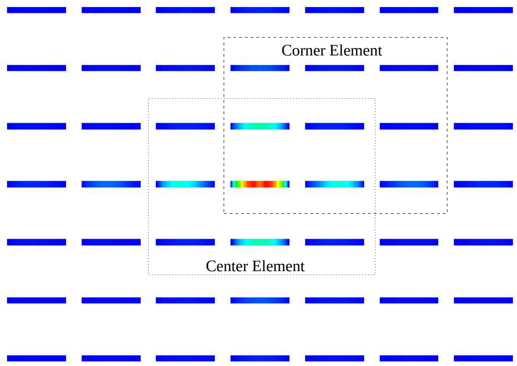

Figure 3.27: Truncation scheme for central element pattern (dashed) and corner element pattern (dotted) for a 3-by-3 finite array

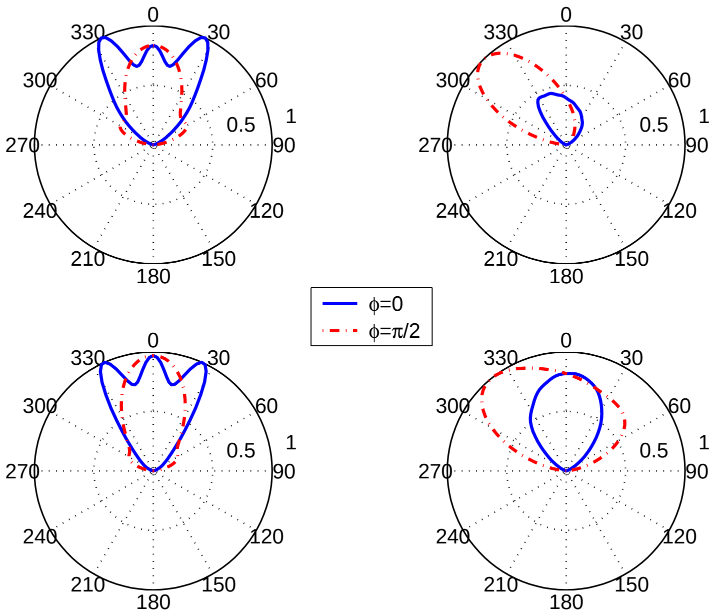

Figure 3.28: Element patterns : Left: Center element, Right: Bottom left Corner element Top row: Finite 7x7 array, Bottom row: ASM 31X31 truncated to 7X7

for the dipole array with $N = 31$ depicted in Fig. 3.24. The window size is 7-by-7 and the element patterns computed with this technique are compared to brute-force finite array simulation results. As shown in Fig. 3.28, the agreement between both methods is quite good for the center element but degrades significantly for an element in the corner of the array. A way of improving this technique and partially take reflections along the edges into account will be presented in the last section of this chapter, describing finite-by-infinite array simulations.

3.7 Dielectric structures

This section present simulations of infinite arrays of dielectric objects. As desribed in Section 2.2.4, when simulating dielectric objects, two different Green's functions are needed, as well as their gradient. In the simulation of an isolated dielectric object, the Green's functions G_{in} and G_{out} both have the same expression, except for the wavenumber, which depends on the media:

$$G_{in}(R) = \frac{e^{-jk_{in}R}}{4\pi R} \quad \text{and} \quad G_{out}(R) = \frac{e^{-jk_{out}R}}{4\pi R} \tag{3.37}$$

where $R = |\vec{r} - \vec{r}'|$ is the distance between source and observation points. When simulating periodic structures made of finite dielectric objects, the Green's function inside the dielectric object is the same as in the previous case. Indeed, as seen from inside the dielectric object, the influence of the outside medium (and the periodicity) is accounted for by equivalent electric and magnetic currents flowing on the boundary of the object. The case of infinite dielectric objects, such as infinite dielectric rods, will be treated in Section 3.8.5. However, in the outside medium, the doubly periodic Green's function has to be used and the unit cell is composed of a single object. Because the doubly periodic Green's function is not evaluated as quickly as a single exponential, it is computed and tabulated before filling the MoM impedance matrix. A second order interpolation technique is then used to evaluate the Green's function where needed.

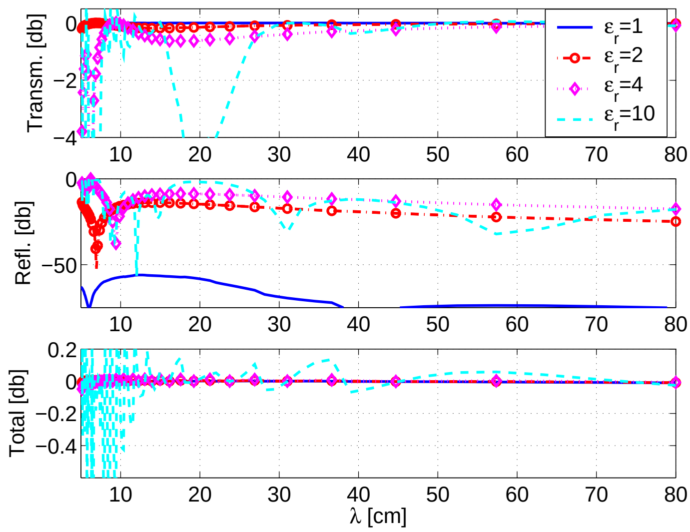

Figure 3.29: Transmission through an infinite array of spheres. Radius=2 cm, distances between spheres=4.2 cm.

3.7.1 Infinite array of spheres

Infinite array simulations have been validated on a doubly periodic dense array of spheres for several values of the dielectric constant. The transmission and reflection coefficients were computed and are shown in Fig. 3.29, as well as the sum of their squared magnitudes in order to check energy conservation. Fig. 3.29 shows that energy conservation is excellent: in most cases, the error does not exceed 0.01dB, except for high values of ϵ_r and high frequencies, where the error increases to a few tenths of a dB. It is worth noting that, as expected, the magnitude of the transmission coefficient obtained for $\epsilon_r = 1$ is constant at 0 dB over the whole frequency range. The unit cell of the array simulated in Fig. 3.29 is shown in Fig. 3.30 and contains 612 basis functions. The total computation time for each frequency point is about 7.5 minutes on a 2.5 GHz desktop computer (24 s for the tabulation of the Green's function and the 3 coordinates of its gradient, 7 min. for the filling of the impedance matrix and about 6 s for the inversion of the matrix).

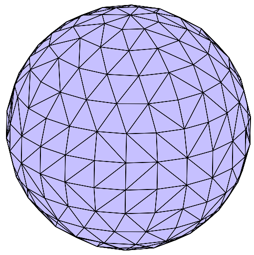

Figure 3.30: Mesh of the unit cell of an infinite array of spheres with 612 unknowns.

3.8 Finite-by-Infinite arrays

Given that couplings between elements are very strong in broadband arrays, the elements near the edges are in a completely different electromagnetic environment. Hence, those elements usually exhibit a strongly deviating behavior in terms of impedance matching and element pattern. Therefore, it is important to be able to correct the infinite-array predictions for the effects of truncation. A first step towards the simulation of finite arrays consists in considering structures which are infinitely periodic in one direction, and finite in the orthogonal direction. For instance, when the arrays under study are rectangular, the finite-by-infinite array solution provides correction factors that can be applied to the infinite-array result. This has been demonstrated in [61] by comparisons with brute-force solutions obtained for finite-by-finite arrays of tapered-slot antennas. Another approach was proposed in [62], which combines finite-by-infinite array simulation results and infinite-array solutions to estimate the element patterns in arrays finite in both directions. In the following, we will recall the basics of the analysis of finite-by-infinite arrays and present a fast iterative solution of the system of equations.

3.8.1 Singly periodic Green's function

The computational complexity associated with an array finite in one direction can only be reduced to the complexity related to a linear array by replacing the Green's function related to a point source to the one related to an infinitely periodic line of sources. As far as the elements are made of thin perfectly conducting sheets, the latter Green's function can be written as (cf. section 3.1.3):

$$G(R,x) = \frac{1}{4ja} \sum_{n=-\infty}^{\infty} e^{-jk_n x} H_0^{(2)}(\gamma_n R) \tag{3.38}$$

with

$$\gamma_n^2 = k^2 - k_n^2 = k^2 - \left(\frac{\psi_x}{a} + n\frac{2\pi}{a}\right)^2 \tag{3.39}$$

where a is the array spacing along $\hat{x}$, ψ_x is the phase shift between these elements, and R is the distance to the array axis. The Hankel functions appearing in (3.38) correspond to cylindrical waves radiated from the axis of the infinite array of sources. In this series, the propagating modes correspond to the values of n leading to a positive value for γ_n^2 in (3.39). They correspond to the main and grating lobes of the infinite array of dipoles. All the other modes are evanescent. It should be noted that the estimation of the Hankel functions involved in expression (3.38) requires a relatively large computation time. In this case, the Green's function is also tabulated, but as it depends only on two spatial coordinates, tabulation only requires a limited amount of memory and second order interpolation turns out to be several times faster than the direct estimation of the function. The singular behavior of the successive Hankel functions combine with each other to generate the $1/R$-type singularity appearing near each source.

3.8.2 Iterative solver

As it is well known, the periodicity of the array leads to a block-Toeplitz structure for the Method-of-Moments impedance matrix. Specific techniques exist for the solution of block-Toeplitz systems. However, compared to the solutions of problems without structure, the time saving is only proportional to the number of antennas. This is why we resort to iterative techniques, as the Stabilized bi-conjugate gradient technique

(Bi-CGstab, [63]). Contrary to the basic Conjugate Gradient technique, convergence is not absolutely garanteed. However, through the use of a proper pre-conditionner, the convergence is practically always achieved, and a five or six digit accuracy is generally obtained within ten to twenty iterations. The preconditioner used here consists of inverting once and for all a block-Toeplitz matrix corresponding to a smaller problem, with p antennas in the finite-array direction ($p = 3$ is the value we considered for our computations). Let us denote by Z_p this smaller impedance matrix, and write the entire block-Toeplitz system as $Zx = v$. If the array has N elements in the finite-array direction, Z has $N \times N$ blocks, and x and v are composed of N smaller vectors x_i and v_i, corresponding to basis and testing functions located on successive antennas. Then, an approximate solution is obtained rapidly by considering the solutions of the following systems:

$$Z_p \begin{bmatrix} x_i \\ \vdots \\ x_{i+p-1} \end{bmatrix} = \begin{bmatrix} v_i \\ \vdots \\ v_{i+p-1} \end{bmatrix} \tag{3.40}$$

for $i = 1 \; to \; N - p + 1$.

As Z_p is inverted once and for all (decomposed in LU form, in fact), the pre-conditioning operation is much faster than the matrix-vector products appearing elsewhere in the iteration procedure.

3.8.3 Application to the array truncation analysis

Standing waves in a finite-by-infinite planar bicone array

Fig. 3.32 shows the active input impedances for both polarizations of a planar bicone array with 16 elements in the finite-array direction depicted in Fig. 3.31. Each port presents a series impedance of 50 Ω. The left pictures represent the impedance for the polarization parallel to the infinite-array direction, while the right picture describes the impedance for the polarization perpendicular to the infinite-array direction. In both cases, deviations from the infinite array solution are the strongest for the outer elements while the impedances are very close to each other further

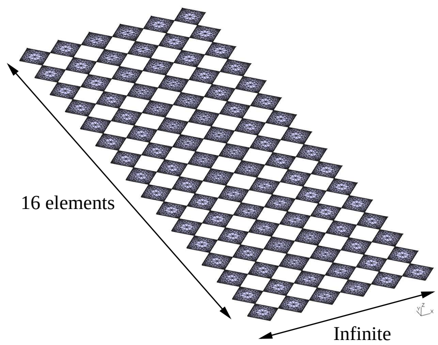

Figure 3.31: Structure of the finite-by-infinite planar bicone array with 16 elements in the finite-array direction.

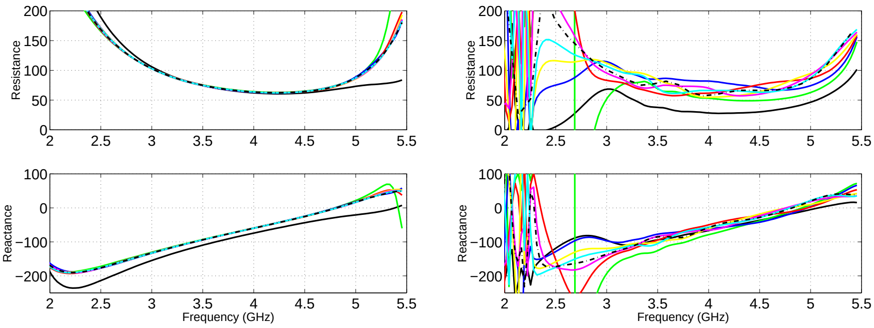

Figure 3.32: Active input impedances for the planar bicone 2 cm above a ground plane, with 5 cm spacing and 16 elements in the finite-array direction. Left: feed parallel to infinite-array direction. Right: feed perpendicular to finite-array direction. The curves represent the input impedances of antennas located in the successive lines along the finite-array direction.

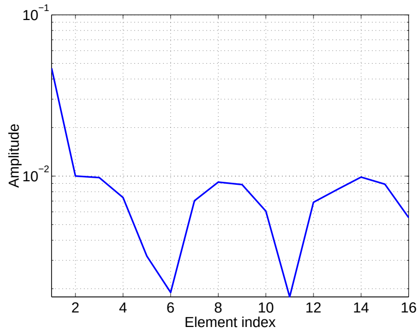

Figure 3.33: Amplitude of currents on successive elements of the finite-by-infinite planar bicone array with ground plane at 2 cm, with first element fed only, polarization parallel to the finite-array direction, at 471 MHz.

inside the array. When the feed is parallel to the finite-array direction, the deviations between elements are very large, and the results becomes completely chaotic at lower frequencies. Simulations performed at lower frequencies showed a number of strong and regularly spaced resonances. This is most probably due to resonances involving the whole finite-array length. This is illustrated by Fig. 3.33, which corresponds to excitation at just the first element (more exactly, the first infinite line of elements). Currents through the successive ports are shown. The resonance is very clear; the length of a double oscillation in Fig. 3.33 corresponds to approximately 11 spacings, while the free-space wavelength is about 12.7 spacings. It should be noted that, given the shape of the elements, it may be expected that they tend to lengthen the electrical path (cf. the current distribution in Fig. 3.3).

3.8.4 Computation of array element patterns with ASM and windowing

As shown in Section 3.6.2, when computing finite-array element patterns using infinite-array simulations and a windowing technique, the accuracy of the results is quite good for the center element of the array, but it

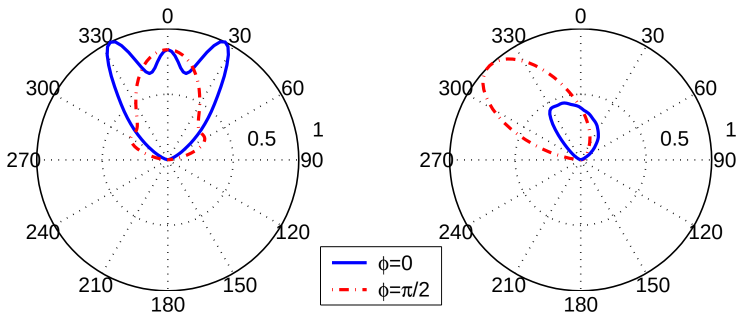

Figure 3.34: Element patterns based on finite-by-infinite array simulations and ASM. Left: Center element, Right: Bottom left Corner element.

degrades significantly for elements located close to the edges or in the corner of the array. To overcome this problem, it is possible to improve our approach thanks to finite-by-infinite array simulations. Indeed, to approximate the 7-by-7 finite array, one can simulate an array that is finite in the direction where couplings between cells are the strongest and infinite in the other direction. Doing this automatically includes the effects of truncation in the finite direction and hence should improve the results. In the infinite-array direction, the ASM can still be used and the results truncated as explained in section 3.6.2. Fig. 3.34 illustrates the excellent results achieved with this new approach. Indeed, these radiation patterns perfectly match those presented for the finite array (top row of Fig. 3.28), even for the corner element. One should notice that when using the finite-by-infinite array approach, although the unit cell is bigger (7 times bigger in this case), the computation cost can be kept very low thanks to the use of 1D periodic Green's function and to the iterative solver.

3.8.5 Dielectric EBG superstrate

In general, EBG materials are comprised of a periodic array of metallic or dielectric elements and are characterized by stop bands and pass bands. This property was already illustrated in section 3.4.1 in the case of a

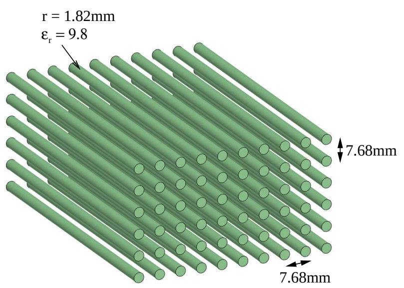

Figure 3.35: Dielectric EBG structure.

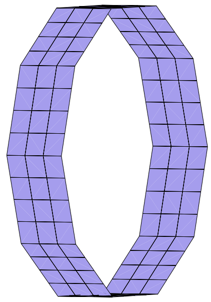

Figure 3.36: Unit cell for the single layer EBG.

metallic EBG structure. Another interesting property of EBG materials is that they display localized frequency windows within the forbidden frequency band when the periodicity is broken up by some defects. This property is very useful for improving the directivity of an antenna when using the EBG structure as its superstrate [52]. In this section, a method resorting to the singly periodic Green's function to simulate infinite dielectric EBG materials will be presented. In order to simulate an infinite dielectric EBG, as the one shown in Fig. 3.35, a slightly different method than the one presented in Section 3.7 has to be used. A Green's function for singly infinite arrays of line sources could be used. However, we wanted to be able to treat this case with the formulation presented in 3.7, assuming very minor changes. In this case, the dielectric object to be simulated is infinite and the unit cell is made of thin slices of dielectric rods (Fig. 3.36). As seen from the exterior medium, these slices are periodized in both directions and the doubly periodic Green's function is used. However, as seen from inside the rods, the unit cell must be periodized in only one direction, along the rods. Hence, for interior integrals, the singly periodic Green's function is used. The rods are discretized using roof-top basis functions defined on rectangular domains, as shown in Fig. 3.36 and overlapping basis functions are added along one edge of the unit cell to allow the equivalent currents to flow from one cell to the next. The transmission and reflection coefficients of a plane

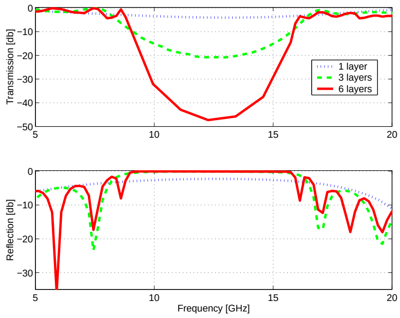

Figure 3.37: Transmission and reflection coefficients of a plane wave through the EBG depicted in Fig. 3.35.

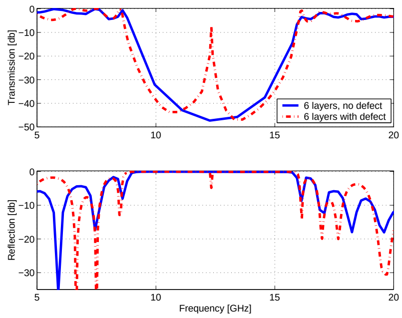

Figure 3.38: Transmission and reflection coefficients of a plane wave through the 6 layers EBG with and without defect.

wave through several layers of rods are presented in Fig. 3.37 where the typical band-gap exhibited by these structures is shown. Fig. 3.38 compares those coefficients for a 6 layers EBG with and without a defect. The defect introduced consists of an increased distance between the 3rd and 4th layers of rods. When this distance is increased to 26.1mm, a transmission peak is observed in the middle of the band-gap. These results are in excellent agreement with those presented in [52], which were obtained with the help of the FDTD method and are shown in Fig. 3.39. The green curve (corresponding to a defect length of 1.7 times the periodicity corresponds to the red dashed curve shown in Fig. 3.38 while the red curve (no defect) is to be compared to the blue solid curve in Fig 3.38.

3.9 Conclusion

In this chapter, we showed how fast infinite-array simulations can be used, in a first instance, for the analysis of large periodic structures. Then, a way of estimating the effects of truncation, relying on finite-by-infinite array simulations was presented. The key concepts developed in this chapter are the following:

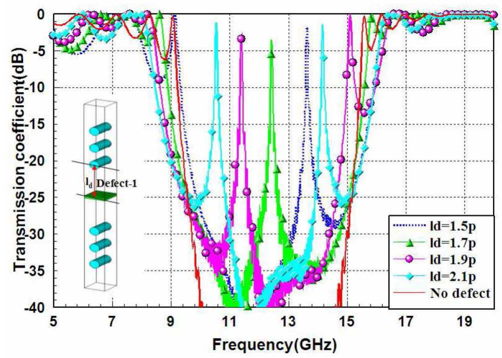

Figure 3.39: Transmission coefficients of a plane wave through the EBG depicted in Fig. 3.35 for several values of the periodicity defect (from [52]).

- Efficient formulations for the periodic Green's function and its gradient.
- Computation of the transmission and reflection properties of periodic structures.
- Modelling of Ohmic losses.
- Array Scanning Method with 3D objects used for the simulation of periodic structures with a single excitation + convergence criterion.
- Truncation analysis: Finite-by-infinite array approach with iterative solver, windowing.
- Validations: Comparison with measurements and FDTD simulations, energy conservation.

Eigenmode analysis

4

This chapter describes how dispersion curves of periodic structures can be computed numerically with the MoM code and presents some application examples. The knowledge of dispersion curves may be very helpful in the design of metamaterial based antennas. Indeed, they can inform about the frequency ranges and directions in which wave propagation is allowed as well as the value of the phase velocity. The first section describes how these curves can be computed with the MoM code. Then the dispersion in single and double wire media is analyzed. Finally a waveguide filled with a double wire medium is studied and it will be shown that waves can propagate below the cut-off frequency of such a waveguide. This phenomenon is very interesting because it allows to reduce the size of waveguide based antennas.

4.1 Computation of eigenmodes

As described in Section 2.2.1, the MoM system of equations reads:

$$\mathbf{Z} \cdot \mathbf{I} = \mathbf{V}$$

Where $\mathbf{Z}$ is the N-by-N MoM impedance matrix (if there are N unknowns), $\mathbf{I}$ is the column vector containing the N unknowns describing the currents and $\mathbf{V}$ is the excitation vector (fields impressed on the N basis functions). The eigenmodes of the structure are modes that can propagate (hence current flows in the structure) although there is no excitation and are therefore characterized by a singular impedance matrix. For a three-dimensional periodic structure, the search for eigenmodes is carried out by searching the values of the frequency f and of the phase shifts between successive unit cells, ψ_x,ψ_y and ψ_z, in the three directions of space that produce an impedance matrix with a zero determinant. We then get the dispersion relation $f = f(\vec{k})$ binding the frequency to the wavevector $\vec{k}$. It is worth noting that this relation is a periodic function of $\vec{k}$ and, thanks to this periodicity, the search for eigenmodes only needs to be carried out in a unit cell of the reciprocal lattice of the periodic structure. Generally, this search is performed in the so-called *first Brillouin zone*. Furthermore, the first Brillouin zone may be redundant if the periodic structure possesses additional symmetries, such as mirror planes. By eliminating the redundant regions, one obtain the *irreducible Brillouin zone* [53].

The accuracy of this technique is demonstrated on a simple structure consisting of an infinite waveguide with a square cross-section. The unit cell of this waveguide is shown in Fig. 4.1. The singly periodic Green's function is used to periodize this cell along the axis of the guide (x axis) and hence computing the impedance matrix for the infinite waveguide for several values of the frequency f and wavevector k_x. A map of the values obtained for the determinant of the impedance matrix is shown in Fig. 4.2. The horizontal axis represents the amplitude of the wavevector k_x and the vertical axis represents the frequency, normalized to the cut-off frequency of the dominant mode of the waveguide, i.e. the TE_{10} mode. Dark regions indicate low values of the determinant. The dispersion curve for the TE_{10} and TE_{01} modes is clearly visible as the dark line starting at $\omega/\omega_c = 1$. These two modes are identical as the waveguide has a square cross-section. The dispersion curve for the next higher order mode, TE_{11}, is also visible, starting at $\omega/\omega_c = \sqrt{2}$. The third line visible in the bottom right of the picture is the dispersion curve of free-space. It is present because, in addition to modes that can propagate inside the waveguide, waves can obviously also propagate in the outside medium

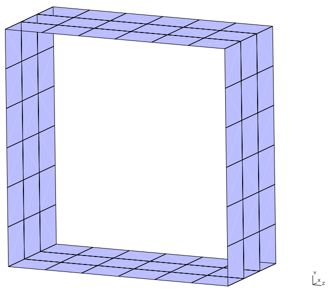

Figure 4.1: Unit cell for an infinite waveguide with square cross-section.

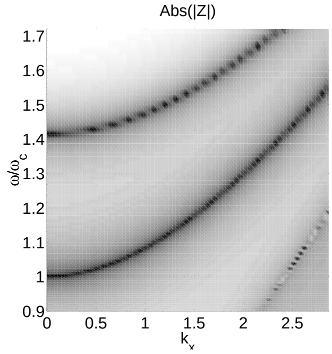

Figure 4.2: Dispersion curves obtained for an infinite waveguide with square cross section.

which is just free-space. The dispersion curves for these three modes were computed analytically [54] and plotted in Fig. 4.3 for comparison. For the TE_{10} mode, the dispersion relation reads:

$$\frac{\omega}{\omega_c} = \sqrt{1 + \left(\frac{k_x a}{\pi}\right)^2}$$

For the TE_{11} mode, one has:

$$\frac{\omega}{\omega_c} = \sqrt{2 + \left(\frac{k_x a}{\pi}\right)^2}$$

and for free-space:

$$\frac{\omega}{\omega_c} = \frac{k_x c}{\omega_c}$$

Where a is the width and height of the waveguide with a square cross-section, c the speed of light in free-space and ω_c the cut-off frequency of the waveguide. Comparing Figs. 4.2 and 4.3, it is obvious that our numerical method correctly computes the dispersion relations. This technique has been extended to the analysis of structures periodic in the three directions of space, such as wire media.

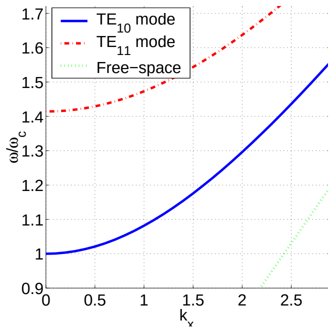

Figure 4.3: Theoretical dispersion curves obtained for an infinite waveguide with square cross section.

4.2 Single wire medium

A single wire medium is made of a doubly periodic lattice of parallel conducting wires. The transmission properties of such a medium have already been studied in Section 3.4.1, where the structure was limited to a few layers. We also showed the equivalence between wires with circular cross-section and thin strips as long as the width of the strips is four times the radius of the wires. Using thin strips allows us to reduce the number of unknowns involved and to get faster simulations.

4.2.1 Green's function periodic in the three directions of space

In order to compute the dispersion curves of this wire medium, the unit cell is made of a short piece of metallic strip and the Green's function periodic in the three directions of space is used. The periodicity along the wire axis creates infinite wires, while periodicity in the two other directions fills the whole space with infinite parallel wires. This new Green's function is computed from the doubly periodic Green's function (periodic along x and y) described in Section 3.1 as follows.
Assuming a periodicity dz along the z axis and a phase shift ψ_z between

successive layers yields:

$$G_{3D}(x,y,z) = \sum_{p=-\infty}^{\infty} G_{2D}(x,y,z+p\cdot dz)\; e^{jp\psi_z} \tag{4.1}$$

Where $G_{2D}(x,y,z)$ is the double periodic Green's function. For the "on-plane" case, the formulation (3.7) is used far from the first line of point sources (x axis) and the direct summation (3.4) is used closer from this line (cf. Section 3.1.3). For the "off-plane" case, the formulation (3.3) is used, where the doubly periodic Green's function is expressed as a sum of propagating and evanescent cylindrical waves. Hence, the computation is carried out in two steps, as expressed by Eq. (4.2).

$$G_{3D}(x,y,z) = G_{2D}(x,y,z) + \sum_{\substack{p=-\infty \\ p\neq 0}}^{\infty} G_{2D}(x,y,z+p\; dz) e^{jp\psi_z} \tag{4.2}$$

The "on-plane" case is treated as needed in the first term and the second term can be computed with the formulation (3.3).

$$\begin{aligned} G_{3D}(x,y,z) &= G_{2D}(x,y,z) \\ &+ \frac{1}{2jab} \sum_{\substack{p=-\infty \\ p\neq 0}}^{\infty} \sum_{m=-\infty}^{\infty} \sum_{n=-\infty}^{\infty} \frac{e^{-j\gamma_{mn}|z+p\cdot dz|} e^{j(\beta_m x+\beta_n y)}}{\gamma_{mn}} e^{jp\psi_z} \end{aligned} \tag{4.3}$$

Reorganizing the summations, one can write:

$$\begin{aligned} G_{3D}(x,y,z) &= G_{2D}(x,y,z) \\ &\quad + \frac{1}{2jab} \sum_{m=-\infty}^{\infty} \sum_{n=-\infty}^{\infty} \frac{e^{j(\beta_m x+\beta_n y)}}{\gamma_{mn}} \\ &\quad \cdot \left(\sum_{p>0} e^{-j\left[\gamma_{mn}(z+p\cdot dz)+p\psi_z\right]} + \sum_{p<0} e^{-j\left[\gamma_{mn}(-z-p\cdot dz)+p\psi_z\right]} \right) \end{aligned} \tag{4.4}$$

And the expression between parentheses can be rewritten:

$$\begin{aligned}
&\sum_{p>0} e^{-j\left[\gamma_{mn}(z+p\cdot dz)+p\psi_z\right]} + \sum_{p>0} e^{-j\left[\gamma_{mn}(-z+p\cdot dz)-p\psi_z\right]} \\
&= e^{-j\gamma_{mn}z} \sum_{p>0} e^{-jp(\gamma_{mn}dz-\psi_z)} + e^{j\gamma_{mn}z} \sum_{p>0} e^{-jp(\gamma_{mn}dz+\psi_z)} \\
&= e^{-j\gamma_{mn}z} \left(\frac{1}{1-e^{-j(\gamma_{mn}dz-\psi_z)}} - 1 \right) + e^{j\gamma_{mn}z} \left(\frac{1}{1-e^{-j(\gamma_{mn}dz+\psi_z)}} - 1 \right)
\end{aligned} \tag{4.5}$$

This last step uses the fact that $\sum_{p=0}^{\infty} q^p = \frac{1}{1-q}$ and avoids an additional summation on the variable p. Hence the computational complexity for the tabulation of the Green's function periodic in the three directions of space remains comparable to the case of the tabulation of the doubly periodic Green's function!

4.2.2 Dispersion curves for the single wire medium

Using this new periodic Green's function, it is now possible to compute the dispersion curves for the single wire medium depicted in Fig. 4.4, with an infinite number of layers. Simulation results are shown in Fig. 4.5. The blue curves correspond to the dispersion obtained with a zero phase shift between successive wires along x and describes waves propagating along the z axis. Comparing these blue curves with the transmission properties through 6 and 12 layers presented respectively in Figs. 3.6 and 3.7, one can note the perfect correspondance of the band-gap position (between 24 GHz and 30 GHz) and the cut-off frequency near 13 GHz. Looking at the lowest blue curve ($\psi_x = \psi_y = 0$) of Fig. 4.5, just below 15 GHz, the phase shift ψ_z is also close to zero. This means that, at these frequencies, modes can propagate within this structure with a phase shift between successive wires that is very low or null in both directions. This in turn means that the phase velocity of these modes is very high and hence the refractive index is very low. This is a proof that this medium behaves as an homogeneous medium with a very low effective permittivity. This property can be used to design high gain antennas, as it will be shown in section 5.1.

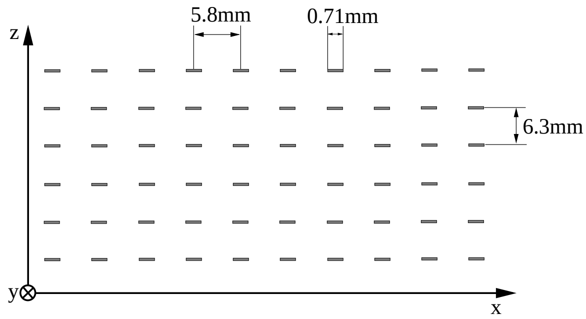

Figure 4.4: Description of the single wire medium.

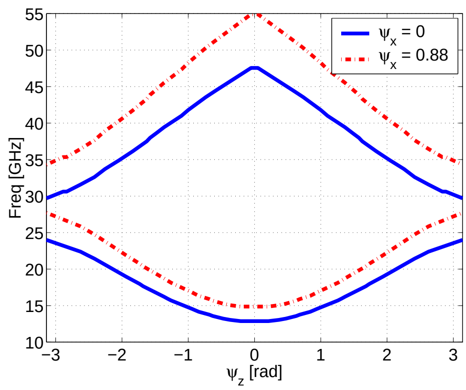

Figure 4.5: Dispersion curves for the single wire medium described in Fig. 4.4. The blue curve ($\psi_x = \psi_y = 0$) corresponds to a propagation along the z axis.

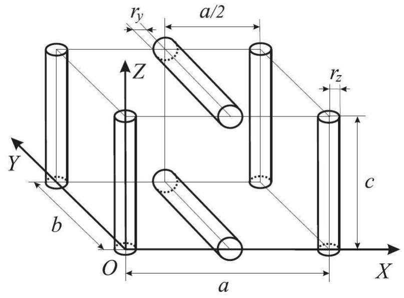

Figure 4.6: Geometry for the double wire medium unit cell. From [60].

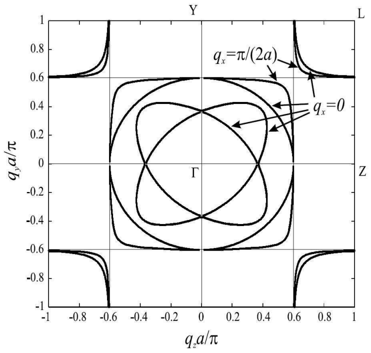

Figure 4.7: Isofrequency contours for double wire media at $ka/(2\pi) = 0.3$. Two cases $\psi_x = 0$ and $\psi_x = \pi/(2a)$ are presented. In this figure (from [60]), the phase shifts ψ_x, ψ_y and ψ_z are respectively noted q_x, q_y and q_z.

4.3 Double wire medium

To further validate the computation technique for eigenmodes, double wire media were also studied numerically. A double wire medium (DWM) is also made of infinite arrays of parallel wires, but wires in two successive layers are orthogonal to each other. The unit cell for a DWM is presented in Fig. 4.6. The properties of DWM have been investiguated analytically in [60] and some dispersion curves obtained are presented in Fig. 4.7. These are isofrequency contours, i.e. relations between phase shifts in 2 directions q_y and q_z (or between 2 components of the wavevector) of the modes that can propagate in the structure. Our numerical results computed with the same parameters are presented in Figs. 4.8 and 4.9 and striking is the excellent agreement with analytical curves.

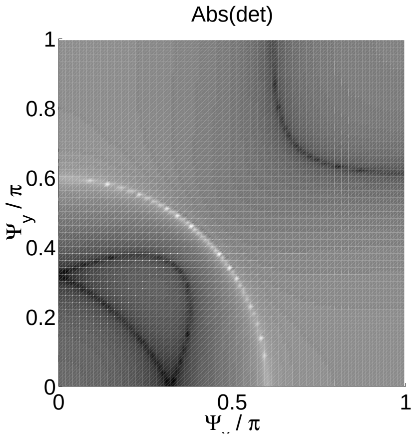

Figure 4.8: Simulated isofrequency contours for double wire media at $ka/(2\pi) = 0.3$ and $\psi_x = 0$.

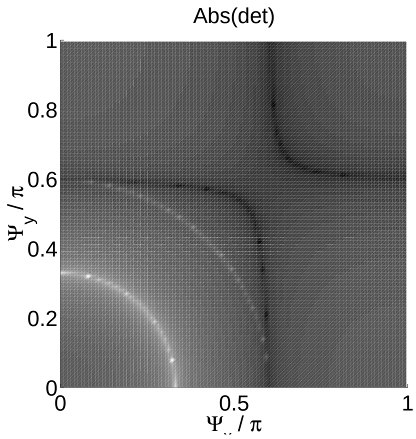

Figure 4.9: Simulated isofrequency contours for double wire media at $ka/(2\pi) = 0.3$ and $\psi_x = \pi/(2a)$.

4.4 Application to the analysis of backward waves in a waveguide filled with a wire medium

As previously mentioned in section 2.3.2, and will be demonstrated in section 5.2, slotted waveguides can be useful as primary sources for metamaterial based antennas. Hence, this section is devoted to the study of waveguides filled with a wire medium. As it will be shown, very interesting properties arise in such structures. This work was carried out in collaboration with Prof. I. Nefedov who was in charge of the analytical part of the study while we confirmed these analytical models with our MoM simulations.

The concept of metamaterials has been found useful in many applications, from low frequencies to optics. They can be designed to achieve properties with respect to electromagnetic waves that cannot be found in nature. An important role among metamaterials is played by artificial media with negative permittivity and permeability. Having both of these parameters negative is a sufficient condition for propagation of backward waves in such structures (backward waves are referred to waves whose phase and group velocities are directed oppositely). Media with one of the parameters negative are also of great interest, namely, wire media (the media formed by lattices of ideally conducting parallel thin wires). A single wire medium (WM), two-dimensional periodic lattice of thin conducting wires, can be described as a uniaxial material, whose relative permittivity tensor can be written as (the wires are in the z direction)

$$\overline{\overline{\epsilon}} = \begin{pmatrix} \epsilon_h & 0 & 0 \\ 0 & \epsilon_h & 0 \\ 0 & 0 & \epsilon_z \end{pmatrix} \tag{4.6}$$

where ϵ_z is expressed by the well-known Drude formula

$$\epsilon_z = \epsilon_h \left(1 - \frac{\omega_p^2}{\omega^2 \epsilon_h}\right) = \epsilon_h \left(1 - \frac{k_p^2}{k^2}\right) \tag{4.7}$$

Here ϵ_h is the permittivity of the host medium, $k = \omega/c\sqrt{\epsilon_h} = k_o\sqrt{\epsilon_h}$ and c is the speed of light. The constant ω_p (or the corresponding k_p) is an equivalent "plasma frequency". However, formula (4.7) is correct only if a wave propagates perpendicular to the wires. It has recently been shown that if the wavevector in a wire medium (WM) has a nonzero component along the wires, the plasma model (4.7) gives nonphysical results [65]. The plasma model has been corrected introducing spatial dispersion (SD) into formula (4.7):

$$\epsilon_z = \epsilon_h \left(1 - \frac{k_p^2}{k^2 - k_z^2}\right). \tag{4.8}$$

Recently J. Esteban et al. [66] have shown that if one inserts a WM sample into a rectangular waveguide, propagation of backward waves below TE_{10} mode cutoff becomes possible. Thus, it is not necessary to be in presence of a double negative metamaterial; a negative permittivity is sufficient. In this section, we will examine the structure considered in [66], revising the explanation given by authors for the effect of backward wave propagation. Low-order modes will be studied in the waveguide under different types of filling. We will compare results, given by the

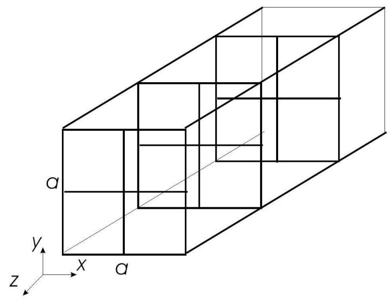

Figure 4.10: Double wire medium in a square waveguide.

effective medium theory and two different realisations of the Method of Moment (MoM). Geometries with connected and non-connected wires are compared, as well as the influence of the wire connection with the waveguide walls.

4.4.1 Waveguide filled with DWM, effective medium models

A square cross-section waveguide, filled with a *double wire medium* (DWM), formed by two mutually orthogonal wire lattices, is shown in Fig. 4.10. The double wire medium can be made in two topologies, connected and non-connected [67], and these kind of DWM exhibit different wave properties.

Note that, very recently, the DWM has been studied in details, using analytical and different numerical methods, [67]-[69]. In [69] a very good agreement between the results given by the effective medium and full-wave theories for all types of waves in DWM (if the wires are thin) has been demonstrated. In addition, the effective medium (EM) model gives good results not only at low frequencies, but also above plasma resonance, i.e. $\omega > \omega_p$.

The following explanation, based on the effective medium model, was given in [66] for the existence of backward waves in the structure of Fig. 4.10. If mutually perpendicular wires are identical, the medium inside the waveguide can be considered as a uniaxial crystal with permittivity dyadic components $\epsilon_t = \epsilon_{xx} = \epsilon_{yy}$, $\epsilon_{zz} = \epsilon_h$, where ϵ_t is expressed by the conventional formula (4.7) and is negative at low frequencies. Then, the known formula for the propagation constant γ of guided TM modes in a waveguide filled with a uniaxial crystal, is used:

$$\gamma^2 = \epsilon_t \left[k_0^2 - (k_x^2 + k_y^2)/\epsilon_h\right] \tag{4.9}$$

where $k_x = k_y = \pi/a$. Obviously, formula (4.9) predicts propagating waves below cutoff and below plasma resonance. Moreover, it leads to a countable spectrum of propagating waves at low frequencies; that can be seen if one takes $k_x = m\pi/a$, $k_y = n\pi/b$. For any low k_0, we can find m and n such that wave propagation becomes possible, which looks weird. In [65] and [69] it is shown, that these unphysical results disappear if one uses an EM model that takes into account spatial dispersion.

Namely, application of formula (4.8) in EM theory yields the following expression for γ, assuming that $k_y = k_x$ [69].

$$\gamma^2 = k_0^2\epsilon_h - k_p^2 \pm \frac{k_x^2 k_p^2}{k_0^2\epsilon_h - k_x^2} - 2k_x^2. \tag{4.10}$$

This formula does not allow propagation of a countable spectrum of modes, in opposition to formula (4.9). However, the formula (4.9) relates to non-connected geometry, and in [66] the connected topology was considered (see Fig. 10 of [66]). Applicability of formulas (4.9) and (4.10) for both geometries as well as difference between their spectra of modes is discussed below.

The next important issue is the correct model for computing the plasma frequency. This problem seems important to us for the interpretation of the results obtained in the framework of effective medium theories.

The most generally used are the following formulas:

1. Formula from [70]:
$$k_p^2 = \frac{2\pi}{d^2 \ln{(d/r)}}, \tag{4.11}$$
where d and r are the period and the radius of WM lattice, respectively.

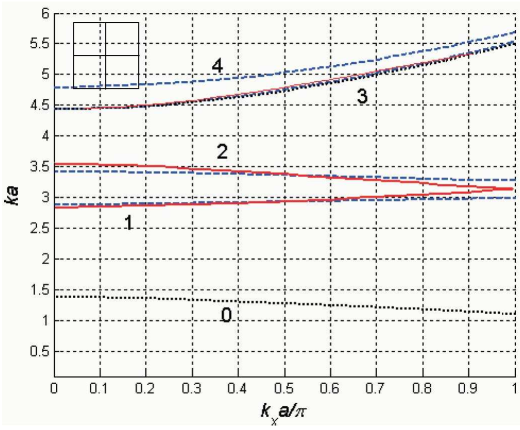

Figure 4.11: Spectrum of modes for circular wires and non-connected geometry. Inset shows the cross-section. Dotted curve – dispersion, calculated using formula (4.9), dashed curves – results obtained from formula (4.10), solid curves – results of Green's function method.

2. Formula from [72]:

$$k_p^2 = \frac{2\pi}{d^2 \left(\ln \frac{d}{2\pi r} + 0.5275\right)}. \tag{4.12}$$

The results, given by formulas (4.11) and (4.12), as well as by another proposed model, have been compared in [71]. A little difference was shown between models developed in [72] and [71] for thin wires, but also a strong difference with Pendry's formula (4.11), which does not take into account the interaction between wires. Namely, even for thin wires with $r/d = 0.01$, considered by us here, formulas (4.11) and (4.12) give $k_p d \simeq 1.17$ and $k_p d \simeq 1.38$, respectively that makes results obtained by the use of (4.11) too rough. The applicability of the effective medium theory for DWM, composed of thin wires and using the formula (4.12) for the plasma wavenumber, was proven in [69] comparing the results obtained from Eq. (4.10) with the results from full-wave simulations.

4.4.2 Spectrum of eigenmodes

We first consider the waveguide, loaded by wires as shown in Fig. 4.10 (one lattice period within the cross section and period of WM in z-direction is the same, equal to a). The ratio $r/a = 0.01$ leads to the plasma wavenumber $k_p a \approx 1.38$ and the wires are assumed to be non-connected. In Fig. 4.11, we compare results, given by formula (4.9), which was used by authors of [66] with the results obtained in the framework of the corrected EM theory (4.10) and those of the Green's function method, described in [69]. We can use for a waveguide structure the same algorithm as for a periodic structure, taking phase shifts per period $\psi_x = \psi_y = \pi$ and controlling the field distribution which must correspond to electric walls at $x = \pm a/2$ and $y = \pm a/2$. We can see a good agreement between the results of the corrected EM and full-wave theories. It is remarkable that two low-order pass bands lie above the plasma wavenumber, which is equal to $1.38/a$ for the chosen wires parameters, though below cutoff, which is equal to $4.44/a$ for TM_{11} mode. Striking is that the first pass band lies even below cutoff for the dominant mode TE_{10} mode. This is obviously very promising for the miniaturization of waveguide based antennas. In opposite, the result, obtained from formula (4.9) (the curve, marked by '0'), strongly differs from the one described above and provides a wave propagating below the plasma frequency. In addition, under the taken parameters and geometry, the backward wave belongs to the second passband and the lowest mode is a forward wave. Also two higher-order modes, propagating above cutoff, are shown in Fig. 4.11.

A similar structure has been simulated by using full-wave MoM. However, the wires have been taken as thin strips whose width w satisfies the condition $w = 4r$ that approximately gives the same plasma frequency for strip-like WM as for circular cross-section WM with the radius of wires r (in the case of thin wires and narrow strips). Thus the strip-like WM with $w/a = 0.04$ is equivalent to the circular WM with $r/a = 0.01$ (cf. section 3.4.1 and Fig. 3.8). The results obtained are in a good agreement both with analytical and Green's function [69] methods for

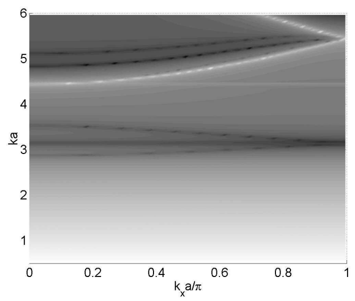

Figure 4.12: Spectrum of modes for the strip-like wires and non-connected geometry. Map of the determinant of the MoM impedance matrix. Nulls are black (eigenmodes) while peaks are white. The position of the TE_{10} mode cutoff corresponds to $ka = \pi$.

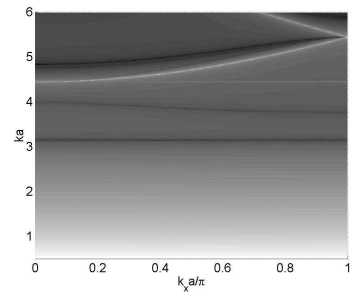

Figure 4.13: Spectrum of modes for the strip-like wires and connected geometry. Map of the determinant of the MoM impedance matrix. Nulls are black (eigenmodes) while peaks are white.

two lowest modes. The black horizontal line in the middle of forward and backward modes corresponds to the cutoff of the TE_{10} mode and white line corresponds to the free space mode. Next, we consider the connected geometry, with the map of determinant in Fig. 4.12. Here we see that the lowest forward mode is absent. This result is in agreement with that obtained by Esteban et al, [66]. However, other modes are similar to those marked by '1' and '3' for the non-connected geometry and they are well described by the model (4.10), not by (4.9) which was used in [66]. Then, we consider the waveguide, filled with a non-connected circular WM, as shown in the inset of Fig. 4.14. In this case the period of WM in all three dimensions is $d = a/2$ and the phase shifts per period of WM in x and y directions are $\psi_x = \psi_y = \pi/2$. It corresponds to the phase shift π across the waveguide walls, as it takes place for the TM_{11} mode. Calculations have been made using formula (4.10) as well as with the Green's function method and the results are presented in

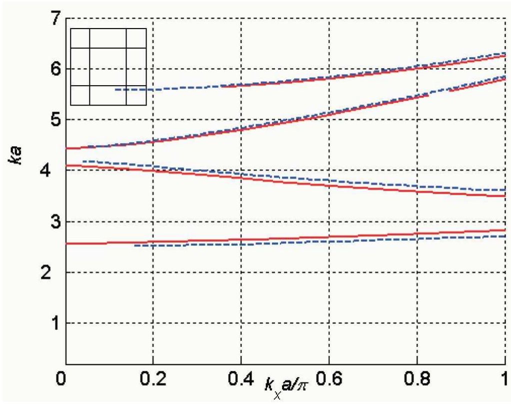

Figure 4.14: Non-connected geometry. Dashed curves – results obtained from formula 4, Solid curves – results of Green's function method.

Fig. 4.14. We observe again a very good agreement between the EM approach and the numerical results. In this case the backward wave also belongs to the second pass band but its cutoff wavenumber shifts to higher frequency, thereby decreasing the gap between the second and the third pass bands, where the last one occupies practically the same frequency range. Dispersion diagrams for the non-connected and connected geometries, calculated using MoM [73], are presented in Fig. 4.15 and Fig. 4.16, respectively. The main difference with the non-connected case is the absence of the lowest forward wave. Dispersion of other modes only slightly differs from the ones for the non-connected geometry.

Then, let us consider three wires in cross-section, as shown in the inset in Fig. 4.17. Here $\psi_x = \psi_y = \pi/3$ and $a = 3d$. In this case we observe quite a large shift of the first pass band to lower frequencies. However, positions of other modes are not changed substantially. The spectrum of modes for the strip wires, calculated by MoM, looks very similar: see Fig. 4.18, excepting horizontal line, which corresponds to the cutoff of the TE_{10} mode. The waveguide structure with connected wires has no low-order forward-mode as in previous cases, see Fig. 4.19.

To conclude this section, we showed that the conventional plasma model, used in Fig. 4.18, is not applicable for the analysis of a waveguide

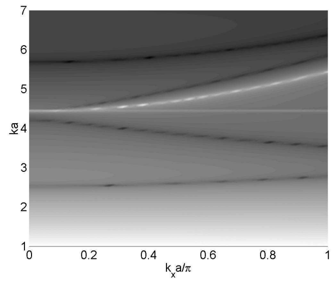

Figure 4.15: Non-connected geometry. Map of the determinant of the MoM impedance matrix.

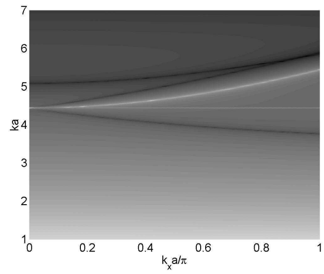

Figure 4.16: Connected geometry. Map of the determinant of the MoM impedance matrix.

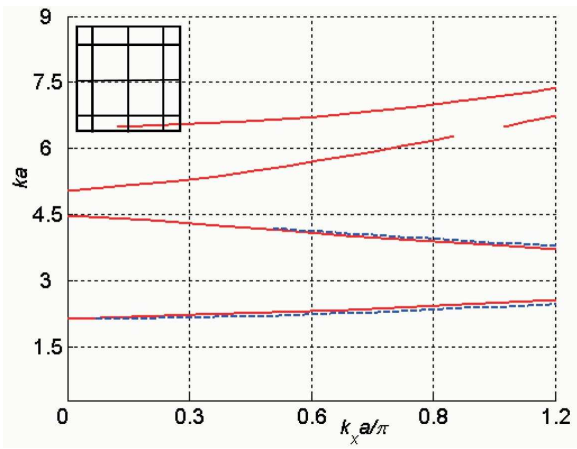

Figure 4.17: Non-connected geometry. Dashed curves – results obtained from formula 4, Solid curves – results of Green's function method.

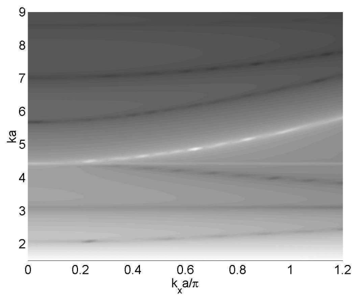

Figure 4.18: Non-connected geometry. Map of the determinant of the MoM impedance matrix.

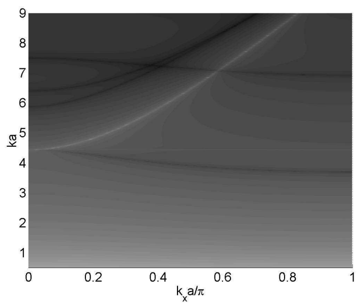

Figure 4.19: Connected geometry. Map of the determinant of the MoM impedance matrix.

filled with crossed wires both for geometries with connected and non-connected wires. The corrected effective medium model, which takes into account spatial dispersion, gives a good agreement with the full-wave models both for geometries with non-connected and connected wires. Both analytical and numerical models predict the propagation of backward waves in the waveguide. Only one essential difference between connected and non-connected geometries is observed. Namely, the spectrum of modes for non-connected geometry contains an extra forward mode, which is the lowest mode in the waveguide, filled with WM. Striking is the fact that this mode propagates even below cutoff of the dominant mode TE_{10}. This opens new perspectives in the miniaturization of waveguide based antennas. It was also demonstrated, that waveguide structures, containing more wires in cross-section, have similar spectra of modes but their pass band can be substantially shifted compared with the case of two perpendicular wires in a cross-section.

4.5 Conclusion

This chapter described how the MoM simulation code can be used to compute the dispersion curves of periodic structures:

- Computation of eigenmodes.

- Efficient computation of the Green's function periodic in three directions.
- Validations: Computation of the dispersion relations of single and double wire media.
- Application: Demonstration of wave propagation below cut-off in a waveguide filled with a double wire medium.

Application to the design of high gain antennas

5

This chapter describes how the MoM code and associated techniques presented in this work, as well as the structures studied, can be used in the design of high gain antennas. This will be demonstrated on two different examples. We first show that a metallic EBG structure made of parallel conducting wires can be used as a low refractive index metamaterial to increase the gain of a short dipole antenna. Then, the second example consists of a frequency selective surfaces (FSS) used as a superstrate to increase the gain of a slotted waveguide.

5.1 Low equivalent permittivity metamaterials

It has been shown in [74] that a structure made of stacked metallic grids of parallel conducting wires can focus energy in a narrow radiation pattern. This conclusion came from a semi-analytical study of a structure infinite in both x and y directions (Fig. 5.1) and an experimental verification in a real finite case. The structure studied here is made of a stack of 12 metallic grids infinite along both x and y directions. The grids are made of flat metallic strips. Fig. 5.2 shows the transmission coefficient of a plane wave polarized along y, at normal incidence. We clearly notice two frequency gaps; the lower one corresponds to wavelengths greater than about 4 times the periodicity of the structure. It is shown in [74] and [76] that near the band edges, this structure behaves as a homogeneous medium with a very low refractive index. Hence, under

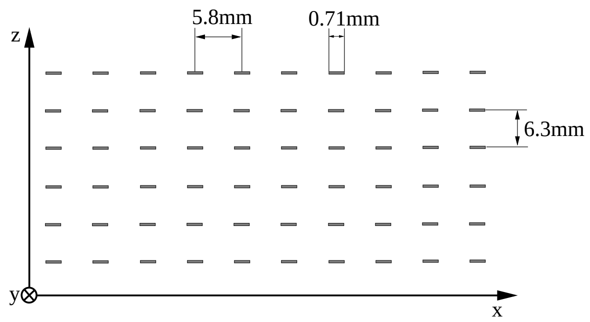

Figure 5.1: Structure of the metamaterial.

proper conditions, the energy radiated by a source embedded inside the metamaterial should be concentrated in a narrow emission lobe. This can be understood if we notice that the band edge is moving with the angle of incidence (Fig. 5.3). Indeed, a plane wave with a wavelength close to the band edge is transmitted at normal incidence but is totally reflected for higher incidences. This illustrates that, near the band edge (i.e. near 14 GHz in the present example), this metamaterial effectively behaves as a medium with a very low refractive index. This fact was also demonstrated by looking at the dispersion curves of this structure in section 4.2.2. Using our code, these simulations can be performed over the whole frequency band (150 frequency points) within a couple of minutes on a 2.5 GHz desktop computer.

5.1.1 Finite array case

In this case, we simulated a very short dipole embedded in a stack of 6 grids over a ground plane in several different finite-array configurations. The frequency is equal to 14.02 GHz, i.e. near the band edge. Fig. 5.1.1 shows the radiation patterns in 3 different conditions. When comparing these patterns we notice, as expected, that the directivity in the H plane is mainly influenced by the number of strips along x, while directivity in the E plane (along the strips) depends on the length of the strips along y.

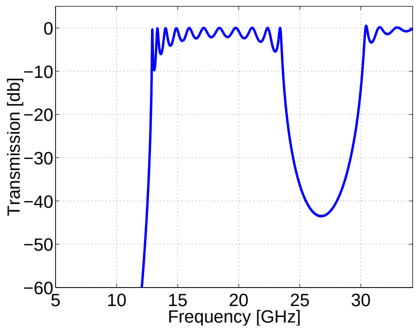

Figure 5.2: Transmission of a plane wave trough the structure shown in Fig. 5.1 with 12 layers at normal incidence.

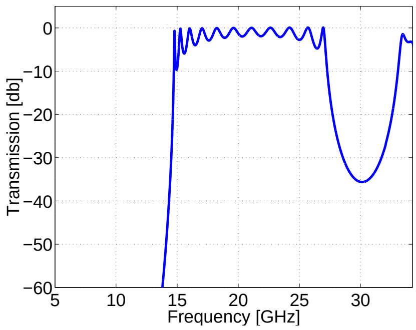

Figure 5.3: Transmission of a plane wave trough the structure shown in Fig. 5.1 with 12 layers at 30° incidence from broadside.

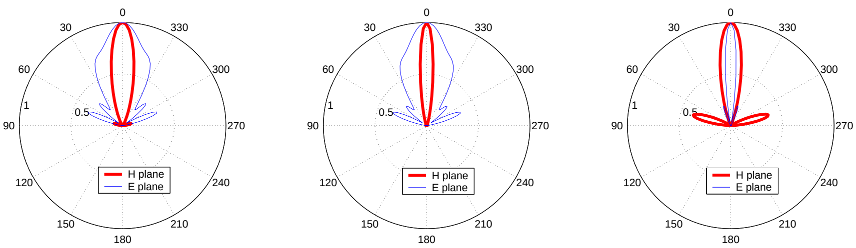

Figure 5.4: Left: 6×11 wires, length=1.3λ ; Center: 6×30 wires, length=1.3λ ; Right: 6×11 wires, length=4.6λ

5.2 FSS superstrate excited by a slotted cavity

In this section, it is shown how a metamaterial superstrate made of periodic frequency selective surfaces (FSS) can be used to increase the gain of a slotted waveguide or cavity. There are several reasons to explain the fact that we chose a slotted waveguide as the feeding structure. First, the whole structure can be entirely metallic, which can be mandatory in some applications. Then, such a waveguide exhibits many parameters that can be used to optimize the input impedance (cf. section 2.3.2): dimensions of the guide itself, size and position of the slot(s), size and position of the feed probe etc. Finally, as it will be shown in this section, the waveguide and the superstrate can be optimized separately, which greatly simplifies the design process. Numerical simulations of antennas based on periodic metamaterials fed by a slotted waveguide can be excessively time consuming because of the large number of unknowns involved in such structures. This Section describes how the analysis of the metamaterial can be carried out separately from the waveguide by defining interior and exterior equivalent problems. Moreover, we will show how the combination of both equivalent problems allows a fast computation of the antenna impedance properties.

5.2.1 The structure

It is now well known that periodic metamaterials can be used as antenna superstrates to collimate energy in a narrow lobe. For instance, it is shown in Section 5.1 how periodic metallic grids can behave as an ultrarefractive metamaterial to enhance the gain of monopole and dipole antennas. Another approach which consists of using frequency selective surfaces (FSS), made of short dipole arrays, to increase the directivity of a patch antenna is described in [79]. FSS superstrates can also be used in conjunction with metamaterial ground planes (Section 3.4.2 and [80]), that exhibit zero degrees reflection phase, to reduce antenna profile. Metamaterials can then also be used, for example, to increase the directivity of a slotted cavity. For instance, in Fig. 5.5, a superstrate

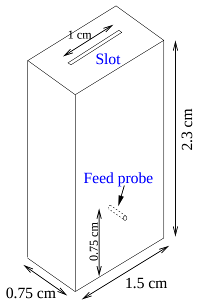

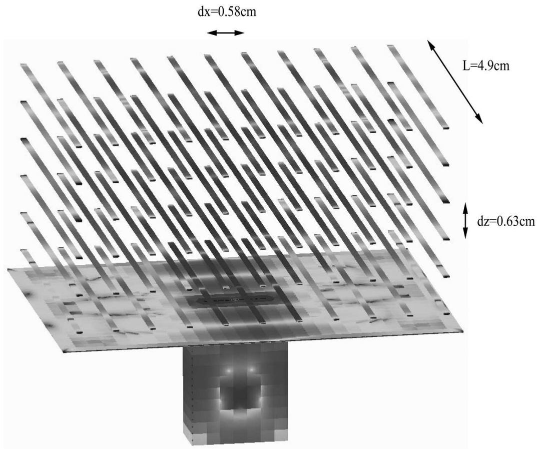

Figure 5.5: Slotted waveguide exciting a periodic metamaterial superstrate made of 6 layers of metallic strips. Left: description of the guide; Right: current distribution on the whole structure at 14 GHz.

made of six layers of metallic strips is used. The strips are 4.9 cm long and the spacings between them are 0.58 cm horizontally and 0.63 cm vertically. Fig. 5.6 shows the radiation pattern obtained at 14GHz. However, brute force simulations of such structures require a large computing power, because of the large number of unknowns, especially in the feeding structure. Another and more efficient approach consists of analyzing separately the waveguide and the metamaterial. A similar separation of the problem into two regions, an internal and an external one, was already used and validated in [81] for the analysis of slotted waveguide arrays. The method proposed here is based on the use of our MoM simulation code and the separate analysis of equivalent interior and exterior problems. Section 5.2.2 defines these interior and exterior equivalent problems and validate this approach on simple examples. It is then shown in Section 5.2.3 how both interior and exterior problems can be combined to obtain easily the impedance properties of the antenna.

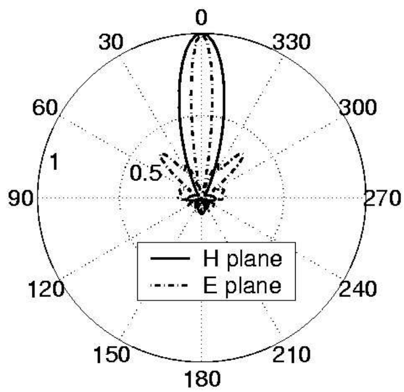

Figure 5.6: Radiation pattern of the structure in Fig. 5.5 at 14GHz.

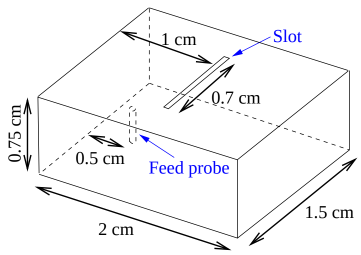

Figure 5.7: Description of the slotted cavity.

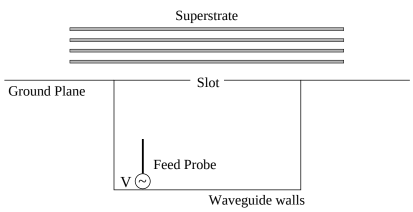

Figure 5.8: Schematic view of the whole structure studied.

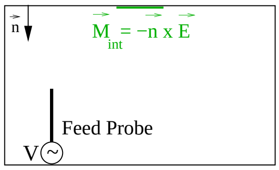

Figure 5.9: Interior equivalent problem.

5.2.2 Interior and exterior problems

The structure under study is illustrated in Figs. 5.7 and 5.8. It consists of a slotted waveguide or cavity, whose top wall is extended into a ground plane. A slot is cut in this top wall and the cavity is excited by some sort of feed probe. The interior problem, depicted in Fig. 5.9, can then be seen as a closed waveguide (the slot is short-circuited) with two different excitations. The first excitation is the voltage source V at the feed probe, modeled as a delta-gap, and the second one comes from magnetic currents $\vec{M} = -\vec{n} \times \vec{E}$ equivalent to fields in the slot. By exciting only the TE_{10} mode in the waveguide, one can assume that $\vec{M}_{int}$ and $\vec{H}_{int}$, respectively the magnetic currents and H field in the slot for the interior problem both have a sinusoidal distribution along the slot. Hence, by simulating this structure, and by using the superposition principle, it is possible to find on one side the ratio Y_{int}^{HM} of the amplitudes H_{int} and M_{int} when the probe is not excited ($V = 0$) and on the other side, the ratio Y^{HV} of the amplitudes H_{int} and V (the voltage source), when there is no magnetic current ($M = 0$). This yields for the interior H field amplitude:

$$H_{int} = Y^{HV} V + Y_{int}^{HM} M_{int} \tag{5.1}$$

Then, the exterior problem consists of a periodic metamaterial superstrate excited by a slot cut in the ground plane extending the top wall of the waveguide. Assuming that this ground plane is large enough, the problem can be seen as a periodic structure excited by magnetic currents $\vec{M} = -\vec{n} \times \vec{E}$, equivalent to fields in the slot, and flowing on an infinite ground plane, as shown in Fig. 5.10. This structure can also be simulated, and using the same assumption of sinusoidal field distribution as

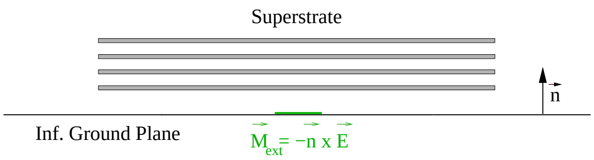

Figure 5.10: Exterior equivalent problem.

in the interior problem, we now have for the H field amplitude in the exterior problem.

$$H_{ext} = Y^{HM}_{ext} M_{ext} \tag{5.2}$$

5.2.3 Combining both problems

By enforcing the continuity of tangential fields along the slot, i.e. $H_{int} = H_{ext}$ and $M_{int} = -M_{ext}$, one can find the amplitude of equivalent magnetic currents using equations (5.1) and (5.2).

$$M_{ext} = -M_{int} = \frac{Y^{HV}V}{Y^{HM}_{int} + Y^{HM}_{ext}} \tag{5.3}$$

Then, using again the superposition principle in the interior problem, one can obtain the relations binding I (amplitude of the current induced on the feed probe) with both V (amplitude of the voltage excitation at the probe level) and M_{int} (amplitude of magnetic currents along the slot).

$$I = Y^{IV}V + Y^{IM}M_{int} \tag{5.4}$$

Then introducing (5.3) into (5.4), the current along the feed probe is obtained and the input impedance of the antenna, V/I at the proble level, can be determined.

$$Z = \frac{V}{I} = \frac{1}{Y^{IV} - \frac{Y^{IM}Y^{HV}}{Y^{HM}_{int}+Y^{HM}_{ext}}} \tag{5.5}$$

With this method, the radiation pattern can be optimized in the exterior problem by tuning the properties of the superstrate. Then, under the

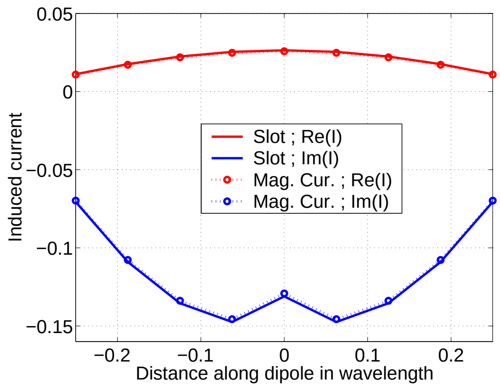

Figure 5.11: Comparison of current induced on a half-wave dipole in a slotted cavity. Solid lines: Slot open, Dotted lines: Slot is short-circuited and replaced by a sheet of magnetic currents, with a sinusoidal distribution.

single-mode approximation for fields in the slot, Eq. (5.5) will allow the determination of the impedance at the waveguide feed level. This input impedance can be optimized by tuning the waveguide parameters in the interior problem. The procedure that consists of replacing the electric field along the slot by magnetic currents with a sinusoidal distribution has been validated on three simple examples. In the first one, a small metallic box containing a half-wave dipole and with a slot cut in its top wall was simulated. Fig. 5.11 shows the current induced on the dipole (solid lines) when it is excited by a delta-gap. Then the slot was short-circuited and replaced by a sheet of magnetic currents with a sinusoidal distribution. The current induced on the dipole is also shown in figure 5.11 (dotted lines) and is almost exactly the same as in the previous case. The second example consists of a metallic cavity fed by a probe and also with a slot cut on its top broad wall. Its cross-section is 1.5 cm X 0.75 cm and its length is 2 cm. A 1 cm long slot is cut in the top wall. The input impedance at the probe level around the resonant frequency of the cavity is shown in Fig. 5.12. Solid lines show the impedance with the slot open and the small bullets and squares when the slot is short-circuited and replaced by a magnetic current sheet. Again the agreement

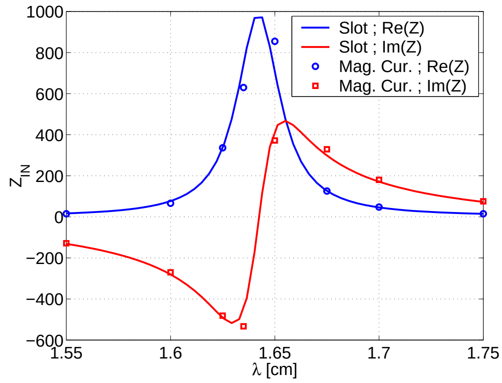

Figure 5.12: Comparison of the input impedance of a slotted cavity (1.5 cm × 0.75 cm × 2 cm). Solid lines: Slot open, Bullets and Squares: Slot is short-circuited and replaced by a sheet of magnetic currents.

is excellent. Finally, the third example is the simulation of a FSS made of two layers of 41×11 dipoles each and described in [79]. In a first instance, the transmission of a plane wave through this structure was computed and is shown in Fig. 5.13. One can note that there is a full transmission peak at 12.5 GHz. Then the FSS was placed above an infinite ground plane and excited by magnetic currents. The radiation pattern obtained at 12.5GHz is shown in Fig. 5.14. As mentioned in [79], we indeed obtain a high directivity. Finally, the optimization method described above was validated by full wave simulations of the complete structure made of the slotted cavity whose top wall is extended into a finite ground plane, above which the FSS was placed. The current distribution at 12.5 GHz is shown in Fig. 5.15 and the radiation pattern in Fig. 5.16. The achieved gain is about 22dB and corresponds to the directivity obtained in [79] by full-wave FDTD simulations. The difference between radiation patterns of Figs. 5.14 and 5.16 could be expected: the finite size of the ground plane allows a little back radiation, the side lobes are a little higher and the directivity is a little lower. The return loss obtained at the feed probe level is shown in Fig. 5.17. The achieved impedance bandwidth is about 6%, while the gain bandwidth (Gain>20dB) is about 2%.

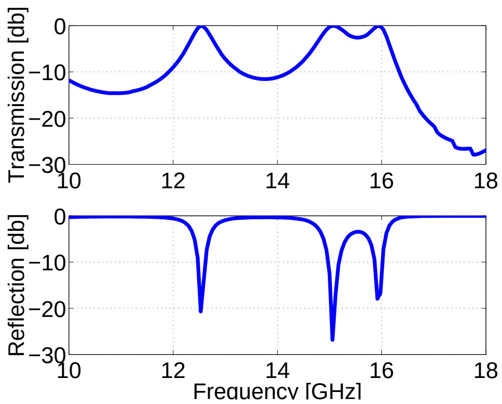

Figure 5.13: Transmission properties of a FSS described in [79] made of two layers of 41×11 dipoles.

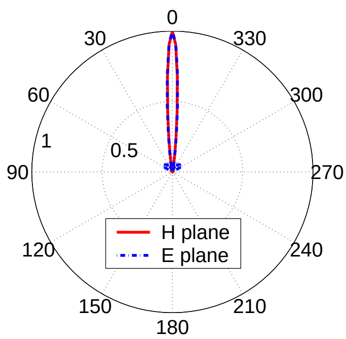

Figure 5.14: Radiation pattern at 12.5 GHz of a FSS described in [79] made of two layers of 41×11 dipoles and excited by magnetic currents on an infinite ground plane.

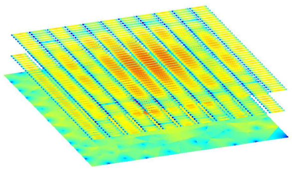

Figure 5.15: Current distribution at 12.5 GHz of the whole radiating structure made of a slotted cavity exciting the FSS superstrate. The size of the whole structure is 11 cm × 11 cm × 3.5 cm.

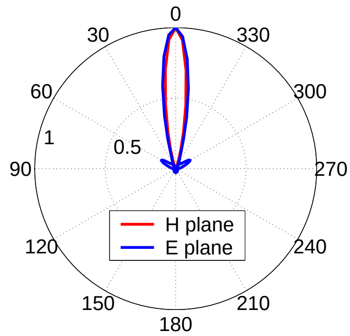

Figure 5.16: Radiation pattern at 12.5 GHz of the structure shown in Fig. 5.15.

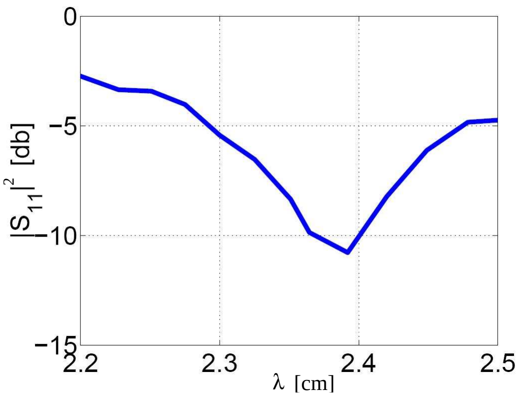

Figure 5.17: Return loss for the structure shown in Fig. 5.15.

5.3 Conclusion

This chapter described how all the tools and techniques presented in previous chapters can be used for the design of high-gain antennas based on a slotted waveguide or cavity exciting a periodic metamaterial superstrate:

- Separate analysis of the waveguide and the periodic superstrate.
- Combination of interior and exterior problems under the single-mode approximation for fields in the slot.
- Radiation pattern optimization: Infinite array simulations of the exterior problem
- Optimization of the input impedance in the interior problem

Conclusions

6

6.1 The MoM simulation code

One of the goals of this work was to develop efficient numerical tools for the analysis of large periodic structures such as metamaterials. Because of the large number of unknowns involved in these structures, brute-force simulation can be excessively time-consuming. A solution to overcome this problem is the infinite-array approximation. Indeed, this approximation reduces the unknowns of the problem to a single unit cell and dramatically reduces the computation time. That is why we developed an efficient implementation of the Method of Moments for the simulation of finite and infinitely periodic structures. This code is able to deal with metallic objects (EFIE formulation), dielectric objects (PMCHWT formulation) or mixed structures. It is based on the surface equivalence principle, hence, only surfaces need to be discretized, i.e. metallic surfaces or interfaces between homogeneous dielectric objects. This is a big advantage over other methods such as the FDTD, where the whole volume surrounding the structures under study needs to be meshed.
In infinite-array simulations, the periodicity is accounted for by resorting to the periodic Green's function. Three different formulations for the computation of this function were proposed and are used in conjunction, depending on the position of the observation point relative to the array plane. This always ensures the faster possible convergence. Moreover, to further reduce simulation time, this function is tabulated and a sec-

ond order interpolation technique is used during the filling of the MoM impedance matrix. In order to obtain the greatest possible accuracy, the singularity is extracted before the tabulation and the interpolation is then carried out on a very smooth function. The singularity is then reintroduced after interpolation, or it is treated separately for close interactions, ensuring a good accuracy of the numerical integration while keeping a reasonable number of integrand samples. It is worth noticing that our efficient formulations for the computation of the Green's function and its gradient allows a very easy extraction of the singularity. Actually, it can be extracted from the periodic Green's function in exactly the same way as in the case of an isolated object.

The code has been validated on numerous examples. Among these examples, we showed the simulation of the input impedance of a multi-band fractal antenna, the comparison of the input impedance of slotted waveguides computed by full-wave simulations and with analytical models, the demonstration of the constant input impedance of self-complementary arrays, and finally, the transmission/reflection properties of EBG structures, while artificial magnetic conductors were compared with results found in the literature. We also developed a simple model for ohmic losses in metallic structures which was validated through the verification of energy conservation in the case of an infinite TEM horn array. Finally, the simulation of infinite-array of dielectric objects was validated by verifying energy conservation in the case of infinite-array of dielectric spheres, with several values of the permittivity, illuminated by a plane wave.

6.2 Design methods and tools

Besides the simulation code, we also developed efficient design methods for large periodic structures such as large phased arrays or metamaterial based high gain antennas.

First, when considering metamaterials to improve the performance of antennas (impedance, gain, sidelobe level,...), one needs to be able to study periodic structures with a non-periodic excitation. However, when using the periodic Green's function to simulate infinitely periodic structures, the excitation is periodized in the same way as the unit cell of the metamaterial. This problem could be solved by resorting to the Array Scanning Method. By combining N^2 infinite-array simulations with every cell excited, this method multiplies by N the excitation period in both directions. It was demonstrated that, when N is large enough, the portion of the structure surrounding an excited cell behaves effectively as if there were only one cell excited. We extended this method to 3D structures and proposed a convergence criterion based on the infinite-array radiation pattern to determine how large N has to be.

We have also investigated several ways of estimating the effects of the truncation of infinitely periodic structures. Indeed, in large but finite periodic structures, the elements along the edges of the array are in a completely different electromagnetic environment, compared to the element further inside the structure. Hence, the behavior of the inner elements can be estimated with a very good accuracy with the infinite-array approximation. However, elements along the edges or in corners can behave very differently. A first step towards the estimation of the effects of truncation may be to consider finite-by-infinite arrays. Indeed, by combining an infinite-array simulation with two finite-by-infinite array simulations with different finite array directions, it is possible to obtain an accurate estimation of the effects of truncation. Finite-by-infinite array simulations are carried out using the Green's function periodic in one direction and leads to a Block-Toeplitz structure of the MoM impedance matrix. Using an iterative solver (Bi-CGstab) with a proper pre-conditionner, the system of equations can be solved very efficiently.
Another approach to estimate the effect of truncation consists of combining finite-by-infinite array simulations with the Array Scanning Method and a windowing technique. By comparing results obtained with this technique with those obtained by brute-force simulation of finite structures, we demonstrated that this method allows to accurately compute

the element pattern of any element of a finite array, provided that couplings are not excessively strong in both directions and generate strong surface waves.

We finally also proposed an elegant way of computing numerically the dispersion curves of periodic structures. These curves may be very important in the analysis of metamaterials as they contain a lot of informations about their properties. They can indeed inform us about the positions of stop and pass-bands, the directions in which modes can propagate as well as their phase velocity. We showed that these dispersion curves can be computed by searching for the nulls of the determinant of the MoM impedance matrix associated to the periodic structure. For the analysis of metamaterials periodic in the three directions of space, we developed an expression for the three-fold periodic Green's function, which can be evaluated with the same computational complexity as the doubly periodic Green's function.
The chosen approach was validated by comparing the dispersion curves obtained numerically for an infinite empty waveguide with those obtained analytically. Other validations were carried out on single and double wire media, for which the numerical results were also compared to analytical models found in the literature.
Surprising results obtained when studying waveguides filled with such wire media are then presented. In this study, we could show that backward waves can propagate in such waveguides. Moreover, we could also demonstrate the propagation of forward waves below the cut-off frequency of the fundamental mode. These results were again compared with analytical models.

6.3 Design of high gain antennas

The last chapter of this thesis focuses on the application of all the previously mentioned techniques to the design of high gain antennas based on metamaterials. Two examples are presented. The first one consists of a wire medium that exhibits a low dielectric permittivity, and hence, a low refraction index. According to Snell's law, the waves radiated by a source embedded in such a medium are refracted very close to the normal with the interface. This fact has been confirmed by simulation of a small dipole put in the middle of this wire medium. The second example describes how a superstrate made of frequency selective surfaces can be used to increase the gain of a slotted waveguide. Moreover, an efficient technique for the design of such slotted waveguide antennas is proposed and validated. This technique consists of separating the whole structure into and interior problem (interior of the waveguide) and an exterior one (the periodic superstrate) and then enforcing the continuity of tangential fields along the slots. In both problems, the slot was short-circuited and the electric field was replaced by equivalent magnetic currents with a sinusoidal distribution. We showed that the superstrate can be analyzed alone to optimize the radiation pattern, while the input impedance of the waveguide can be optimized by tuning parameters of the interior problem. We would like to stress that the input impedance of high-gain metamaterial antennas is almost never analyzed. The efficiency of this design method was demonstrated on an example in which we could achieve a gain of 22dB with a return loss of -10dB.

6.4 Further prospects

The technique presented above for the design of slotted waveguide antennas with a metamaterial superstrate is currently being extended to more than one feeding slot. For instance, one can study two separate slotted cavities exciting the metamaterial with almost no increase in simulation complexity. This opens new perspectives in the fast analysis of arrays of slots, dual-polarization as well as dual-band high gain antennas. Moreover, we demonstrated that, when waveguides are filled with wire media, waves can propagate below the cut-off frequency. This is very promising in terms of miniaturization of these slotted waveguide antennas.

An ASM-based method to compute the effect of truncation of the periodic superstrate and its impact on the aperture efficiency of the structure is also under study.

Thanks to the finite-by-infinite array approach, our code can also be very useful in the design of wideband antenna arrays, and in the analysis of the effects of truncation in such arrays with electrically connected, and hence, strongly coupled elements [62].

Finally, work is currently carried out towards the fast analysis of finite arrays with the help of Macro Basis Functions (MBF). Recently fast methods have been described where the interactions between macro basis and macro testing functions are computed with the help of a multipole approach [82]. Extensions of these methods, where physically based MBF's can be obtained with the Array Scanning Method are under study and seem to be very promising.

List of acronyms

A

AMC: Artificial Magnetic Conductor

ASM: Array Scanning Method

Bi-CGstab: Bi-Conjugate Gradient stabilized

BW: Backward-Waves materials

DFT: Discrete Fourier Transform

DNG: Double Negative media

DWM: Double Wire Medium

EBG: Electromagnetic Band-Gap

EFIE: Electric Field Integral Equation

EM: Effective Medium

EMC: Electromagnetic Compatibility

FD: Finite Difference method

FDTD: Finite Difference Time Domain method

FEM: Finite Element Method

FSS: Frequency Selective Surface

MBF: Macro Basis Function

MoM: Method of Moments

NIM: Negative-Index Materials

LHM: Left-Handed Material

PBG: Photonic Band-Gap

PEC: Perfect Electric Conductor

PMC: Perfect Magnetic Conductor

PRS: Partially Reflective Surface

PMCHWT: Poggio-Miller-Chang-Harrington-Wu-Tsai formulation

RWG: Rao-Wilton-Glisson

SRR: Split Ring Resonator

TE: Transverse Electric

TEM: Transverse Electromagnetic

TL: Transmission Line

TM: Transverse Magnetic

TLM: Transmission Line Matrix method

VSWR: Voltage Standing Wave Ratio

WM: Wire Medium

Computation of the MoM matrix elements

B

Using Eq. 2.59, one can see that the MoM impedance matrix elements can be computed as follows:

$$\begin{aligned} Z_{mn} &= \frac{1}{j\omega\epsilon}\int_S \vec{J}_m \cdot (k^2\overline{\overline{I}} + \nabla\nabla\cdot)\int_{S'} \vec{J}_n G(R)\, dS' dS \\ &= \frac{1}{j\omega\epsilon}(I_1 + I_2) \end{aligned}$$

Where we defined I_1 and I_2 as

$$\begin{aligned} I_1 &= k^2 \int_S \vec{J}_m \cdot \int_{S'} \vec{J}_n G(R)\, dS' dS \\ I_2 &= \int_S \vec{J}_m \cdot \nabla\nabla \cdot \int_{S'} \vec{J}_n G(R)\, dS' dS \end{aligned}$$

Let

$$\phi_1 = \int_{S'} \nabla_S \cdot \left[\vec{J}_n G(R)\right] dS'$$

Where ∇_S is a surface divergence.
Hence, I_2 can be rewritten as:

$$\begin{aligned} I_2 &= \int_S \vec{J}_m \cdot \nabla\phi_1 dS \\ &= \int_S \nabla \cdot (\vec{J}_m \phi_1) dS - \int_S \phi_1 \nabla \cdot \vec{J}_m dS \end{aligned} \tag{B.1}$$

but from the divergence theorem:

$$\int_S \nabla \cdot (\vec{J}_m \phi_1) dS = \int_{\partial S} \phi_1 \vec{J}_m \cdot \hat{n}\, dl = 0$$

Where $\hat{n}$ is the outward pointing unit normal of the boundary ∂S. This integral is null because the current $vecJ_m$ has no component normal to the edges of the basis function. Hence

$$I_2 = -\int_S \phi 1 \nabla \cdot \vec{J}_m dS$$

and ϕ_1 can be rewritten as follows:

$$\begin{aligned}
\phi_1 &= \int_{S'} \nabla_S \left[\vec{J}_n G(R) \right] dS' \\
&= \int_{S'} \vec{J}_n \cdot \nabla_S \left[G(R) \right] dS' \\
&= -\int_{S'} \vec{J}_n \cdot \nabla_{S'} \left[G(R) \right] dS' \\
&= -\int_{S'} \nabla_{S'} \left[\vec{J}_n G(R) \right] dS' + \int_{S'} G(R) \nabla_{S'} \cdot \vec{J}_n dS'
\end{aligned}$$

From the divergence theorem, and using the fact that the current has no component normal to the edges of the basis functions, the first integral of the right member is always null:

$$\int_{S'} \nabla_{S'} \left(\vec{J}_n G(R) \right) dS' = \int_{\partial S'} G(R) \vec{J}_n \cdot \hat{n} \, dl = 0$$

so the integral I_2 finally writes

$$I_2 = -\int_S \int_{S'} (\nabla \cdot \vec{J}_m)(\nabla \cdot \vec{J}_n) G(R) dS' dS$$

and the impedance matrix elements finally writes:

$$Z_{mn} = \frac{1}{j\omega\epsilon} \left[\int_S \int_{S'} \left(k^2 \vec{J}_m \cdot \vec{J}_n - (\nabla \cdot \vec{J}_m)(\nabla \cdot \vec{J}_n) \right) G(R) dS' dS \right] \quad \text{(B.2)}$$

Proof of expression 2.39

C

$$\frac{1}{j\omega\epsilon}\nabla\nabla\cdot\int_{S'} G(\hat{n}\times\vec{H})dS' = \frac{1}{j\omega\epsilon}\nabla\int_{S'}\nabla\cdot\left[G(\hat{n}\times\vec{H})\right]dS'$$
$$= \frac{1}{j\omega\epsilon}\nabla\left[\int_{S'}(\nabla G)\cdot(\hat{n}\times\vec{H})\,dS' - \int_{S'} G\nabla\cdot(\hat{n}\times\vec{H})\,dS'\right]$$
$$= \frac{-1}{j\omega\epsilon}\nabla\left[\int_{S'}(\nabla' G)\cdot(\hat{n}\times\vec{H})\,dS'\right]$$
$$= \frac{-1}{j\omega\epsilon}\nabla\int_{S'}\left[\nabla'\cdot\left[G(\hat{n}\times\vec{H})\right] - G\nabla'\cdot(\hat{n}\times\vec{H})\right]dS' = (1)+(2) \quad \text{(C.1)}$$

$$(1) = \frac{-1}{j\omega\epsilon}\nabla\int_{S'}\nabla'\left[G(\hat{n}\times\vec{H})\right]dS' = \frac{-1}{j\omega\epsilon}\nabla\int_{S'}\nabla'(\hat{n}\times G\vec{H})dS'$$
$$= \frac{-1}{j\omega\epsilon}\nabla\int_{S'}\left[G\vec{H}\cdot\nabla'\times\hat{n} - \hat{n}\cdot\nabla'\times(G\vec{H})\right]dS' \quad \text{(C.2)}$$

If S is closed, this can be rewritten:

$$= \frac{-1}{j\omega\epsilon}\nabla\int_{S'} G\vec{H}\cdot\nabla'\times\hat{n}\,dS' + \frac{1}{j\omega\epsilon}\nabla\int_{V}\nabla\cdot\nabla\times(G\vec{H})\,dS'$$
$$= \frac{-1}{j\omega\epsilon}\nabla\int_{S'} G\vec{H}\cdot\nabla'\times\hat{n}\,dS' \quad \text{(C.3)}$$

Then,

$$(2) = \frac{1}{j\omega\epsilon}\nabla\int_{S'} G\vec{H}(\hat{n}\times\vec{H})\,dS' = \frac{1}{j\omega\epsilon}\nabla\int_{S'} G\left[\vec{H}\cdot\nabla'\times\hat{n} - \hat{n}\cdot\nabla'\times\vec{H}\right]dS' \quad \text{(C.4)}$$

If $\vec{J} = 0$ on S, this can be rewritten:

$$\frac{1}{j\omega\epsilon}\nabla \int_{S'} G\big[\vec{H} \cdot \nabla' \times \hat{n} - \hat{n} \cdot j\omega\epsilon\vec{E}\big] dS' \tag{C.5}$$

And finally:

$$\begin{aligned}(1) + (2) &= -\nabla \int_{S'} G(\hat{n} \cdot \vec{E}) dS' = -\int_{S'} \nabla\big[G(\hat{n} \cdot \vec{E})\big] dS' \\ &= -\int_{S'} \nabla(\nabla G)(\hat{n} \cdot \vec{E})\, dS' \\ &\int_{S'} (\nabla' G)(\hat{n} \cdot \vec{E})\, dS' \end{aligned} \tag{C.6}$$

List of publications

D

D.1 Conference papers

- X. Dardenne and C. Craeye, "Simulation of the effects of a ground plane on the radiation characteristics of self-complementary arrays," *Proc. of the 2003 IEEE Antennas and Propagation Society Symposium,* Columbus, Ohio, June 2002.

- X. Dardenne and C. Craeye, "Simulation of the radiation characteristics of 3D quasi self-complementary arrays," *Proc. of COST284 workshop,* Budapest, April 2003.

- X. Dardenne and C. Craeye, "Analysis of infinite and finite low-profile broadband arrays," *Proc. of the 26th ESA Antenna Technology Workshop on Satellite antenna modeling and design tools,* Noordwijk, Nov. 2003

- X. Dardenne and C. Craeye, "Numerical Study of low-profile directive antennas based on metamaterials," *Proc. of the 2004 Student Seminar,* St-Petersburg, June 2004.

- X. Dardenne and C. Craeye, "ASM Based Method for the Study of Periodic Metamaterials Excited by a Slotted Waveguide," *Proc. of the 2005 IEEE Antennas and Propagation Society Symposium,* Washington DC, July 2005.

- X. Dardenne and C. Craeye, "Application of the Array Scanning Method with Windowing to the Analysis of Finite Rectangular Periodic Structures," *Proc. of the 18th International Conference on Applied Electromagnetics and Communications,* Dubrovnik, Oct. 2005.

- X. Dardenne, I. Nefedov and C. Craeye, "Numerical analysis of effective wire length in wire media for image canalization with subwavelength resolution," *Proc. of the 2006 Loughborough Antennas & Propagation Conference*, 2006.

- X. Dardenne, C. Craeye and A.O. Boryssenko, "Design of high gain slotted waveguide antenna using metamaterials," *Proc. of First European Conference on Antennas and Propagation-EuCAP2006,* Nice, Nov. 2006.

- X. Dardenne, N. Guérin and C. Craeye, "Efficient MoM analysis of metamaterials involving dielectric structures," accepted for publication in *Proc. of the ACES 2007 Conference,* Verona, Italy, March 19-23, 2007

- I.S. Nefedov, X. Dardenne, C. Craeye and S.A. Tretyakov, "Backward waves in a waveguide, filled with wire media," *Proc. of the Third Workshop on Metamaterials and Special Materials for Electromagnetic Applications*, Rome, 2006

- Mateos R., Ferrer P., "Craeye C. and Dardenne X., Reactive fields above an artificial PMC," *Proc. of the 2005 IEEE Antennas and Propagation Society Symposium,* Washington DC, July 2005.

- Huynen Isabelle, Saib Aimad, Raskin Jean-Pierre, Dardenne Xavier, Craeye Christophe, "Periodic metamaterials combining ferromagnetic, dielectric and/or metallic structures for planar circuits applications", *Bianisotropics 2004 - 10th Conference on Complex Media and Metamaterials,* Het Pand, Ghent, Belgium, September 22-24, 2004, 212-219

- C. Craeye and X. Dardenne, "Efficient computation of the polarization characteristics of infinite and finite arrays of tapered-slot antennas," *Proc. of the 2003 IEEE Symposium on Phased Array Systems and Technology,* 2003

- C. Craeye W. Brisken and X. Dardenne, "Simulated radiation characteristics of wideband focal plane arrays and their impact on the system gain-to-temperature ratio," *Proc. of the JINA 2004 Conference,* Nice, Nov. 2004.

D.2 Journal papers

- C. Craeye, B. Parvais and X. Dardenne, "MoM Simulation on Signal-to-Noise Patterns in Infinite and Finite Receiving Antenna Arrays," *IEEE Trans. Antennas and Propagat.,* 12, pp.3245-3256, 2004

- Craeye C., Dardenne X., "Element pattern analysis of wideband arrays with the help of a finite-by-infinite array approach," *IEEE Trans. on Antennas and Propagat.* 54, pp.519-526, 2006

- I. Nefedov, X. Dardenne and C. Craeye, Backward waves in a waveguide filled with wire media, accepted for publication in *Special Issue on Metamaterials of Microwaves Optical and Technology Letters,* April 2006.

Bibliography

[1] The www page of David Smith, University of California, San Diego. *http://physics.ucsd.edu/ drs/*

[2] Weiland, T., Schuhmann, R., Greegor, R.P., Parazzoli, C.G., Vetter, A.M., Smith, D.R., Vier, D.C., and Schultz, S. "Ab initio numerical simulation of left-handed metamaterials: Comparison of calculations and experiments," *J. of Applied Physics,* 90(10), 5419-5424, 2001.

[3] Pendry, J.B., "Negative μ, negative ϵ, negative refractive index, and how to exploit them. Electromagnetic Crystal Structures," *Euroconference on Electromagnetic Confinement, from Basic Research to the Marketplace,* St. Andrews, Scotland, 9-14 June 2001.

[4] Metamaterials home page of the future projects of the Defense Advanced Research Projects Agency's (DARPA) Defense Sciences Office (DSO). *http://www.darpa.mil/dso/thrust/matdev/metamaterials/metamaterials.html*

[5] Walser, R.M. (2001) "Electromagnetic metamaterials, Inaugural Lecture," *Proc. of SPIE (Complex Mediums II: Beyond Linear Isotropic Dielectrics)*, 4467, 1-15.

[6] V.G. Veselago, "The electrodynamics of substances with simultaneously negative values of ϵ and μ," *Soviet Physics Uspekhi,* Vol. 10, No. 4, January 1968

[7] J. Bonache, I. Gil, J. Garcia-Garca, and Ferran Martn, "Novel Microstrip Bandpass Filters Based on Complementary Split-Ring Resonators," *IEEE Trans. MTT.,* Vol. 54, No. 1, January 2006.

[8] C. Caloz, T. Itoh, "Electromagnetic Metamaterials: Transmission Line Theory and Microwave Applications," Wiley, 2006

[9] J. B. Pendry, "Negative Refraction Makes a Perfect Lens," *Phys. Rev. Lett.* 85, No. 18, October 2000

[10] R.W. Ziolkowski, A. Kipple, "Causality and double-negative metamaterials," *Phys. Rev. E,* 68, 026615, Aug. 2003.

[11] J. B. Pendry, A. J. Holden, W. J. Stewart and I. Youngs, "Extremely Low Frequency Plasmons in Metallic Mesostructures," *Phys. Rev. Letters,* Vol. 76, No. 25, pp. 4773-4776, 1996.

[12] B. Szentpali, "Metamaterials: a New Concept in the Microwave Technique," *Microwave review,* December 2003

[13] J. B. Pendry, A. J. Holden, D. J. Robbins and W. J. Stewart, "Magnetism from Conductors and Enhanced Nonliear Phenomena," *IEEE Trans. On Microwave Theory and Technique,* Vol. 47, No. 11, pp. 2075-2084, 1999.

[14] R. A. Shelby, D. R. Smith, S. Schultz, "Experimental Verification of a Negative Index of Refraction," *Science,* Vol. 292, pp. 77-79, 2001

[15] Sievenpiper, D. F., L. Zhang, R. F. J. Broas, N. G. Alexopolous and E. Yablonovitch, "High-impedance Electromagnetic Surfaces with a Forbidden Frequency Band," *IEEE Trans. MTT.,* Vol. 47, 2059-2074, Nov. 1999.

[16] R. W. Ziolkowski and A. D. Kipple, "Application of Double Negative Materials to Increase the Power Radiated by Electrically Small Antennas," *IEEE Trans. Ant. Propagat.,* Vol. 51, No. 10, October 2003

[17] J.C. Maxwell, "A Treatise on Electricity and Magnetism," *Clarendon Press,* Oxford, 1873.

[18] K. Yee, "Numerical solution of initial boundary value problems involving Maxwell's equation in isotropic media," *IEEE Trans. Ant. Propagat.,* Vol. 14, pp. 302-307, May 1966.

[19] A. Taflove, "Advances in Computational Electrodynamics: the Finite Difference Time Domain Method," *Boston, MA: Artech house,* 1998

[20] B. Engquist and A. Majda, "Absorbing boundary conditions for the numerical simulation of waves," *Math. Comput.,* iol. 31, pp. 629451, July 1977

[21] G. Mur, "Absorbing boundary conditions for the finite difference approximation of time-domain electromagneticfield equations," *IEEE Trans. Electromag. Compat.,* vol. EMC-23, pp. 377-382, Nov. 1981

[22] P.P. Silvester and G. Pelosi, "Finite Element Method for Wave Electromagnetics,"*New-York: IEEE Press.* ,1996.

[23] S. Akhtarzad, and P.B. Johns, "Three-Dimensional Transmission-Line Matrix Computer Analysis of Microstrip Resonators," *IEEE Trans. On Microwave Theory and Technique,* Vol. 23, No. 12, December 1975

[24] R.F. Harrington, "Time-Harmonic Electromagnetic Fields," *McGraw-Hill Book Company*, 1961

[25] Albert Guissard, "On the Surface Field Integral Equations," *IEEE Trans. on Education*, vol.46, No.3, August 2003

[26] Y Mushiake, "Self-Complementary Antennas," *IEEE Antennas and Propagation Maga- zine*, vol. 34, pp. 23-29, December 1992.

[27] A. K. Skrivervik, J.-F. Zurcher, O. Staub and J. R. Mosig, "PCS Antenna Design: The Challenge of miniaturization", *IEEE Antennas and Propagation Magazine*, vol. 43, pp. 12-27, August 2001.

[28] R.F. Harrington, "Field Computation by Moment Methods," *IEEE Press Series on Electromagnetic Wave Theory*, 1993.

[29] C. Geuzaine and J-F. Remacle, "Gmsh: a three-dimensional finite element mesh generator with built-in pre- and post-processing facilities," *http://geuz.org/gmsh/*

[30] S.M.Rao, D.R.Wilton and A.W.Glisson, "Electromagnetic scattering by surfaces of arbitrary shape", *IEEE Trans. Antennas Propagat.*, Vol.AP-30, pp. 409-418, May 1982

[31] R.E. Jorgenson and R. Mittra, "Efficient Calculation of the Free-Space Periodic Green's Function," *IEEE Trans. Antennas Propagat.*, Vol.AP-38, No. 5, pp. 633-642, May 1990

[32] D. A. Dunavant, "High degree efficient symmetrical Gaussian quadrature rules for the triangle," *Int. Journal Numer. Meth. Eng.*,1985, pp. 1129-1148.

[33] D.R. Wilton, S.M. Rao, A.W. Glisson, D.H. Schaubert, O.M. Al-Bundak and C.M. Butler, "Potential Integrals for Uniform and Linear Source Distributions on Polygonal and Polyhedral Domains," *IEEE Trans. Antennas Propagat.*, Vol. AP-32, No. 3, March 1984

[34] R.E. Hodges and Y. Rahmat-Samii, "The Evaluation of MFIE Integrals with the Use of Vector Triangle Basis Functions," *Microwave and Optical Technology letters*, Vol. 14, No. 1, January 1997

[35] C. Puente, J. Romeu, R. Pous, and A. Cardama, "On the behavior of the Sierpinski multiband antenna," *IEEE Trans. Antennas Propagat.*, Vol. 46, No. 4, pp. 517-524, April 1998

[36] N. Marcuvitz, "Waveguide Handbook," *MIT Radiation Laboratory Series,* Vol. 10, McGraw-Hill, New York, 1951

[37] A.Oliner, "The Impedance Properties of Narrow Radiating Slots in the Broad Face of Rectangular Waveguide, Part I - Theory," *IRE Trans. on Antennas and Propagation,* January 1957

[38] A.Oliner, "The Impedance Properties of Narrow Radiating Slots in the Broad Face of Rectangular Waveguide, Part II - Comparison with Measurement," *IRE Trans. on Antennas and Propagation,* January 1957

[39] A. Vander Vorst and D. Vanhoenacker-Janvier, "Bases de l'ingénierie micro-onde," De Boeck Université, 1996

[40] C. Craeye, A.B. Smolders, D.H. Schaubert and A.G. Tijhuis, "An Efficient Computation Scheme for the Free Space Greens Function of a Two-Dimensional Semiinfinite Phased Array,"*IEEE Trans. Antennas Propagat.*, Vol.AP-51, No. 4, pp. 766-771, April 2003

[41] S. Singh and R. Singh, "On the Use of Shankss Transform to Accelerate the Summation of Slowly Converging Series," *IEEE Trans. on Microwave Theory and Techniques,* Vol. 39, No. 3, March 1991

[42] C. Craeye and F. Capolino, "Accelerated Computation of the Free Space Greens Function of Semi-Infinite Phased Arrays of Dipoles," *IEEE Trans. Antennas Propagat.*, vol. 54, No. 3, pp. 1037-1040, March 2006.

[43] D. T. McGrath and C. E. Baum, "Scanning and Impedance Properties of TEM Horn Arrays for Transient Radiation," *IEEE Trans. Antennas Propagat.*, vol. 47, pp. 469-473, March 1999.

[44] A-C. Tarot, S. Collardey, and K. Mahdjoubi, "Numerical Studies of Metallic PBG Structures," *Progress in Electromagnetics Research,* PIER 41, 133-157, 2003

[45] Fan Yang, and Yahya Rahmat-Samii, "Reflection Phase Characterizations of the EBG Ground Plane for Low Profile Wire Antenna Applications," *IEEE Trans. Antennas Propagat.*, vol. 51, No. 10, Oct. 2003

[46] D. Smith, J. Pendry and M. Wiltshire, Science 305, 788 (2004)

[47] M. Wiltshire, J.B. Pendry, I. Young, D. Larkman, D. Gilderdale, and J. Hajnal, Science 291, 849 (2001)

[48] P. A. Belov, Y. Hao and Sunil Sudhakaran,"Sub-wavelength imaging by wire media," unpublished, http://arxiv.org/abs/cond-mat/0508696

[49] P.A. Belov, M.G. Silveirinha, "Resolution of sub-wavelength lenses formed by the wire medium," *http://www.arxiv.org/abs/physics/0511139*

[50] P.A. Belov, R. Marques, S.I. Maslovski, I.S. Nefedov, M. Silveirinha, C.R. Simovski, and S.A. Tretyakov, "Strong Spatial Dispersion in Wire media in the Very Large Wavelength Limit,"*Phys. Rev. B,* vol. 67, 113103 (2003).

[51] X. Dardenne and C. Craeye, "Applications of ASM and a windowing technique in the analysis of finite periodic structures," *Proc. of the 18th International Conference on Applied Electromagnetics, ICECom 2005*, Dubrovnik, October 2005.

[52] Y. Lee, J. Yeo, R. Mittra, and W. Park, "Application of Electromagnetic Bandgap (EBG) Superstrates With Controllable Defects for a Class of Patch Antennas as Spatial Angular Filters," *IEEE Trans. Antennas Propagation*, vol.53, no.1, pp.224–235, 2005.

[53] C. Kittel, "Introduction to Solid State Physics," *Wiley,* New York, 1996

[54] D.M. Pozar, "Microwave Engineering," *Addison Wesley,* 1990

[55] Craeye C., Parvais B., Dardenne X., "MoM Simulation of Signal-to-noise Patterns in Infinite and Finite Receiving Antenna Arrays," *IEEE Transactions on Antennas and Propagation*, vol. 52, pp. 3245-3256, Dec. 2004.

[56] A.F. Peterson, D.R. Wilton, and R.E. Jorgenson, "Variational Nature of Galerkin and Non-Galerkin Moment Method Solutions,"*IEEE Trans Antennas Propagat.* Vol. 44, No. 4, April 1996

[57] A. Roederer, "Etude des réseaux finis de guides rectangulaires à parois épaisses," *L'onde électrique*, vol. 51, Nov. 1971, 854-861

[58] B.A. Munk and G.A. Burrell, "Plane-wave expansion for arrays of arbitrarily oriented piecewise linear elements and its application in determining the impedance of a single linear antenna in a lossy half-space," *IEEE Trans Antennas Propagat.* AP-27 1979 ,331-343

[59] F. Capolino, D.R. Jackson, D.R. Wilton, "Fundamental Properties of the Field at the Interface Between Air and a Periodic Artificial Material Excited by a Line Source," *IEEE Trans Antennas Propagat.*, vol. 53, Jan. 2005

[60] C.R. Simovski and P.A. Belov, "On the low-frequency spatial dispersion in wire media," *Physical Review E*, vol. 70, 046616 (1-8), 2004.

[61] C. Craeye C., A.O. Boryssenko and D.H. Schaubert, "Computation of truncation effects in broadband tapered-slot phased arrays using efficient frequency-domain and time-domain approaches," *Proc. of the 12th IEE Int. Conf. on Antennas and Propagat.* ,pp. 445-448, Exeter, April 2003.

[62] C. Craeye and X. Dardenne, "Element Pattern Analysis of Wide-Band Arrays With the Help of a Finite-by-Infinite Array Approach," *IEEE Trans Antennas Propagat.*, vol. 54, No. 2, February 2006

[63] H.A. van der Vorst, "Bi-CGSTAB: A fast and smoothly converging variant of Bi-CG for the solution of nonsymmetric linear systems," *SIAM J. Scientific and Statistical Computing,* vol. 13, pp. 631-644, 1992.

[64] S. Tretyakov, *Analytical Modeling in Applied Electromagnetics* (Artech House. Boston-London, 2003).

[65] P.A. Belov, R. Marques, S.I. Maslovski, I.S. Nefedov, M. Silveirinha, C.R. Simovski, and S.A. Tretyakov, Strong Spatial Dispersion in Wire media in the Very Large Wavelength Limit, *Phys. Rev. B*, vol. 63, pp. 113103-1-113103-4, 2003.

[66] J. Esteban, C. Camacho-Penalosa, J.E. Page, T.M. Martin-Guerrero, and E. Marquez-Segura, Simulation of Negative Permittivity and Negative Permeability by Means of Evanescent Waveguide Modes – Theory and Experiment, *IEEE Trans. Microwave Theory Tech.*, vol. 53, no. 4, pp. 1506–.., April 2005.

[67] M.G. Silveirinha, and C.A. Fernandes, Homogenization of 3-D-Connected and Nonconnected Wire Metamaterials, *IEEE Trans. Microwave Theory Tech.* **53**, 1418 (2005).

[68] M.G. Silveirinha, and C.A. Fernandes, A Hybrid Method for the Efficient Calculation of the Band Structure of 3-D Metallic Crystals, *IEEE Trans. Microwave Theory Techn.,*, vol. 52, No. 3, pp. 889–902, 2004.

[69] I.S. Nefedov, A.J. Viitanen, S.A. Tretyakov, Propagating and Evanescent Modes in Two-Dimensional Wire Media, *Phys. Rev. E*, Vol. 71, 046612-1–10, 2005.

[70] J.B. Pendry, A.J. Holden, W.J. Stewart, and I. Youngs, Extremely LOw Frequency Plasmons in Metallic Mesostructures, *Phys. Rev. Lett.* **76**, pp. 4773–4776 (1996).

[71] Maslovski, S.I., Tretyakov, S.A. and Belov, P.A., Wire media with negative effective permittivity: a quasi-static model, *Microwave and Optical Technology Letters,* Vol. 35, No. 1, pp. 47-51, October 2002.

[72] P.A. Belov, S.A. Tretyakov, A.J. Viitanen, Dispersion and Reflection Properties of Artificial Media Formed by Regular Lattices of Ideally Conducting Wires, *Journal of Electrom. Waves and Applic.,* Vol. 16, No. 8, pp. 1153-1170, 2002.

[73] I. Huynen, A. Saib, J.P. Raskin, X. Dardenne and C. Craeye, "Periodic metamaterials combining ferromagnetic, dielectric and/or metallic structures for planar circuits applications", *Proc. of the Bianisotropics 2004 Conference*, Ghent, Belgium, September 2004.

[74] G. Tayeb, S. Enoch, P. Sabouroux, N. Guérin, P. Vincent, "Compact directive antennas using metamaterials," *Proc. of 2002 JINA conference,* Vol. 2, pp. 101-104, Nice, Nov. 2002.

[75] G. Lovat, P. Burghignoli, F. Capolino, D.R. Jackson,and D. R. Wilton, "Analysis of Directive Radiation From a Line Source in a Metamaterial

Slab With Low Permittivity," *IEEE Trans. Antennas Propag.*, Vol. AP-54, No. 3, March 2006

[76] B. Gralak, S. Enoch and G. Tayeb, "Anomalous refractive properties of photonic crystals," *J. Opt. Soc. Am. A,* vol.17, pp1012-1020, 2000.

[77] N. Guérin, C. Hafner and R. Vahldieck, "Compact directive antennas using metallic photonic crystals," *Proc. of the 2005 IEEE Symposium on Antennas and Propagation,* Washington DC, 4-8 July 2005.

[78] X. Dardenne and C. Craeye, "Numerical Study of low-profile directive antennas based on metamaterials," *Proc. of the 2004 Intl. Student Seminar,* St-Petersburg, June 2004.

[79] Y. J. Lee, J. Yeo, R. Mittra and W. S. Park, "Design of a High-Directivity Electromagnetic Band Gap (EBG) Resonator Antenna Using a Frequency-Selective Surface (FSS) Superstrate," *Microw. Opt. Tech. Lett.*, vol.43, no.6, pp.462-467, Dec. 2004.

[80] A.P. Feresidis, G. Goussetis, S. Wang and J.C. Vardaxoglou, "Artificial Magnetic Conductor Surfaces and Their Application to Low-Profile High-Gain Planar Antennas," *IEEE Trans. Antennas Propag., vol AP-53, pp.209-215, Jan. 2005.*

[81] A. Morini, T. Rozzi and G. Venanzoni, "On the Analysis of Slotted Waveguide Arrays," *IEEE Trans. Antennas Propag.*, Vol AP-54, pp.2016-2021, July 2006

[82] C. Craeye, "A Fast Impedance and Pattern Computation Scheme for Finite Antenna Arrays," *IEEE Trans. Antennas Propag.*,Vol. 54 No. 10, October 2006